Modeling Classical Dynamics and Quantum Effects in Superconducting Circuit Systems

by

Peter Groszkowski

A thesis
presented to the University of Waterloo
in fulfillment of the
thesis requirement for the degree of
Doctor of Philosophy
in
Physics

Waterloo, Ontario, Canada, 2015

Abstract

In recent years, superconducting circuits have come to the forefront of certain areas of physics. They have shown to be particularly useful in research related to quantum computing and information, as well as fundamental physics. This is largely because they provide a very flexible way to implement complicated quantum systems that can be relatively easily manipulated and measured. In this thesis we look at three different applications where superconducting circuits play a central role, and explore their classical and quantum dynamics and behavior.

The first part consists of studying the Casimir [20] and Casimir–Polder like [19] effects. These effects have been discovered in 1948 and show that under certain conditions, vacuum field fluctuations can mediate forces between neutral objects. In our work, we analyze analogous behavior in a superconducting system which consists of a stripline cavity with a DC–SQUID on one of its boundaries, as well as, in a Casimir–Polder case, a charge qubit coupled to the field of the cavity. Instead of a force, in the system considered here, we show that the Casimir and Casimir–Polder like effects are mediated through a circulating current around the loop of the boundary DC–SQUID. Using detailed analysis, we examine how the values of these currents change as we vary different physical circuit parameters. We show that for the set of physical parameters that can be easily obtained experimentally, the Casimir and Casimir–Polder currents can be of the order of 10^{-8} A and 10^{-13} A respectively.

In the second part, we theoretically model an experiment which was performed by Britton Plourde's group at Syracuse University, and which studied the transient dynamics of a nonlinear superconducting oscillator, based on a capacitively shunted DC–SQUID. Such DC–SQUID oscillators are used in many areas of physics and engineering, for example, as building blocks of amplifiers or qubits, qubit couplers, or as sensitive magnetic field detectors. In many of these situations, their steady state behavior is often considered, while in the experiment performed at Syracuse, of specific interest, was the response of a DC–SQUID oscillator to a short radiation that only briefly excited the system. In this thesis, we simulate this response at the experimental temperature, by numerically solving a set of classical stochastic differential equations that mimic the behavior of the circuit. This is done for different settings of the flux that is threaded through the DC–SQUID as well as different input pulse amplitudes. Furthermore, we briefly outline just how these kinds of brief excitations could be useful when applied in flux measurement protocols. We find that our simulations show good agreement with the experimentally obtained data.

The final part considered in this thesis, looks at the dynamics of a qubit coupled to a measuring probe, which is modeled as a harmonic oscillator. An example superconducting circuit, that could be used to implement such a setup, consists of a flux qubit inductively coupled to a DC–SQUID. This measurement scenario has already been explored in [111], but there, the authors only consider very short interaction times between the DC–SQUID and the qubit. Here, in contrast, we concentrate our efforts on studying the evolution of qubit as the measurement takes place, by solving the corresponding Lindblad master equation, but over longer measurement times. This is done by calculating the measurement induced dephasing rate of the qubit, as well as, discussing its sometimes present effective relaxation, in regimes where the measurement is considered to not be quantum non–demolition (QND). Finally, we briefly explore how well a potentially complicated evolution of the qubit can be approximated as a very simple Kraus map.

Acknowledgements

I would like to start by thanking my advisor Frank Wilhelm for his scientific and financial support, as well as his guidance throughout my PhD studies. Further thanks go to my examining committee: Ray Laflamme, Adrian Lupascu, Hamed Majedi as well as my external examiner Miles Blencowe for the time they have put into this endeavor and their helpful input.

I am grateful for the insight of my collaborators: Britton Plourde and Pradeep Bhupathi on the transient oscillator project, Eduardo Martin–Martinnez and Chris Wilson on the Casimir effect project, Jay Gambetta on the measurement dynamics project and Austin Fowler as well as Felix Motzoi on the flux qubit coupling project (not explicitly covered in this thesis).

I have been lucky to have met many great people while here. Special thanks to Felix, Farzad, Jonathan, Pierre-Luc, Emily, Seth, Luke, Razieh, Pol, Bruno, Daniel, Per and Markku. The last few, especially for their hospitality in Germany, and for making my stays there so enjoyable.

A very special thank you also goes to my great office mates over the years (in alphabetical order): Agnes, Jean-Luc, Moj and Yuval — our endless discussions about anything and everything have always been entertaining.

I consider myself very lucky to have been a part of the IQC. It has been a great place to think about physics, and I'm certain that it will only get better in the future. Many thanks to all those behind making it what it is today. I would also like to acknowledge the generous financial support that the IQC has provided me with.

Computing has played a central role in all of my research. I am very grateful to countless open source developers for providing quality software that made my life that much easier.

Last, but certainly not least, I would like to thank my parents for all their love and support, and Silvia for being the best partner–in–life one could ask for.

Contents

List of Figures

Chapter 1

Introduction

1.1 Motivation

The 20th century saw great changes in our understanding of the world around us, in particular from the point of view of physics. One key area that has had a tremendous impact, not just on our state of knowledge, but also on our everyday lives, has been the discovery of quantum mechanics. Within the last few decades we have started to learn not just how to observe the quantum behavior of nature, but how to control it as well. One subfield of physics where this ability to control quantum systems has become very useful is quantum computation. Quantum computers, if ever built on a large scale, could potentially revolutionize how many everyday things are currently done. They could factor numbers [113], search [55] databases and even simulate physical systems [39, 115], all much more efficiently than their classical counterparts. While many of these things are possible in theory, building a large scale quantum computer is however, a formidable challenge. There are many physical systems that are potential candidates for implementation of quantum computers and their key building blocks — qubits, ranging from nonlinear optics, through NMR, to various proposals with atoms, and even more exotic systems such as nitrogen–vacancy centers in diamonds. Another very promising system that has gained a lot of momentum over the last few years, consists of electrical circuits operated while in their superconducting state. These superconducting circuits' key strengths lie in the fact that they provide a lot of freedom to construct fairly arbitrary quantum systems. Furthermore, a lot of our knowledge and expertise obtained from building classical computers and integrated circuits, directly caries over, which makes them relatively easy to fabricate in a lab. Recent proposals have also shown that the flexibility of superconducting circuits can be very useful when studying fundamental physics [94, 128], or when modeling quantum behavior of certain mechanical systems [64] — another area of active research.

Our motivation in this thesis, is therefore, to simply push the envelope further when it comes to our understanding of the usefulness of superconducting circuits in areas related to both fundamental physics, as well as applications related to quantum computation. We do this through three different projects, which consist of: looking at Casimir and Casimir–Polder like effects in a superconducting circuit system, studying a transient response of a superconducting oscillator and finally by studying a measurement process of a superconducting qubit coupled to a meter.

1.2 Outline

This thesis is organized as follows. The second chapter briefly outlines a couple of basic concepts of superconductivity, and uses them to introduce the Josephson effect. It then looks at a few superconducting circuits that are used throughout the rest of the thesis, and describes means by which one can arrive at a Hamiltonian of any arbitrary circuit. The third chapter starts with a short historical overview of the Casimir and Casimi–Polder effects, after which, it presents a detailed mathematical analysis of analogous phenomena in a superconducting circuit system. The fourth chapter looks theoretical modeling of an experiment conducted at the Syracuse University by the group of Britton Plourde, that studied a transient response of a highly nonlinear, superconducting oscillator made out of a DC–SQUID. The fifth chapter explores the measurement dynamics of a qubit coupled to a harmonic oscillator, which similarly is modeled as a superconducting circuit consisting of a flux qubit inductively coupled to a DC–SQUID. Finally, the final, sixth chapter, presents conclusions and outlines possible future research directions.

Chapter 2

Superconducting Circuits

In this chapter, we briefly review some of the key concepts behind superconductivity and attempt to justify why it has been so useful in recent developments related to studies in quantum information and fundamental physics. We also provide a discussion of a few widely used superconducting circuits and outline their properties. We then list steps that have to be taken in order to mathematically describe such circuits, and in particular how to obtain their quantum Hamiltonians. Finally, we go through an explicit example of using these steps to write down a Hamiltonian of a simple circuit consisting of a charge qubit coupled to an LC–oscillator, which shares some of the properties of a more complicated system that is studied in Chapter 3.

2.1 Superconductivity — Basics

Superconductivity was first discovered in 1911 by a Dutch physicist named Heike Kamerlingh Onnes [99]. He noticed that when mercury is cooled below 4.2K, its resistivity to current disappears. The implications of this discovery play a very important role in many aspects of modern physics to this day. While high temperature superconductivity is not fully yet understood, physicists over the last century made tremendous progress in understanding it at low temperatures, and more importantly perhaps, even harnessing its effects to do useful things, ranging from building less noisy electric circuits, to building large superconducting magnets that are not just responsible for super fast trains [127] but also play a central role in our studies of the true nature of the universe [126]. In the next couple of paragraphs, we will briefly point out a few key concepts, however, for a detailed review of superconductivity we refer the reader to texts such as [28] and [117], or in a context of superconducting circuits, articles such as [101].

A central breakthrough in the efforts of understanding superconductivity came in 1957, when Bardeen, Cooper and Schrieffer [2], proposed a microscopic theory

(BCS theory), which argued that under some conditions, the scattering between the atomic lattice vibrations (phonons) and electrons, introduces an effective attractive force between the electrons, which can overcome their Coulomb repulsion. This leads to some of them teaming up and forming *Cooper pairs*. These Cooper pairs are no longer fermions and do not need to adhere to the Fermi's exclusion principle. Instead, they are bosons, and hence their behavior is governed by the Bose–Einstein statistics, which in turn means that they can condense into the same many–body state. We will shortly see that a phase of the wavefunction associated with such a sate, can be useful when describing the macroscopic behavior of electrical circuits made out of superconducting materials. A further consequence of the pairing of electrons, and an important piece of the puzzle of conventional superconductivity that came along with the BCS theory, is the presence of an energy band gap, often labeled as $\Delta_{\rm gap}$. It is typically defined as the energy between the ground state of a superconductor and the energy of the lowest quasiparticle excitation. The value of $\Delta_{\rm gap}$ is typically highest at low temperatures and vanishes as the temperature approaches the critical temperature of a given superconductor. The presence of $\Delta_{\rm gap}$ has a profound impact on how a superconductor interacts with an electromagnetic field — in particular since the energy has to be conserved[1], an incoming photon can only be absorbed by a superconductor if its energy is greater than $2\Delta_{\rm gap}$ — the factor of 2 comes the destruction of a Cooper pair in order to create a pair of quasiparticles. In aluminum for example, $\Delta_{\rm gap}$ is of the order of 75 GHz, which sets a limit on the frequency of radiation that we can use in superconducting circuit experiments before the dissipative effects need to be considered (assuming the temperature is low enough). We will come back to this very point in Chapter 3 when discussing an energy cutoff of electromagnetic field modes in a stripline cavity. In the next section, we will discuss an effect that is of great importance when using superconductors to design and implement electrical circuits.

2.1.1 The Josephson Effect

In this section we discuss a very important effect that will form the basis of many practical applications of superconducting circuits — the Josephson Effect. In 1962, Josephson made a theoretical prediction that a zero–voltage supercurrent should flow in a junction composed of two superconducting electrodes, separated by a thin insulating barrier [67]. He further postulated that such a current can be written as

$$I = I_0 \sin\varphi, \tag{2.1}$$

---

[1] The momentum needs to also be conserved of course. For a discussion on the implication of $\Delta_{\rm gap}$ on momentum conservation, see for example [28].

where I_0 is called the critical current of the junction, and φ the difference of the superconducting phases associated with the wavefunctions of the Cooper pairs in the superconductors on either side of the barrier. Moreover, he continued, a voltage across such a junction should be proportional to time derivative of the phase difference φ. Mathematically one can express this as

$$V = \frac{\Phi_0}{2\pi}\dot{\varphi}, \tag{2.2}$$

where $\Phi_0 = 2.07 \times 10^{-15}\,\mathrm{Wb}$ is referred to as the magnetic flux quantum. Equations 2.1 and 2.2 are often called the *Josephson relations*. This effect, in its simplest form, can be attributed to the Cooper pairs located on either side of the junction, being able to tunnel across the barrier. The key reason why Josephson junctions are so important is that as long as they are driven with currents smaller than their critical current and operated at cold enough temperatures (i.e., below the critical temperature of the material they are constructed from), they are both non–dissipative, and nonlinear! The fact that they are non–dissipative helps preserve their quantum effects, while the nonlinearity leads to an anharmonicity of the junction's energy structure, which in turn is critical to various qubit designs (as it allows for selective addressability of particular energy level transitions), as well as in other applications (for example in the design of various amplifiers [21, 58, 131]).

The most widely used material when it comes to fabricating Josephson junctions in applications related to quantum information and fundamental physics, is aluminum. The fabrication is typically done by a process called shadow evaporation which consists of depositing two layers of aluminum on a substrate made out of sapphire or silicon, with an oxidation step in between [33]. Figure 2.1(a) shows a picture of such aluminum Josephson junction as viewed from the top. The image shows two "fingers" which form the electrodes. The thin oxide layer (not directly visible) between these fingers provides the necessary barrier through which the Cooper pair can tunnel. By varying the area of overlap of the two layers of aluminum, as well as the thickness of the oxide layer, the effective capacitance of the junction as well as its critical current can be tuned to desired values[2].

2.1.2 RCSJ Model

In order to mathematically model Josephon junctions, it is useful to use the RCSJ model [117]. In it, a junction is described as a capacitor in parallel with a resistor, as well as an inductive element called the *Josephson element*. Figure 2.1(b) shows this schematically. The Josephson element is drawn as a rotated cross and it is assumed that the current through it satisfies Eqs. 2.1 and 2.2. As was already briefly stated

---

[2] Increasing the overlap increases the junction's capacitance, but decreases the its critical current [117].

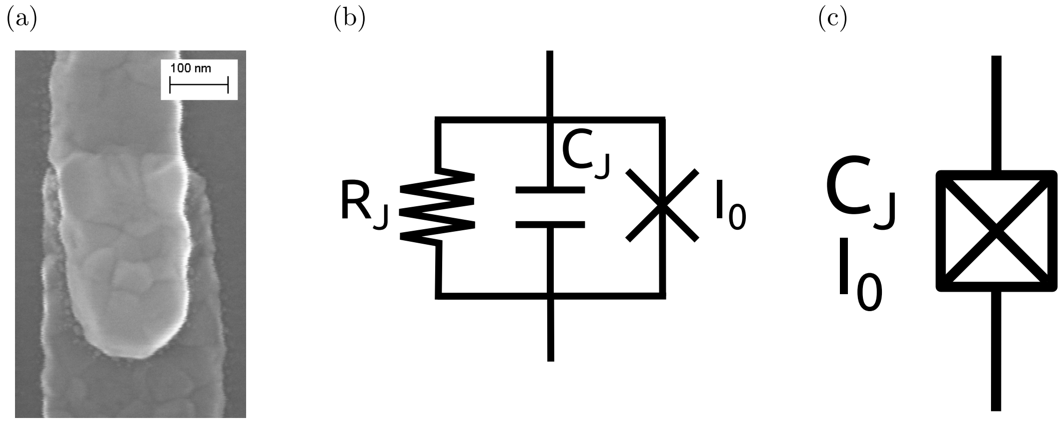

Figure 2.1: (a) A picture of a fabricated aluminum Josephson junction, as seen from the top. The sample was prepared, as well as imaged by Jean-Luc Orgiazzi and is being used with permission. (b) A Josephson junction described by the RCSJ model as a resistor in parallel with a capacitor and a Josephson element, which satisfies the Josephson relations shown in Eqs. 2.1 and 2.2. (c) A simpler representation of the schematic in (b) where the resistance is assumed large enough to be neglected.

above, in many applications the junctions are considered non–dissipative, and hence the resistance is often assumed to be large enough to be neglected. In those cases, as simpler schematic shown in Fig. 2.1(c) is often used.

2.2 Common Circuits

Within the last couple of decades, many different superconducting circuits have been studied for various purposes, ranging from applications to quantum information, through metrology, to even fundamental physics. In this section we review a few very important constructs that often come up in these different applications, and that we will come back to in other chapters of this thesis. In practice, most superconducting circuits consist of standard inductors, capacitors, resistors, as well as nonlinear Josephson junctions (which were discussed in Sec. 2.1). These elements are then arranged in various configurations to produce certain desired behavior. We should stress that the noisy behavior which often is attributed to the coupling of a superconducting circuit to the outside world, can be modeled using resistors or transmission lines, which in turn are often described using large (infinite) arrangements of lossless capacitive and inductive elements, that effectively couple a given system to a large (infinite) number of degrees freedom.

In Fig. 2.2 we present four different examples of very commonly used circuits. Figure 2.2(a) shows a schematic of a DC Superconducting QUantum Interference

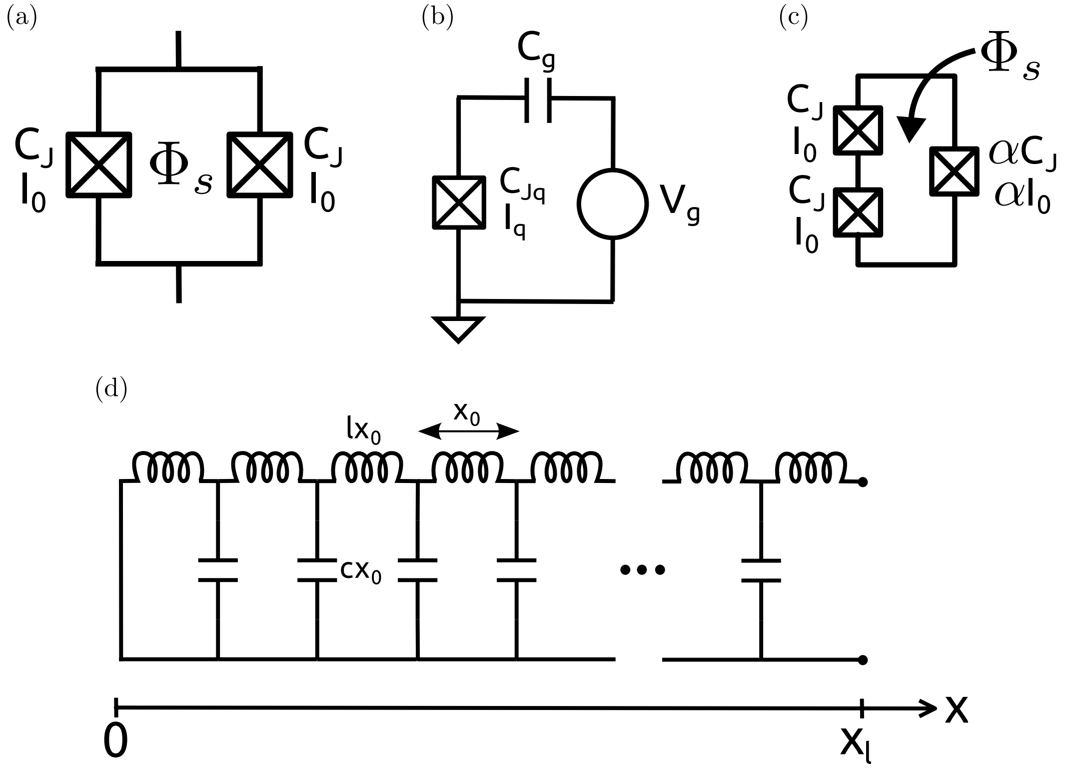

Figure 2.2: (a) A DC–SQUID consisting of two parallel Josephson junctions, threaded by a magnetic flux Φ_s. In this diagram we neglect the geometric inductance of the DC–SQUID loop, which is often done when the Josephson inductance associated with the junctions is much bigger. (b) A charge qubit controlled by a biasing voltage V_g. The computational basis of such a qubit are often defined in terms of the number of extra Cooper pairs that occupy the "qubit island" — the node between the Josephson junction and the capacitor C_g. (c) A flux qubit consisting of a loop interrupted by three Josephson junctions and biased with a magnetic flux Φ_s. One of the Junctions is typically smaller than the other two, which leads to a potential energy landscape that lets us define computational basis in terms of currents circulating in opposite directions around the loop. (d) A schematic of a stripline cavity composed of an arrangement of capacitors cx_0 and inductors lx_0, with c (l) representing the capacitance (inductance) per unit length, and x_0 the length of a unit cell. The structure of the field inside such as system depends on the boundary conditions that are chosen — in the drawing above the cavity is considered "closed" at $x = 0$ and "open" at $x = x_l$.

Device (DC–SQUID). It consists of two parallel Josephson junctions forming a loop. In this particular case, each junction is assumed to have a capacitance C_J and the critical current I_0. An external flux Φ_s is threaded through the loop. In the regime where the loop is small (i.e., when its geometric inductance L_g is much smaller than the inductance associated with each Josephson junction L_{J0}, namely when $L_g \ll L_{J0} = \Phi_0/2\pi I_0$), a DC–SQUID can be approximately treated as a single junction with a flux–controlled critical current. This fact has been explored in various applications ranging from metrology to quantum computing. A DC–SQUID will play a lead role throughout the rest of this thesis, and will be discussed in more detail in Chapters 3 and 4 as well as Appendix D.

Figure 2.2(b) shows a circuit of a charge qubit [10, 91]. It consists of a single Josephson junction with capacitance C_{Jq} and critical current I_q, in series with a capacitor labeled C_g and a voltage source V_g. When V_g is biased appropriately, the qubit states can be associated with the excess number of Cooper pairs that occupy the charge qubit "island" — the electrode between the Junction capacitor C_{Jq} and C_g. Such a qubit can be controlled by tuning the biasing voltage V_g. A more complicated variations of this design can include a shunt capacitor in parallel with the junction, which limits the sensitivity of the qubit to the charge noise at a cost of anharmonicity, and even a DC–SQUID that replaces the single junction, which in turn allows for another means of controlling the qubit [72].

Next, in Fig. 2.2(c) we present a schematic of a flux qubit [100]. It consists of a loop with three junctions, with one of the junctions slightly smaller than the other two. In the diagram this is represented by the factor α, which scales the capacitance and the critical current of the junction on the right arm of the loop. In typical cases $\alpha \approx 0.7$. In a flux qubit, the computational basis states correspond to the currents circulating in the opposite direction around the loop. Such a qubit can be both controlled, as well as coupled through the applied flux Φ_s that threads the circuit loop. As in the case of the charge qubit, there are variations to this general design. The first incarnation of a flux qubit, for example, considered a loop with only a single junction [44], however, that design required the physical size of the qubit to be large, which in turn lead to more sensitivity to flux noise.

Finally, in Fig. 2.2(d) we show a schematic of a stripline cavity. It consists of an arrangement of capacitors cx_0 and inductors lx_0, where c (l) represents the capacitance (inductance) per unit length, and x_0 is the length of a unit cell. To model the continuous nature of a stipline caivty, one takes the limit of $x_0 \to 0$, as will be shown in Chapter 3. The structure of the field inside such as system depends on the boundary conditions that are chosen — in the drawing above, the cavity is considered "closed" at $x = 0$ and "open" at $x = x_l$. When these devices are coupled to qubits, they are mathematically similar to quantum electrodynamic systems consisting of atoms inside cavities, except with often much more tunable parameters, and many orders of magnitude larger coupling between the fields and the atoms/qubits [7]. Besides opening doors for studies in fundamental physics, using stripline cavities have been shown to be very useful in applications to quantum information. They provide a means to both couple as well as read out qubits much more effectively than ever before [3, 23].

The key observation that could be made from our brief overview above, is that superconducting circuits provide a lot of freedom when it comes to studying interesting quantum behavior, mainly because they contain a lot of intrinsic flexibility. After all, we have many different configurations in which circuits can be constructed, generally leading to very different behavior. Moreover, the extensive amount of experimental expertise that scientists and engineers have gained through fabricating integrated circuits and understanding the technology required for classical solid state computing, can be often directly applied here.

2.3 Circuits and their Hamiltonians

Now that we have shown a few important circuits, we need to address the question of how we can model their quantum behavior mathematically. In classical physics, and electrical engineering applications in particular, in order to understand the behavior of a given circuit, it is often enough to simply write down the corresponding equations of motion (which can be done by following Kirchhoff's rules) and solve them for currents and voltages that we are interested in. When treating these circuits as quantum objects however, it is useful to first find their effective Hamiltonians, which can then be used in standard ways to solve the corresponding Schrödinger equation. The procedures that describe how to do this, have been discussed in various publications [16, 32, 132]. Here, for completeness, we provide a brief summary of the main steps. It is assumed that the reader is familiar with elementary circuit theory as presented in for example [34].

In the limit where the circuit can be divided into lumped elements, namely when the wavelengths of the radiation in the circuit are longer than the dimensions of the elements themselves, we can split the circuit into nodes that are connected by two–terminal components, often called branches. Each branch has an associated voltage across it, and a current through it. Knowing these voltages and currents, lets us completely describe the behavior of a given circuit. A useful convention that has been especially helpful when describing superconducting circuits (with Josephson junctions in particular) is to use fluxes and charges instead of voltages and currents as the degrees of freedom. This is because one can show that the flux across a branch is proportional to the superconducting phase difference that we have already investigated in Sec. 2.1. The general relationship that connects the two descriptions can be written as

$$\Phi_{\text{branch}}(t) = \int_{-\infty}^{t} V_{\text{branch}}(t')dt' \tag{2.3}$$

$$Q_{\text{branch}}(t) = \int_{-\infty}^{t} I_{\text{branch}}(t')dt', \tag{2.4}$$

where Φ_{branch} and V_{branch} correspond the flux and voltage across a branch respectively, while Q_{branch} and I_{branch} the charge and current. We are now ready to outline the steps that can be taken to arrive at a quantum Hamiltonian description of a given circuit. It is worth stressing that there are slight variations in different references that discuss this topic — for example, often explicitly writing down the equations of motion can be skipped and the Lagrangian can be obtained directly. For the most complete description that covers many details and nuances that one can come across, we point the reader to [16].

For simplicity, let us assume that we are dealing with a circuit that consists of no resistors[3], but only capacitors, inductors and Josephson elements. Furthermore following [32], we stress that all the voltage (current) sources in the circuit can also be modeled in terms of capacitors (inductors) with large initial charges (fluxes)[4].

The first step in finding the Hamiltonian, consists of simply labeling the circuit in a consistent way. To do this, we first arbitrarily chose one reference node, and without loss of generality, associate with it zero flux. We then, starting at this node, define a spanning tree of the circuit network, which consists of a loop–free graph that includes all of its nodes[5]. Branches that belong to the spanning tree are called *tree branches*, while branches outside of it, *chords* [16] or *closure branches* [32]. Each of the closure branches defines a loop by joining its two end points by the minimal path on the spanning tree. If a given branch is part of the spanning tree, then its branch flux can be expressed as simply the difference between the fluxes of the end nodes. Alternatively in a case of a closure branch, the total branch flux also includes the applied flux through the loop which the closure branch defines. Mathematically we can write this as

$$\Phi_{\text{branch}} = \Phi_n - \Phi_{n'} \qquad \text{if branch} \in \text{spanning tree} \tag{2.5}$$

$$\Phi_{\text{branch}} = \Phi_n - \Phi_{n'} + \Phi_{\text{ext}} \qquad \text{if branch} \notin \text{spanning tree}, \tag{2.6}$$

---

[3] If dissipative elements such as resistors are present, they can be modeled as transmissions lines (i.e., infinite sets of dissipation free capacitors and inductors), or in a related way, by using the Caldeira–Leggett model, which treats each dissipative element as a bath of harmonic oscillators that couple to the degrees of freedom of the circuit. We point the reader to [16], [132] and references therein for more information on this topic.

[4] In practice this is often not necessary. One can directly substitute currents due to branches with current sources into Eq. 2.7, and similarly relate node fluxes at the end points of branches that contain voltage sources to voltages, through Eq. 2.3.

[5] Such a spanning tree is not unique.

where n and n' are the indices of the end nodes of the branch, and Φ_{ext} the external flux. Next, using Kirchhoff's rules, and the means of converting between branch and node fluxes we have just outlined, we write the current conservation relation for each of the nodes, except the reference node. This leads to a set of equations that read

$$\sum_{\substack{i \in \text{connecting} \\ \text{branches}}} I_i = 0. \tag{2.7}$$

The sum is over the branches that connect to the node in question. The directions of the currents can be defined in a arbitrary way, but need to be consistent for all the nodes. Once we have the equation of motion for each node n, we treat it as a Euler–Lagrange equation

$$\frac{\partial L}{\partial(\partial_t \Phi_n)} - \frac{\partial L}{\partial \Phi_n} = 0, \tag{2.8}$$

for a Lagrangian L, which can be obtained by integration. The next step is to apply the Legendre transformation and obtain the classical Hamiltonian. Mathematically we have

$$H = \sum_n Q_n \dot{\Phi}_n - L, \tag{2.9}$$

where each Q_n satisfies

$$Q_n = \frac{\partial L}{\partial \dot{\Phi}_n}. \tag{2.10}$$

H is now a classical Hamiltonian that describes the electrical circuit. The final step is to promote the classical degrees of freedom Φ_n and Q_n into quantum operators. This is done by introducing standard commutation relationships between them, which results in

$$[\Phi_n, Q_k] = i\hbar\delta_{n,k}. \tag{2.11}$$

This procedure leads to a quantum description of the circuit, which we set out to find. In practical applications, one can often go a step further, and rewrite the newly obtained Hamiltonian in more easily usable forms: for example, in terms of lowering and raising operators, or in the case where the circuit is operated as qubit, in terms of Pauli operators (by first truncating the Hilbert space to two levels).

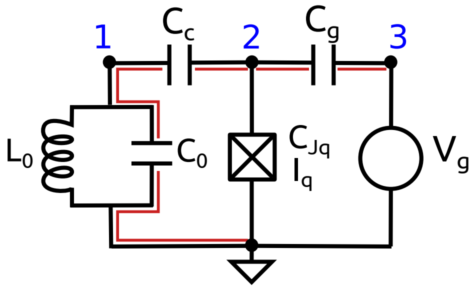

Figure 2.3: A circuit diagram of a charge qubit coupled to an LC oscillator and a voltage source. I_q is the critical current of the Josephson junction, C_{Jq} the capacitance across the junction, and C_c and C_g, the capacitances that couple the qubit island to the oscillator and voltage source V_g respectively. The blue numbers represent node labels, while the red line, the circuit spanning tree (see Sec. 2.3 for details).

2.3.1 Example: Charge Qubit Coupled to an LC Oscillator

Let us apply the discussion from the previous section, to look at another example circuit, this time in a bit more detail. Here we derive a Hamiltonian of a circuit which has some of the features of a more complicated scenario that we will consider in Chapter 2. In Fig. 2.3 we show a circuit of a charge qubit coupled to an LC oscillator and biased by a classical voltage source V_g. L_0 and C_0 represent the inductance and capacitance of the LC circuit, while C_c and C_g couple the oscillator and the voltage source to the qubit island respectively. Finally, C_{Jq} and I_q are the capacitance and critical current of the Josephson junction that makes up the qubit. The red line shows an example spanning tree, although in this case, since no external fluxes are considered, defining such a spanning tree explicitly is not necessary.

We will treat the fluxes at nodes 1 and 2 as active degrees of freedom, while the flux at node 3 will be treated as a classical parameter, and later related to the voltage V_g. Using Eqs. 2.1, 2.2, 2.5, 2.6 and standard descriptions for currents across capacitors and resistors, we can utilize Kirchhoff's current rule from Eq. 2.7 to write down the equations of motion for our circuit as

$$C_0\ddot{\Phi}_1 + \frac{1}{L_0}\Phi_1 - C_c\left(\ddot{\Phi}_2 - \ddot{\Phi}_1\right) = 0, \tag{2.12}$$

and

$$C_c\left(\ddot{\Phi}_2 - \ddot{\Phi}_1\right) + C_{Jq}\ddot{\Phi}_2 + I_q \sin\left(\frac{\Phi_2}{\phi_0}\right) - C_g\left(\ddot{\Phi}_3 - \ddot{\Phi}_2\right) = 0, \tag{2.13}$$

where we have taken $\phi_0 = \Phi_0/2\pi$. Integrating these to get a Lagrangian, gives

$$\begin{aligned} L =& \frac{C_{Jq}}{2}\dot{\Phi}_2^2 + \frac{C_0}{2}\dot{\Phi}_1^2 + \frac{C_c}{2}\left(\dot{\Phi}_2 - \dot{\Phi}_1\right)^2 + \frac{C_g}{2}\left(V_g - \dot{\Phi}_2\right)^2 \\ &+ \phi_0 I_q \cos\left(\frac{\Phi_2}{\phi_0}\right) - \frac{1}{2L_0}\Phi_1^2. \end{aligned} \tag{2.14}$$

In the last step we have replaced $\dot{\Phi}_3$ with V_g. The next step, is to calculate the conjugate variables of Φ_1 and Φ_2. These will correspond to effective charges at nodes 1 and 2 respectively. Hence we have

$$Q_1 = \frac{\partial}{\partial\dot{\Phi}_1}L \tag{2.15}$$

$$= C_{\text{osc}}\dot{\Phi}_1 - C_c\dot{\Phi}_2, \tag{2.16}$$

and for the case of Φ_2,

$$Q_2 = C_r\dot{\Phi}_2 - C_c\dot{\Phi}_1 - C_g V_g. \tag{2.17}$$

In the last two expressions, we have defined $C_{\text{osc}} = C_0 + C_c$, and temporarily $C_r = C_{Jq} + C_J + C_g$. The next step is inverting these and solving for $\dot{\Phi}_1$ and $\dot{\Phi}_2$, which leads to

$$\dot{\Phi}_1 = \frac{C_r}{C_t}Q_1 + \frac{C_c}{C_t}Q_2 + \frac{C_g C_c}{C_t}V_g \tag{2.18}$$

$$\dot{\Phi}_2 = \frac{C_c}{C_t}Q_1 + \frac{C_{\text{osc}}}{C_t}Q_2 + \frac{C_g C_{\text{osc}}}{C_t}V_g, \tag{2.19}$$

where we have introduced $C_t = C_r C_c + C_0(C_{Jq} + C_g)$. Finally we are ready to write the Hamiltonian of our simple circuit, which reads

$$\begin{aligned} H =& \dot{\Phi}_1 Q_1 + \dot{\Phi}_2 Q_2 - L \\ =& \frac{\left(C_g V_g + \frac{C_c}{C_{\text{osc}}}Q_1 + Q_2\right)^2}{C_\sum} - I_q\phi_0\cos\left(\frac{\Phi_2}{\phi_0}\right) \\ &+ \frac{1}{2C_{\text{osc}}}Q_1^2 + \frac{1}{2L_0}\Phi_1^2 - \frac{C_g}{2}V_g^2. \end{aligned} \tag{2.20}$$

Here for convenience we introduced yet another effective capacitance $C_\sum = \frac{C_c^2}{C_{\text{osc}}} + C_c + C_{Jq} + C_g$. Furthermore, anticipating the expression we want to obtain, we completed the square in Q_2. The terms containing charges Q_i (fluxes Φ_i) can be interpreted as analogous to kinetic (potential) energies in a mechanical system.

The last step is to quantize our circuit. This is simply done by promoting the variables which represent the degrees for freedom of the circuit into operators, and enforcing their commutation relations. In our case, it leads to

$$[\Phi_n, Q_m] = i\hbar\delta_{n,m}. \tag{2.21}$$

with n and m being 1 or 2. Hence we now have a quantum version of the Hamiltonian of the circuit shown in Fig. 2.3. In order to treat our system as a qubit coupled to an oscillator, we would need to go a step further and truncate the Hilbert space of the operators Φ_2 and Q_2 to only two levels. This is something we will look at in more detail in Chapter 3, in the context of the system presented there.

It is useful however, to make some observations about Eq. 2.20. The last term on the third line corresponds to a voltage offset that comes from the biasing voltage V_g, and when studying the dynamics of the circuit, can be neglected. The first two terms on the third line represent a Hamiltonian of a simple harmonic oscillator with a natural frequency of $\omega_{\text{osc}} = 1/\sqrt{C_{\text{osc}} L_0}$ — the fact that the LC oscillator couples to the qubit via the C_c capacitor, results in its frequency being shifted, since $C_{\text{osc}} = C_0 + C_c$. Finally, the second line of 2.20 shows the effective Hamiltonian of the qubit. Its kinetic energy (the first term) is affected by both the biasing voltage V_g as well as by the presence of the LC oscillator, through Q_1. These two contributions can add or subtract to the net charge on the qubit island (node 2) and when the parameters are chosen appropriately, can provide a means for qubit control. Finally, we note that expanding the first term of the second line of Eq. 2.20 will, among other expressions, contain $\frac{C_c^2}{C_{\sum} C_{\text{osc}}^2} Q_1^2$. This term represents a contribution that is often described as an analogous of the A^2 term in the Hamiltonian of a charged particle in an electromagnetic field. We will discuss the general importance and implications of this fact in more detail in Chapter 3.

2.4 Summary and Conclusions

In this chapter we have reviewed some of the key concepts of superconductivity, discussed the Josephson effect, as well as shown a few widely used superconducting circuits, while outlining their key properties. We then looked at how to obtain Hamiltonians of such circuits, and ended with a Hamiltonian derivation of a specific circuit consisting of a charge qubit coupled to an LC–oscillator, which can be thought of, as a simpler version of a circuit studied in more detail in Chapter 3.

Chapter 3

Casimir–like Effects in a Superconducting Circuit System

In this chapter, we look at Casimir and Casimir–Polder–like effects in a superconducting circuit system. We start with a brief review that introduces these topics in a historical context. We then define a superconducting circuit that we use to model a cavity as well an interacting qubit. Next, we derive the corresponding Hamiltonians and calculate the energy shift due to the presence of the coupling qubit, which in turn lets us define a Casimir–Polder–like effect in a form of a Casimir–Polder current. We then study the consequences that varying different physical circuit parameters has on our newly derived results. Finally, we finish the discussion by describing an analogous of a Casimir effect where we neglect the qubit and only concentrate on the superconducting stipline cavity with a flux–dependent boundary.

3.1 The Casimir Effect — Historical Overview

Our brief historical overview of the Casimir and Casimir–Polder effects mainly follows review papers [38, 85, 107] as well as [19, 20, 65].

Over the last century scientists have been trying to come to terms with the often highly unusual predictions of quantum theory. One of its particularly fascinating consequences, which was first discovered in the early 1900s by Max Planck while studying black–body radiation, is the zero–point energy and more importantly perhaps, the fluctuations associated with it. Planck looked at the average energy of an electromagnetic field mode of frequency ω, at temperature T. He arrived at an expression

$$U = \frac{\hbar\omega}{e^{\frac{\hbar\omega}{k_B T}} - 1} + \frac{1}{2}\hbar\omega. \tag{3.1}$$

He right away noticed the troubling fact, that in the limit of $T \to 0$ this expression reduces to $\frac{1}{2}\hbar\omega$. This was at odds with the conventional understanding at the time, where it was believed that at zero temperature all motion ceased, and therefore the average energy radiated should necessarily simplify to zero. This lead him to initially assume that this result must have no physical significance. A few years later, in 1913, Einstein along with Stern argued [37] that in the opposite limit of high temperature, where $k_B T \gg \hbar\omega$, the "extra" term is needed in order to recover the classically known result [85]

$$U = k_B T. \tag{3.2}$$

This, among other reasons [85], lead to them to write "The existence of zero–point energy is probable". The paper started a heated discussion of just how physically relevant this unusual term can be. The first possibly observable consequence of the zero–point energy (or more specifically fluctuations associated with it) was suggested by Debye [29] when he proposed that the zero–point energy fluctuations in atomic motion should lead to a reduction in X–ray scattering from crystals. Mulliken was able to experimentally confirm this prediction a decade later [90].

In 1916, Nernst further suggested that the zero–point energy fluctuations should also exist for free electromagnetic fields [95], hence discovering what is now often called the *quantum vacuum*. The analysis of the physical significance of this prediction and its various implications, in particular on cosmology, continued on. An important contribution came in 1948 in a proposal by Hendrik Casimir [20], even though he originally did not frame his discussion explicitly in terms of the zero–point fluctuations. He considered an idealized case of two parallel, conducting plates, with perfect reflectivity (effectively mirrors) and at zero temperature. He envisioned these plates to be separated by a distance d, as is shown in the schematic of Fig. 3.1(a). His key realization was that even with no photons present, the two mirrors will experience an attractive force. This was of particular importance because such a force could, in principle at least, be measured. By considering the structure of the field modes both between the mirrors and on the outside, he calculated this force as (here shown as pressure — force per area)

$$P_{\mathrm{Casimir}}(d) = -\frac{\pi\hbar c}{240}\frac{1}{d^4}. \tag{3.3}$$

Since Casimir's original proposal, many variations have been discussed, with some of initial constraints lifted. Experimental realizations have also been considered. Initially, due to the technical complications associated with properly aligning two plates in parallel, it was easier to consider a plate near lenses or spheres, but finally in 2002 an experiment with the originally proposed setup was successfully conducted [13]. It resulted in a confirmation of Casimir's prediction from Eq. 3.3 to within %15.

Another paper of Casimir that turned out to be very important in the study of the zero–point energy fluctuations, was also written in 1948 with Polder [107]. There, the authors considered a single conducting plate, interacting with an atom. Through similar arguments they were able to predict an attractive force between the atom and the plate — this kind of a force, where neutral atoms are coupled to neutral macroscopic objects through electromagnetic field fluctuations, is often now referred to as the Casimir–Polder force. Other variations of such a force have been explored over the years. One of particular interest to us is an atom within a cavity, interacting with the cavity boundaries. A schematic of such a setup is shown in Fig. 3.1(b), with the theoretical aspects studied in [1].

Although there have been multiple successful experiments that explored variations of both the Casimir–Polder as well as Casimir forces, they have shown to be difficult. In the rest of this chapter we will describe a mathematically similar systems to both a standalone cavity as well as a cavity with an atom, but implemented using a superconducting circuit. The key difference will be that instead of Casimir forces, we will consider analogous electrical currents. It is possible that with all the resent advances in superconducting circuit technology, in the future, experiments with such systems will be substantially easier and will let us explore the Casimir physics in more detail, and less effort.

Finally, let us briefly discuss another effect that builds on Casimir's original ideas — the Dynamical Casimir effect. The original proposal dates to 1970 [86] where Moore noticed that if the mirrors of a cavity discussed earlier moved, the mismatch between the structure of the vacuum modes at different points in time could lead to generation of real photons. In 1976 this idea was also expanded to a system with only a single mirror in free space [45]. Figs. 3.1(c) and 3.1(d) present a pictorial representations of these two scenarios. In the case of a single mirror, it was shown that radiation can also be generated, as long as the acceleration of the mirror is nonuniform. The Dynamical Casimir effect has been very elusive experimentally however, because in order for the physical mirrors to generate photons at a rate that modern equipment could detect, the mirrors would have to move at speeds close to the speed of light — a feat hard to implement with current technology. Nonetheless, in 2011, a team at Chalmers University of Technology in Sweden observed results consistent with a Dynamical Casimir effect, but in a system implemented using superconducting circuits [128].

3.2 The $\mathbf{A^2}$ Term in Field–Atom Interaction

Before we move onto our particular superconducting circuit that we will analyze, let us briefly discuss the relevance of the so called $\mathbf{A^2}$ term, and its importance to the study of the field–atom interactions. Let us consider a two level atom coupled to a single mode of the electromagnetic field. We can write down a general Hamiltonian

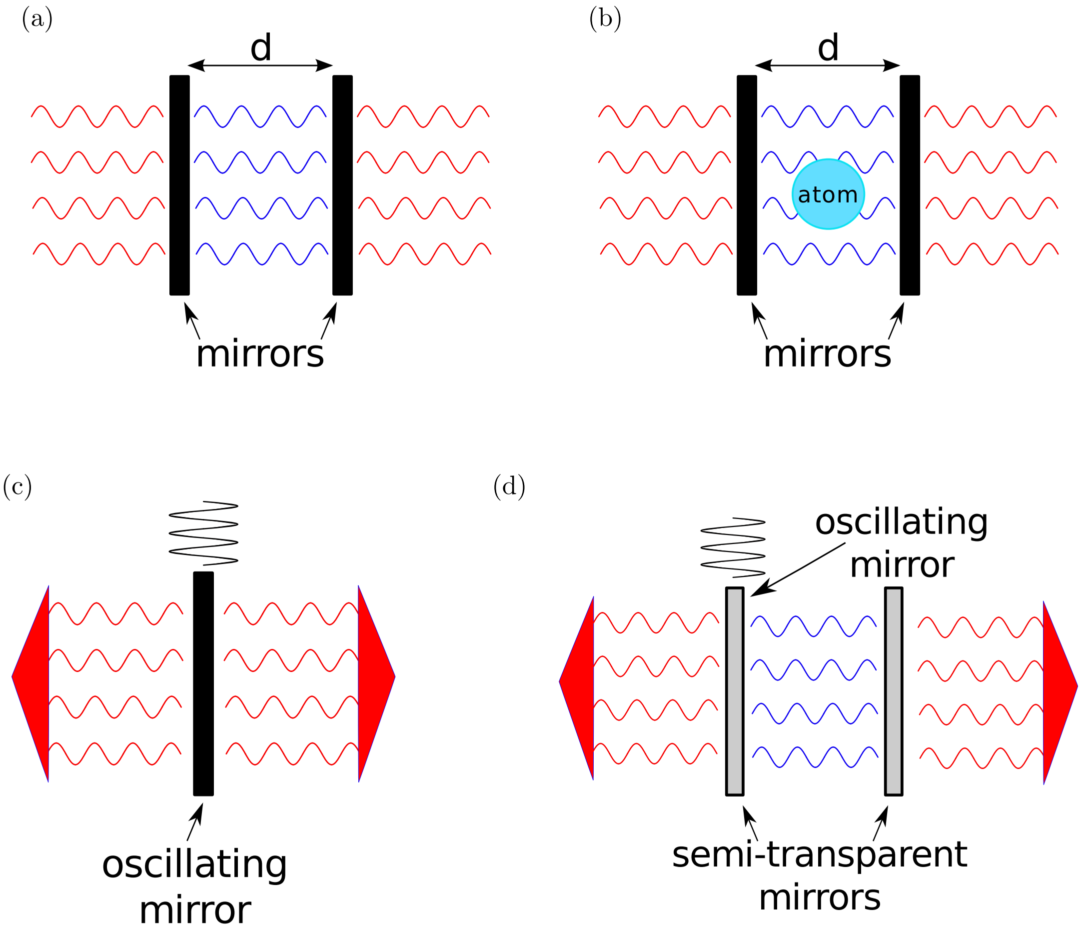

Figure 3.1: (a) Two parallel, stationary mirrors that Casimir envisioned in his original proposal from 1948. The structure of the field modes between the mirrors is different from what it is outside, which in turn leads to an attractive force between the mirrors. (b) Including an atom between the mirrors, can lead to either attractive or repulsive forces, depending on the type of coupling between the field and the atom as well as the boundary conditions of the field. (c) An example of a system where a dynamical Casimir effect can be observed. Here, one only considers a single mirror in free space, that is driven by a continuous signal. (d) A more elaborate example of a dynamical Casimir effect, with a cavity consisting of two mirrors, one stationary, and the other rapidly modulated. It is worth stressing that the diagrams are not to scale — in these systems when physical mirrors are considered (particularly in cases (a) and (b)), it is assumed that the length of the mirrors is substantially larger than the separation between them.

for such a system as

$$H_{\mathrm{atom-field}} = \frac{1}{2m}\left(\mathbf{p} - \frac{e}{c}\mathbf{A}\right)^2, \tag{3.4}$$

where m is the atom's mass, c the speed of light, e its charge, and $\mathbf{p}$ and $\mathbf{A}$ are the atom's momentum and field's vector potential respectively. In the Coulomb gauge, the interaction contribution simply reduces to

$$H_{\mathrm{atom-field-int}} = -\frac{e}{mc}\mathbf{A}\cdot\mathbf{p} + \frac{e^2}{2mc^2}\mathbf{A^2}, \tag{3.5}$$

with the first term, linear in $\mathbf{A}$, often called *paramagnetic* and the second, $\mathbf{A}^2$–dependent, *diamagnetic* (often also called the *field self–interaction* term). A mathematically analogous discussion can be made about superconducting qubits that are coupled to a field inside a superconducting waveguide [92, 93], as will be shown in some detail, in Sec.3.5. In those systems, since the term corresponding to the diamagnetic term above does not contain any operators acting on the qubit's Hilbert's space, its contribution is often neglected — in particular when discussing the dynamics of the qubit. It has been shown, however, that in atomic systems, where the Casimir–Polder effects are studied, under certain conditions, the diamagnetic term can be of importance. In [1] for example, where a setup with a two–level atom inside a cavity was explored in the context of the Casimir–Polder effect discussed in the last section, it was theoretically shown that if the atom's size is carefully considered, and it is small enough[1], the contribution of the diamagnetic term to the interaction energy can be of the same order as the contribution of the paramagnetic term, and hence should not be neglected.

3.3 Superconducting Circuit Implementation

The system we choose to study is a superconducting circuit, which consists of a coplanar waveguide (often referred to as a cavity) of length x_l with a DC–SQUID at one of its boundaries and a coupling qubit at some position x_q. We concentrate our discussion on the case of a charge qubit, but other qubit types, such as a flux qubit could provide an interesting research direction in the future. A circuit diagram that shows our system in some detail, is presented in Fig. 3.2. The DC–SQUID is located at $x = 0$, the qubit centered around $x = x_q$, and we take the boundary at $x = x_l$ to be open. We assume that the DC–SQUID is operated in its linear regime, and that its geometric inductance L_g is much smaller than the Josephson inductance of each of the junctions L_{J0} — namely we will consider the limit of

---

[1] The smaller the atom, the larger are the quantum field fluctuations that the atom coupels to.

$L_g/L_{J0} \to 0$. These assumptions and their consequences are studied in great detail in Chapter 4 as well as in Appendix D, with the key result being that in this limit, the DC–SQUID can be treated as a simple LC circuit, with its effective inductance (and hence the natural frequency) that depends on the flux threaded through the DC–SQUID — labeled Φ_s. We can model this cavity in a standard way [105], as a collection of infinitesimally small cells, each consisting of a capacitor cx_0 and inductor lx_0, with c and l representing the capacitance and inductance per unit length of material used, and the x_0, the length of each cell (we later take the limit $x_0 \to 0$) [7, 105].

We can write a general Hamiltonian of our full system as

$$H = H_{\rm sq} + H_{\rm cav} + H_{\rm sq-cav} + H_q + H_{\rm q-cav}, \tag{3.6}$$

where we have taken $H_{\rm sq}$ as the Hamiltonian of the DC–SQUID, $H_{\rm cav}$ of the cavity, $H_{\rm sq-cav}$, the interaction Hamiltonian between the DC–SQUID and the cavity, H_q, the qubit's Hamiltonian, and finally $H_{\rm q-cav}$, the interaction Hamiltonian between the qubit and cavity. In the Casimir–Polder effect treatment below, we will look at each of those in more detail, but our ultimate goal will be to diagonalize $H - H_{\rm q-cav}$, and treat $H_{\rm q-cav}$ as a perturbation dependent on the flux through the DC–SQUID, and controllable through rotations of the qubit. In the Casimir effect treatment shown in Sec. 3.10, it will be enough to only consider the Hamiltonians of the stripline cavity, the DC–SQUID and their interaction.

3.4 Normal Modes and the Cavity Hamiltonian

We begin by initially neglecting the qubit, and concentrating on the DC–SQUID and the cavity. As already mentioned, we will operate in the regime where the DC–SQUID is modeled as a linear LC oscillator. Following the discussions in Chapter 2 and Appendix D one can show that such an LC oscillator will have the effective capacitance of $C_{Js} = 2C_J$ and flux dependent inductance $L_{Js}(\Phi_s) = \phi_0(2I_0\cos(\Phi_s/2\phi_0))^{-1}$, where C_J and I_0 represent the capacitance and critical current of the individual Josephson junctions that make up the DC–SQUID respectively (as can be observed from Fig. 3.2(a)). Mathematically then, the physical circuit consisting of such an LC oscillator on a boundary of a stripline cavity is similar to a harmonic oscillator at an end of a string [130].

In order to write down the Lagrangian and later the Hamiltonian of our system, we turn to the circuit quantization rules discussed in Chapter 2. Namely, we divide the circuit into nodes and branches. To each node n we assign a node flux Φ_n that is related to the voltage by the relation $V_n = \partial_t \Phi_n$. Hence, assuming that the full cavity contains a total of N flux nodes, we can write down the current conservation

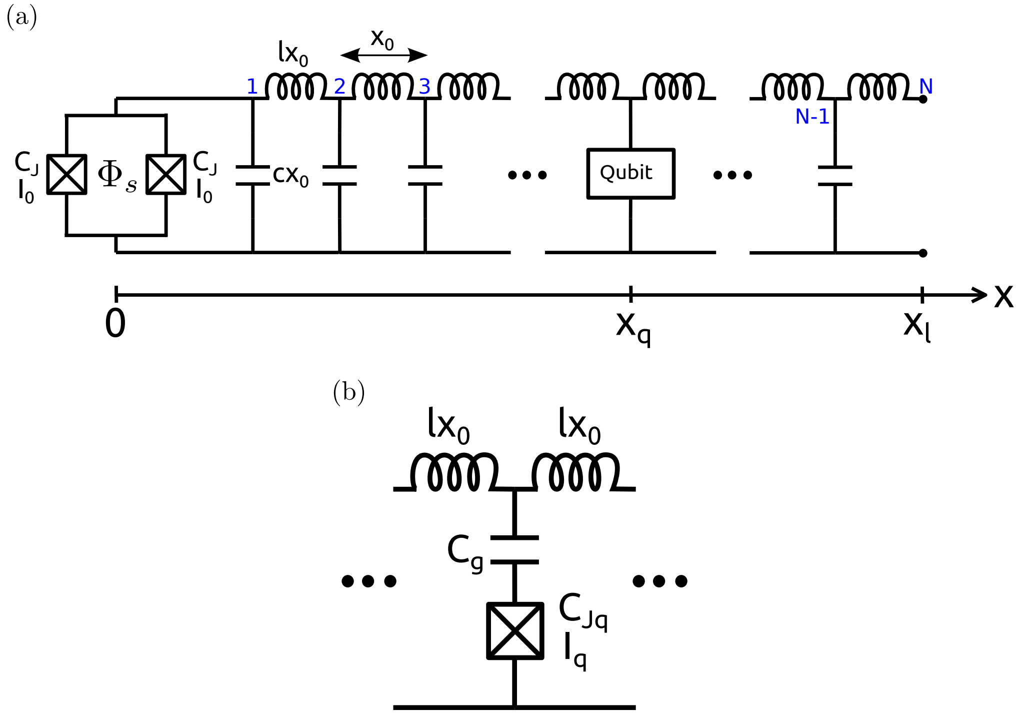

Figure 3.2: Diagram in (a) shows a schematic of a superconducting circuit that depicts a coplanar waveguide of length x_l, terminated at $x = 0$ by a DC–SQUID and open at $x = x_l$. The parameters c and l represent the capacitance and inductance per unit length respectively, while C_J and I_0 the capacitance and the critical current of the Josephson junctions that make up the DC–SQUID, which is threaded with a flux Φ_s. This cavity is coupled to a qubit which is centered around $x = x_q$. (b) An example of a superconducting qubit that could be used — a charge qubit.

equations in terms of node fluxes Φ_n. For each node $1 < n < N$ this leads to

$$\frac{1}{lx_0}\left(\Phi_{n-1} - \Phi_n\right) = \frac{1}{lx_0}\left(\Phi_n - \Phi_{n+1}\right) + cx_0\partial_t^2\Phi_n. \tag{3.7}$$

In the case of the nodes that are on the boundaries, we have

$$C_{Js}\partial_t^2\Phi_1 + \frac{1}{L_{Js}(\Phi_s)}\Phi_1 + \frac{1}{lx_0}\left(\Phi_1 - \Phi_2\right) + cx_0\partial_t^2\Phi_1 = 0 \tag{3.8}$$

for $n = 1$, and

$$\frac{1}{lx_0}\left(\Phi_{N-1} - \Phi_N\right) = 0 \tag{3.9}$$

for the case of $n = N$. We could directly rewrite these as a wave equation with time dependent boundary conditions, but here we choose to proceed slightly differently, by calculating the corresponding Lagrangian, taking the limit of small cell dimensions x_0, and only then writing down the corresponding equations of motion. Integrating Eqs. 3.7, 3.8 and 3.9 leads to a Lagrangian

$$L = \left(\frac{C_{Js}}{2}(\partial_t\Phi_1)^2 - \frac{1}{2L_{Js}(\Phi_s)}\Phi_1^2\right) \tag{3.10}$$

$$+ \sum_{n=1}^{N-1}\left(\frac{cx_0}{2}(\partial_t\Phi_n)^2 - \frac{1}{2lx_0}(\Phi_n - \Phi_{n+1})^2\right). \tag{3.11}$$

In the continuum limit, where $x_0 \to 0$, the above expression can be rewritten in terms of the Lagrangian density

$$\mathcal{L} = \delta(x)\left(\frac{C_{Js}}{2}(\partial_t\Phi)^2 - \frac{1}{2L_{Js}(\Phi_s)}\Phi^2\right) \tag{3.12}$$

$$+ \Theta(x)\left(\frac{c}{2}(\partial_t\Phi)^2 - \frac{1}{2l}(\partial_x\Phi)^2\right), \tag{3.13}$$

where we have taken $\Theta(x)$ to represent the Heaviside function

$$\Theta(x) = \begin{matrix} 1 & \text{if } x > 0 \\ 0 & \text{if } x \leq 0, \end{matrix} \tag{3.14}$$

and where the total Lagrangian for the system is equivalent to $L = \int_0^{x_l} dx\mathcal{L}$. It is implicitly assumed that the now continuous flux Φ is a function of both the coordinate x and time t. We can use this expression to also calculate a corresponding (classical) Hamiltonian. To do this, we define the canonical momentum conjugate to the flux Φ (which in our physical system can be thought of as charge density along the stripline cavity) as

$$\begin{aligned} Q &= \frac{\partial \mathcal{L}}{\partial\left(\partial_t \Phi\right)} \\ &= \left(\delta(x) C_{Js} + \Theta(x) c\right) \partial_t \Phi \\ &= w(x) \partial_t \Phi, \end{aligned} \tag{3.15}$$

where we have defined a weight function $w(x) = (\delta(x)C_{Js} + \Theta(x)c)$. Hence the total Hamiltonian for the DC–SQUID and cavity circuit can be written as

$$\begin{aligned} H_{\mathrm{sq}} + H_{\mathrm{cav}} + H_{\mathrm{sq-cav}} &= \int_{-\infty}^{x_l} dx (\partial_t \Phi) Q - \mathcal{L} \\ &= \int_{-\infty}^{x_l} dx \left[\delta(x) \left(\frac{C_{Js}}{2} (\partial_t \Phi)^2 + \frac{1}{2L_{Js}(\Phi_s)} \Phi^2 \right) \right. \\ &\quad \left. + \Theta(x) \left(\frac{c}{2} (\partial_t \Phi)^2 + \frac{1}{2l} (\partial_x \Phi)^2 \right) \right]. \end{aligned} \tag{3.16}$$

Naturally the last two lines could be written in terms of Q, but here, for later convenience, we express them only in terms of the flux Φ. Next, using Eq. 3.13 we can write down the Euler–Lagrange equation of motion (but this time not in terms of node fluxes Φ_n, but instead in terms of the continuous Φ). This leads to

$$\Theta(x) c \partial_t^2 \Phi + \delta(x) C_{Js} \partial_t^2 \Phi - \frac{1}{l} \partial_x \left(\Theta(x) \partial_x \Phi \right) + \delta(x) \frac{1}{L_{Js}(\Phi_s)} \Phi = 0. \tag{3.17}$$

It is clear that for $x > 0$, Eq. 3.17 reduces to a standard wave equation

$$c \partial_t^2 \Phi - \frac{1}{l} \partial_x^2 \Phi = 0, \tag{3.18}$$

allowing us to define the propagation velocity as $v = \sqrt{1/lc}$. In the case of $x = 0$, we can integrate Eq. 3.17 from $x = -\varepsilon$ to $x = \varepsilon$ and take the limit of $\varepsilon \to 0$, which gives

$$C_{Js} \partial_t^2 \Phi + \frac{1}{L_{Js}(\Phi_s)} \Phi - \frac{1}{l} \partial_x \Phi \bigg|_{x=0} = 0. \tag{3.19}$$

This equation represents the dynamic property of the boundary condition, hinted at earlier, which is a consequence of having a DC–SQUID located at a $x = 0$. Since we treat the other end of the cavity to be open, at x_l we have a current node. Mathematically we can represent it as

$$\partial_x \Phi \bigg|_{x=x_l} = 0. \tag{3.20}$$

Our goal is to find the normal modes of this system. To do this, first we note that Eq. 3.17 can be rewritten in a following form

$$-\frac{1}{l}\partial_x\left(\Theta(x)\partial_x\Phi\right)+\delta(x)\frac{1}{L_{Js}(\Phi_s)}\Phi=-w(x)\partial_t^2\Phi. \tag{3.21}$$

Next, we can decompose $\Phi=\Phi(x,t)$ into yet to be determined normal modes, while separating the dependence on x and t. Letting

$$\begin{aligned}\Phi(x,t)&=\sum_n\Phi_n(x,t)\\&=\sum_n\varphi_n(t)u_n(x),\end{aligned} \tag{3.22}$$

and substituting it into Eq. 3.21, we arrive at two differential equations

$$\partial_t^2\varphi_n(t)=-\omega_n^2\varphi_n(t), \tag{3.23}$$

as well as

$$-\frac{1}{l}\partial_x\left(\Theta(x)\partial_x u_n(x)\right)+\delta(x)\frac{1}{L_{Js}(\Phi_s)}u_n(x)=\omega_n^2 w(x)u_n(x), \tag{3.24}$$

where we have introduced a constant ω_n^2, which is an eigenvalue in both Eqs. 3.23 and 3.24. Solutions to Eq. 3.23 are easily determined to be proportional to $e^{\pm i\omega_n t}$. In order to calculate $u_n(x)$, we make the ansatz

$$u_n(x)=\eta_n\cos\left(\frac{\omega_n}{v}x+\theta_n\right), \tag{3.25}$$

where η_n and θ_n are to be determined. We then substitute the ansatz into the boundary conditions shown in Eqs. 3.19 and 3.20. This leads to the equations that describe the relationship between ω_n and θ_n, namely

$$\theta_n=\tan^{-1}\left(C_{Js}Z_0\frac{\omega_n^2-\omega_s(\Phi_s)^2}{\omega_n}\right) \tag{3.26}$$

$$\omega_n=\frac{v}{x_l}\left(n\pi-\theta_n\right), \tag{3.27}$$

with n integer. Here $\omega_s(\Phi_s)=1/\sqrt{C_{Js}L_{Js}(\Phi_s)}$ is the natural frequency of the DC–SQUID (dependent on the applied flux Φ_s), and $Z_0=\sqrt{l/c}$ the impedance of the waveguide.

Next, we need to ensure that each u_k is normalized with respect to the weight function $w(x)$. This implies

$$\int_{-\infty}^{x_l} u_n(x) u_{n'}(x) w(x) dx = \delta_{n,n'}, \tag{3.28}$$

noting that we have taken the lower limit to $-\infty$, since the weight function $w(x)$ is zero outside of the cavity. Enforcing the equation above, leads to

$$\eta_n = \left(\frac{C_t}{2} + C_{Js} \cos^2 \theta_n + \frac{1}{4Z_0 \omega_n} \sin 2\theta_n \right)^{-\frac{1}{2}} \tag{3.29}$$

where we have defined $C_t = cx_l$ to be the total capacitance of the cavity. A detailed justification is shown in Appendix A. Hence combining Eqs. 3.22 and 3.29 gives us a full normalized spectrum of normal modes that satisfy Eq. 3.24 along with the specified boundary conditions.

We are now ready to quantize the Hamiltonian presented in Eq. 3.16. The first step, is to promote Φ and Q to operators and insist that the standard commutation relations are satisfied. Namely

$$\begin{gathered} [\hat{\Phi}(x,t), \hat{Q}(x',t)] = i\hbar\delta(x - x') \\ [\hat{\Phi}(x,t), \hat{\Phi}(x',t)] = [\hat{Q}(x,t), \hat{Q}(x',t)] = 0. \end{gathered} \tag{3.30}$$

We stress that for the sake of brevity, we will neglect the operator notation (i.e. the ˆ symbol) from now on, and unless otherwise stated, both Φ and Q will be assumed to be quantum operators and not classical quantities. Next, expanding the flux along the cavity in terms of the newly calculated normal modes, we can write

$$\Phi(x,t) = \sum_n N_n \left(u_n(x) e^{-i\omega_n t} a_n + u_n^*(x) e^{i\omega_n t} a_n^\dagger \right) \tag{3.31}$$

where N_n is a normalization constant and a_n and $a_n^\dagger$ are lowering and raising operators of the nth mode respectively. By defining an $N_n = \sqrt{\hbar/2\omega_n}$ and insisting that the operators a_n satisfy

$$\begin{aligned} \left[a_n, a_{n'}^\dagger\right] &= \delta_{n,n'} \\ [a_n, a_{n'}] = \left[a_n^\dagger, a_{n'}^\dagger\right] &= 0, \end{aligned} \tag{3.32}$$

we note that our choice of the expansion in Eq. 3.31 satisfies 3.30.

Our final step consists of rewriting the Hamiltonian presented in Eq. 3.16 in a more convenient form, in terms of a_n and $a_n^\dagger$. While we could directly substitute Eq. 3.31 into 3.16 and simplify, it is more convenient to use a trick described in [130]. First let us consider the last term of Eq. 3.16. Integrating it by parts leads to

$$\frac{1}{2l}\int_{-\infty}^{x_l} dx\Theta(x)\left(\partial_x\Phi\right)^2 = \frac{1}{2l}\left(\Phi\Theta(x)\partial_x\Phi\right)\Big|_{-\infty}^{x_l} - \frac{1}{2l}\int_{-\infty}^{x_l} dx\Phi\partial_x\left(\Theta(x)\partial_x\Phi\right). \quad (3.33)$$

The first term vanishes due to the boundary condition from Eq. 3.20 and the fact that $h(0) = 0$, while the second term can be rewritten using Eq. 3.17. Hence we have

$$\frac{1}{2l}\int_{-\infty}^{x_l} dx\Theta(x)\left(\partial_x\Phi\right)^2 = -\frac{1}{2}\int_{-\infty}^{x_l} dx\left(w(x)\Phi\partial_t^2\Phi + \delta(x)\frac{1}{L_{Js}}\Phi^2\right). \quad (3.34)$$

Substituting this expression back into Eq. 3.16, gives a much simpler form for the Hamiltonian, namely

$$H_{\rm sq} + H_{\rm cav} + H_{\rm sq-cav} = \int_{-\infty}^{x_l} dx\ \frac{1}{2}w(x)\left((\partial_t\Phi)^2 - \Phi\partial_t^2\Phi\right). \quad (3.35)$$

Finally, using the normalization condition from Eq. 3.28 along with Eq. 3.31, we can write down the Hamiltonian for the cavity and the DC–SQUID as a sum of simple harmonic oscillators

$$H_{\rm sq} + H_{\rm cav} + H_{\rm sq-cav} = \sum_n \hbar\omega_n\left(a_n^\dagger a_n + \frac{1}{2}\right). \quad (3.36)$$

We stress that the normal mode structure that we have calculated in this section is exact, as long as the DC–SQUID is operated in its linear regime (and treated as a single degree of freedom). It is however important to note that the actual functional form of the nth mode (i.e. $u_n(x)$), can only be calculated numerically, as for a set of fixed physical parameters (inductances, capacitances, flux Φ_s), in order to obtain θ_n and ω_n, one needs to simultaneously solve Eqs. 3.26 and 3.27, which do not have a general, analytical solution. Furthermore, the expressions above could be simplified in certain parameter regimes. For example, in typical experiments the total cavity capacitance $C_t = lx_l$, is large relative to junctions capacitances, namely $C_t \gg C_{Js}$, which would let us simplify η_n from Eq. 3.29. We however, in this current work make no approximations to the normal mode profiles used.

Our next step is to consider the addition of a qubit, which we cover in the next section.

3.5 Charge Qubit

In this section, we consider a charge qubit centered around $x = x_q$ and coupled capacitively to the stripline cavity. A schematic that shows this setup is presented in Fig. 3.2(b). In our initial treatment we will neglect the spatial extension of the qubit, and assume it couples to the cavity only at a single point. In Sec. 3.7 however, we will briefly discuss the consequences of this assumption and describe a more realistic approach. The case of a charge qubit coupled to a superconducting waveguide has been studied by various authors [7, 124], but we review it, as in our case we will include the contributions of the $\mathbf{A^2}$–like term, which was already discussed in Sec. 3.2.

Using standard circuit analysis methods described in Chapter 2, and following [7], we can write the Hamiltonian of a charge qubit coupling to the cavity depicted in Fig. 3.2(b) as

$$H_q + H_{\text{q}-\text{cav}} = \frac{1}{2C_\Sigma}\left(C_g V_{\text{cav}} + Q_q\right)^2 - I_{0q}\phi_0 \cos\left(\frac{\Phi_q}{\phi_0}\right), \tag{3.37}$$

where, Φ_q and Q_q are respectively the flux and charge at the node labeled q in Fig. 3.2(b). I_{0q} and C_{Jq} are the critical current and capacitance of the Josephson junction, C_g is a capacitor that couples the qubit island (node "q") to the stripline cavity and finally[2] $C_\Sigma = C_g + C_{Jq}$. V_{cav} represents the cavity voltage, for now strictly at the center of the qubit, at $x = x_q$ (although as already outlined, we will discuss the consequence of the qubit having finite size in Sec. 3.7). We assume that V_{cav} contains both an AC contribution coming from the fluctuations of the various field modes inside the cavity, as well as a DC component that can be used to rotate the qubit [3].

It is convenient to rewrite this expression in terms of the excess Cooper pair number operator $n = \frac{1}{2e}Q_q$ and its conjugate phase $\varphi = \Phi_q/\phi_0$. Also taking $n_{\text{cav}} = -\frac{1}{2e}C_g V_{\text{cav}}$, $E_c = \frac{e^2}{2C_\Sigma}$ and $E_{Jq} = I_{0q}\phi_0$ lets us write the Hamiltonian in a standard form [7, 11, 125]

$$H_q + H_{\text{q}-\text{cav}} = 4E_c\left(n - n_{\text{cav}}\right)^2 - E_{Jq}\cos\varphi. \tag{3.38}$$

---

[2] A more detailed analysis presented (for example) in [76] or [103], shows that in reality the presence of the stripline cavity changes the effective values of capacitors C_g and C_{Jq} and therefore $C_{\sum}$. Likewise the presence of the qubit slightly renormalizes the effective value of c — the capacitance per unit length of the cavity. The final functional form of the Hamiltonian is however, not affected, and is still as shown in Eq. 3.37. Furthermore, in the limit of a long cavity (where $x_l c \gg C_g, C_{Jq}$), these expressions for the effective capacitances simply reduce back to actual C_g and C_{Jq}. Since in our case, of particular interest is the ratio between C_g and $C_{\sum}$ (defined as β in main text), as well as the resulting $C_{\sum}$, which determines the charging energy E_c, as long as we choose realistic values for those parameters we can safely neglect the minor effects of the capacitance redefinitions.

[3] We could imagine a slightly more complicated setup with a separate DC voltage source to control the qubit, as was shown explicitly in a case of a simpler circuit in Sec. 2.3.1 as well as studied in [124]. This is however not necessary as the Hamiltonian of such a circuit can be reduced to Eq. 3.37 by an appropriate choice of capacitance values. We therefore simply assume that $V_{\text{cav}} = V_{\text{dc}} + V_{\text{ac}}$, with V_{ac} treated as a quantum degree of freedom of the cavity field.

It is worth stressing that φ and n satisfy the commutation relation $[\varphi, n] = i$. The first term in Eq. 3.39 is equivalent to the momentum–vector potential coupling of an atom in a magnetic field $\frac{1}{2m}\left(\mathbf{p} - \frac{e}{c}\mathbf{A}\right)^2$, with n analogous to $\mathbf{p}$ and n_g analogous to $\mathbf{A}$. Following [7, 11], we can truncate the Hamiltonian to two levels. Assuming we operate the system in the regime $4E_c \gg E_J$, it is convenient to work in the Cooper pair number basis $|n\rangle$, the eigenstates of the n operator. Hence we can yet again rewrite the Hamiltonian as

$$H_q + H_{\text{q−cav}} = 4E_c \left(\sum_{n=-\infty}^{\infty} n|n\rangle\langle n| - n_{\text{cav}}|n\rangle\langle n| \right)^2 - \frac{1}{2} E_{Jq} \left(|n\rangle\langle n+1| + |n+1\rangle\langle n| \right). \tag{3.39}$$

It is easy to see that the expression above, is block–diagonal. We concentrate on a two consecutive energy levels, and without a loss of generality can chose those to be $n = 0$ and $n = 1$. This reduces Eq. 3.39 to

$$H_q + H_{\text{q−cav}} = 4E_c \begin{pmatrix} n_{\text{cav}}^2 & 0 \\ 0 & (1 - n_{\text{cav}})^2 \end{pmatrix} - \frac{1}{2} E_{Jq} \sigma_x. \tag{3.40}$$

Following [7], and as was already discussed, we assume that the contributions to n_{cav} come from a DC bias as well as from the fluctuations inside the cavity. This lets define $n_{\text{cav}} = n_{\text{dc}} + n_{\text{ac}}$, with n_{ac} representing an operator on the degrees of freedom of the cavity — in particular $n_{\text{ac}} \sim \sum_n \left(a_n^\dagger - a_n\right)$. The Hamiltonian then becomes

$$H_q + H_{\text{q−cav}} = -\frac{1}{2} E_{Jq} \sigma_x - 2E_c(1 - 2n_{\text{dc}})\sigma_z - 4E_c \left(1 - 2n_{\text{dc}} - \sigma_z\right) n_{\text{ac}} + 4E_c n_{\text{ac}}^2, \tag{3.41}$$

where we have neglected constant terms, as well as terms that depend only on n_{dc}, since for a fixed n_{dc} their contribution to the energy shift will be the same (even for varying boundary conditions of the stripline cavity, which will cause n_{ac} to change). Next, following [7], we do a change of basis, by diagonalizing the first two terms (i.e. the qubit part) of Eq. 3.41. We chose new basis defined by $|1'\rangle = \cos(\theta_q/2)|0\rangle + \sin(\theta_q/2)|1\rangle$ and $|0'\rangle = -\sin(\theta_q/2)|0\rangle + \cos(\theta_q/2)|1\rangle$, with $\tan\theta_q = E_{Jq}/(4E_c(1-2n_{\text{dc}}))$. Further taking $\omega_q = \sqrt{E_{Jq}^2 + (4E_c(1-2n_{\text{dc}}))^2}/\hbar$, we can write (now in $\{|0'\rangle, |1'\rangle\}$ basis)[4]

$$H_q + H_{\text{q−cav}} = \frac{\omega_q}{2}\sigma_z - 4E_c \left(1 - 2n_{\text{dc}} + \cos(\theta_q)\sigma_z + \sin(\theta_q)\sigma_x\right) n_{\text{ac}} + 4E_c n_{\text{ac}}^2. \tag{3.42}$$

We imagine operating the qubit near the DC bias of 1/2, and rewrite $n_{\text{dc}} = 1/2 +$

---

[4] Our choice of the qubit Hamiltonian digonalization transforms σ_z to $-\cos\theta_q\sigma_z - \sin\theta_q\sigma_x$, which is different from [7].

δn_{dc}, which leads to $\theta_q = \arctan\left(-\frac{E_{Jq}}{8E_c\delta n_{\mathrm{dc}}}\right)$, $\omega_q = \sqrt{E_{Jq}^2 + (8E_c n_{\mathrm{dc}})^2}/\hbar$ and

$$H_q + H_{\mathrm{q-cav}} = \frac{\omega_q}{2}\sigma_z - 4E_c\left(-2\delta n_{\mathrm{dc}} + \cos(\theta_q)\sigma_z + \sin(\theta_q)\sigma_x\right) n_{\mathrm{ac}} + 4E_c n_{\mathrm{ac}}^2. \quad (3.43)$$

We note that when the qubit is at its optimal point, where $\delta n_{\mathrm{dc}} = 0$, the Hamiltonian reduces to the typical case considered in atomic physics (for example in [1]). However in a more general situation where δn_{dc} is nonzero, we have other contributions which come from the $\delta n_{\mathrm{dc}} n_{\mathrm{ac}}$ and $\sigma_z n_{\mathrm{ac}}$ terms.

Next, we introduce $\beta = C_g/C_\Sigma$, and note that $4E_c n_{\mathrm{ac}} = -e\beta V_{\mathrm{ac}}$, with e representing the fundamental charge. Then, clearly $4E_c n_{\mathrm{ac}}^2 = (4E_c n_{\mathrm{ac}})^2/(\hbar\gamma) = (e\beta V_{\mathrm{ac}})^2/(\hbar\gamma)$, where we chose $\gamma = 4E_c/\hbar$. Finally, combining results from Sec. 3.4 where we calculated the flux along the cavity, and using the fact that $V_{\mathrm{ac}} = \partial_t \Phi(x,t)$, we arrive at

$$\begin{aligned} H_q + H_{\mathrm{q-cav}} =& \frac{\omega_q}{2}\sigma_z + i\hbar\sum_k g_k^{(-)}\left(a_k^\dagger - a_k\right)\left(2\delta n_{dc} - \cos(\theta_q)\sigma_z - \sin(\theta_q)\sigma_x\right) \\ &+ \frac{\hbar}{\gamma}\left(\sum_k i g_k^{(-)2}\left(a_k^\dagger - a_k\right)\right)^2, \end{aligned} \quad (3.44)$$

with

$$g_k^{(-)} = \frac{|e|\beta}{\hbar}\sqrt{\frac{\hbar\omega_k}{2}}\left(\frac{C_t}{2} + C_{Js}\cos^2\theta_k + \frac{1}{4Z_0\omega_k}\sin 2\theta_k\right)^{-\frac{1}{2}}\cos\left(\frac{\omega_n}{v}x_q + \theta_k\right). \quad (3.45)$$

The "$(-)$" superscript on g_k is to stress that the qubit here couples to the operators $(a_k^\dagger - a_k)$. These expressions, along with Eq. 3.36 lead to a full description of our system.

3.6 Energy Shift with Perturbation Theory

In this section we will look at a perturbative correction to the energy levels of our system. While of particular interest will be the energy shift of the qubit's ground state, we will initially derive the energy correction for a general thermal state, and only at the end consider that special case. Let us begin with a general Hamiltonian

$$H = H_0 + V. \quad (3.46)$$

We treat the H_0 as the nonperturbed contribution

$$H_0 = \hbar \sum_k \omega_k \left(a_k^\dagger a_k + \frac{1}{2} \right) + \hbar \sum_m \varepsilon_m |m\rangle\langle m|, \tag{3.47}$$

and V as a perturbation described by

$$\begin{aligned} V =& \hbar \sum_m x_{m,m+1} \sigma_x^m \left(\sum_k g_k^{(\pm)} i^{\frac{1\mp1}{2}} \left(a_k^\dagger \pm a_k \right) \right) \\ & + \hbar \sum_m z_m |m\rangle\langle m| \left(\sum_k g_k^{(\pm)} i^{\frac{1\mp1}{2}} \left(a_k^\dagger \pm a_k \right) \right) \\ & + \frac{\hbar}{\gamma} \left(\sum_k g_k^{(\pm)} i^{\frac{1\mp1}{2}} \left(a_k^\dagger \pm a_k \right) \right)^2 . \end{aligned} \tag{3.48}$$

For the sake of generality, we treat the qubit, as a more general qudit, occupying a d–dimensional Hilbert space. We define $\sigma_x^m = \sigma_+^m + \sigma_-^m$ with $\sigma_-^m = |m\rangle\langle m+1| = \left(\sigma_+^m\right)^\dagger$ and ε_m as the frequency of the mth level of the qudit (with $\varepsilon_{m+1} > \varepsilon_m$). $x_{m,m+1}$ and z_m are treated as dimensionless quantities that allow for level dependent coupling differences between levels m and $m+1$, as well as varying scaling between different energy levels (anharmonicity) respectively. We assume that $x_{m,m+1} = x_{m+1,m}$ for all m. γ has units of frequency and ensures that the third term in Eq. 3.48 has the correct dimensions. Finally, we stress that using terms like $g_k^{(\pm)} i^{\frac{1\mp1}{2}} \left(a_k^\dagger \pm a_k \right)$ lets us easily study both cases of the qudit coupling to flux (i.e. $a_k^\dagger + a_k$) as well as charge (i.e. $i(a_k^\dagger - a_k)$) along the cavity simultaneously (although we only show explicit results for latter scenario). It is clear from Eq. 3.48 that the perturbation will only couple neighbouring energy levels, both in the qudit's as well as the cavity oscillators' Hilbert spaces. In order to be consistent with the discussion in Sec. 3.2, we label the first and second terms of Eq. 3.48 as the paramagnetic, while the last term as diamagnetic. We will later map this general Hamiltonian from Eq 3.46 to the one obtained in Sections 3.4, 3.5.

The energy shift of a state $|s\rangle$ due to a perturbation V can be written as

$$\delta E_s = \lambda \langle s|V|s\rangle + \lambda^2 \sum_{k \neq s} \frac{|\langle k|V|s\rangle|^2}{E_s - E_k} + \mathcal{O}\left(\lambda^3\right), \tag{3.49}$$

where λ is a “small parameter”. This expression is valid when the various energy levels are non–degenerate.

Our initial goal is to calculate the energy shift of a mixed state described as

$$\rho =|q\rangle\langle q| \prod_{n_i} \otimes \sum_{n_i} P_{n_i}|n_i\rangle\langle n_i|. \tag{3.50}$$

Here, the qudit is assumed to be in a state $|q\rangle$, while the oscillators in their respective thermal states[5]. Here $P_{n_i} = (1 - e^{-\frac{\hbar\omega_i}{k_B T}})e^{-\frac{n_i\hbar\omega_i}{k_B T}}$ represents the probability that ith mode is occupied with n photons.

In order to calculate the energy shift to a state ρ, we will first neglect the effects of temperature and consider a much simpler case with only two cavity modes present. The resulting correction will then be easily generalized to the more elaborate scenario of Eq. 3.50. Hence let us begin with a state $|q, n_1, n_2\rangle$. q here represents the qth level of the qudit, while n_1 and n_2 the nth levels of the cavity modes 1 and 2 respectively.

Since the diamagnetic and paramegnetic terms are of different orders in $g_k^{(\pm)}$, and we are only interested in corrections up to second order in $g_k^{(\pm)}$, we can easily see that in the case of the first term of Eq. 3.49 only the diamagnetic term will be relevant, while in the case of the second term of Eq. 3.49 only the paramagnetic terms will be of importance. This lets use calculate shift contributions separately.

The details of the following calculations are shown in Appendix B, while in this section, for brevity, we only present the key results. In the case of the diamagnetic portion of the perturbation Hamiltonian, we have

$$\delta E^{\text{diam}}_{q,n_1,n_2} = \frac{\hbar}{\gamma} \sum_{k=1,2} g_k^{(\pm)2}(2n_k + 1). \tag{3.51}$$

The next step is to look at the paramagnetic terms and calculate how they contribute to the energy shift. As before, using Eqs. 3.48 and 3.49 we arrive at

$$\begin{aligned}\delta E^{\text{param}}_{p,n_1,n_2} =&\hbar \sum_{j=+1,-1} \sum_{k=1,2} |x_{q,q+j}|^2 g_k^{(\pm)2} \left(\frac{n_k + 1}{(\varepsilon_q - \varepsilon_{q+j}) - \omega_k} + \frac{n_k}{(\varepsilon_q - \varepsilon_{q+j}) + \omega_k} \right) \\ &- \hbar|z_q|^2 \sum_{k=1,2} \frac{g_k^{(\pm)2}}{\omega_k},\end{aligned} \tag{3.52}$$

where we have assumed that $g_k^{(\pm)}$ is real. Hence the total shift to the state $|q, n_1, n_2\rangle$

---

[5] A more realistic scenario would be to consider a possibility of the qudit also being in a thermal state. For the sake of simplicity however, we will assume that $k_B T \ll \hbar(\varepsilon_{q+1} - \varepsilon_q)$, while the energy of the lowest energy modes in the cavity may be of the order of $k_B T$, and hence the nonzero temperature correction might be relevant.

can be written as

$$\delta E_{q,n_1,n_2} = \delta E^{\text{param}}_{q,n_1,n_2} + \delta E^{\text{diam}}_{q,n_1,n_2}, \tag{3.53}$$

with $\delta E^{\text{param}}_{q,n_1,n_2}$ and $\delta E^{\text{diam}}_{q,n_1,n_2}$ from Eqs. 3.52 and 3.51 respectively. It is easy to see that this expression trivially generalizes to an arbitrary number of oscillators — hence in order to consider all modes in the cavity, we can take k to vary between 1 and ∞.

Next, we imagine that instead of a pure state where the kth mode has n_k photons, each mode is in a thermal state at temperature T. Hence the energy shift for a given fixed set of n_ks now gets a weight that corresponds to the probability of it occurring. The generalized shift can then be written as

$$\langle \delta E_{q,n_1,n_2,\ldots} \rangle = \sum_{n_1,n_2,\ldots} (P_{n_1} P_{n_2} \ldots) \delta E_{q,n_1,n_2,\ldots}. \tag{3.54}$$

Noting that the average occupation of the kth mode can be written as $\langle n_k \rangle = \sum_{n_k} P_{n_k} n_k$, with $\sum_{n_k} P_{n_k} = 1$, this expression reduces to

$$\begin{aligned} \delta E_q = \hbar \sum_{j=+1,-1} \sum_{k} x^2_{q,q+j} g_k^{(\pm)2} \left(\frac{\langle n_k \rangle + 1}{(\varepsilon_q - \varepsilon_{q+j}) - \omega_k} + \frac{\langle n_k \rangle}{(\varepsilon_q - \varepsilon_{q+j}) + \omega_k} \right) \\ - \hbar z_q^2 \sum_k \frac{g_k^{(\pm)2}}{\omega_k} + \frac{\hbar}{\gamma} \sum_k g_k^{(\pm)2} (2\langle n_k \rangle + 1). \end{aligned} \tag{3.55}$$

Here, we have simplified the notation, and defined $\delta E_q = \langle \delta E_{q,n_1,n_2,\ldots} \rangle$. The first two terms are due to the paramagnetic contributions in the coupling Hamiltonian, while the last term is due to the diamagnetic term.

In summary, we now have a very general expression for the energy shift of the state shown in Eq. 3.50. In the next section, we will concentrate on a particular case where the qudit is assumed to be in its ground state.

3.6.1 Ground State Energy Shift

In Sec. 3.9, we will revisit the general energy shift expression just calculated to look at a cavity boundary dependent Lamb shift, but in the context of the Casimir–Polder effect, of particular interest, is the case where the qudit is its ground state, namely where $q = 0$. Combing Eq. 3.55 along with the Hamiltonian calculated in Sections 3.4 and 3.5 and further defining $\omega_q = \varepsilon_1 - \varepsilon_0$ as well as $x_{0,1} = -\sin(\theta_q)$

and $z_0 = 2\delta n_{\rm dc} - \cos(\theta_q)$, we can write

$$\delta E_0 = -\hbar \sum_k g_k^{(\pm)2} \left(\sin^2\theta_q \left(\frac{\langle n_k\rangle + 1}{\omega_q + \omega_k} + \frac{\langle n_k\rangle}{\omega_q - \omega_k} \right) + \frac{(2\delta n_{\rm dc} - \cos\theta_q)^2}{\omega_k} - \frac{2\langle n_k\rangle + 1}{\gamma} \right). \tag{3.56}$$

First, it is important to stress that the expression above is not defined when $\omega_k = \omega_q$. This is a possibility when the temperature is nonzero and hence $\langle n_k\rangle \neq 0$. Furthermore, in order for the perturbative correction to be valid, we need to insist that $\langle n_k\rangle g_k^{(\pm)2}/|\omega_q - \omega_k| \ll \omega_k + \omega_q$. Hence, we need to keep this constraint in mind in the following sections, when considering realistic values for the various circuit parameters.

Finally it is important to stress that the sum we have just written down, not surprisingly, does not converge — this is true even in the case of zero temperature when all the $n_k = 0$. In a case of a charge qubit, in Sections 3.4 and 3.5, we showed that[6] $g_k^{(-)}$ scales like $\sqrt{\omega_k}$ with $\omega_k \sim k$, which clearly leads to both the paramagnetic as well as the diamagnetic sum contributions diverging. In the next section we will address this point, and discuss ways to remedy it, by accounting for the finite size of the qubit, as well as considering the dissipative nature of superconductors beyond certain energies.

3.7 Frequency Cutoff

In this section, we discuss two mechanisms which limit the total number of modes that contribute to the energy shift described in Sec. 3.6.1, and therefore allow the sum in Eq. 3.56 to converge. The first is related to the size of the qubit, and the second to the fact that at high energies, superconductors that make up the stripline cavity are no longer superconducting, produce dissipation, and that in turn can cause these high energy modes to decay. We furthermore stress that there should be a yet another, higher cutoff, mediated by the bulk plasma frequency of the superconductor, but we assume that it is much higher than the other two candidates and hence do not discuss it explicitly.

3.7.1 Spatial Dimensions of the Qubit

So far we have envisioned that the qubit has a point–like spatial distribution. This unrealistic assumption leads to a divergence when calculating the total contribution to the energy shift that accounts for the many–mode field inside the cavity. To

---

[6] In the case of a flux qubit, which couples to the current in the stripline cavity, we would have $g_k^{(+)}$, which just like $g^{(-)}$ scales as $\sqrt{\omega_k}$, and hence also leads to divergence.

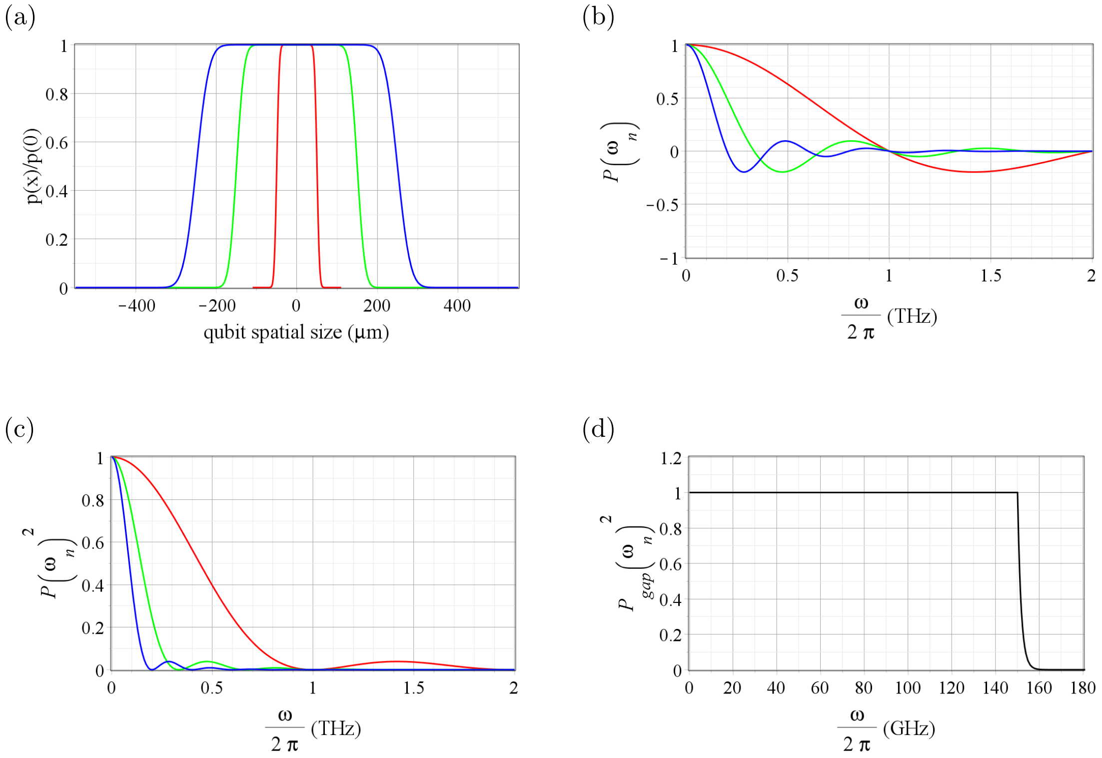

Figure 3.3: (a) Qubit spatial profile function $p(x)$ (scaled by $p(0)$) defined in Eq. 3.59 with $\sigma_{\text{rect}}, \sigma_{\text{Gauss}} = 100, 5\,\mu\text{m}$ (red curve), $\sigma_{\text{rect}}, \sigma_{\text{Gauss}} = 300, 15\,\mu\text{m}$ (green curve) and $\sigma_{\text{rect}}, \sigma_{\text{Gauss}} = 500, 25\,\mu\text{m}$ (blue curve). (b) $P(\omega_n)$ from Eq. 3.62 — a Fourier transform of the spatial profile function shown in (a). (c) $P(\omega_n)^2$, which is responsible in determining which cavity modes contribute to the energy shift due to the qubit–cavity interactions. Even in the case of a very large qubit size, we find that frequencies beyond 150 GHz could play a role. (d) A square of an alternative, phenomenological frequency cutoff function $P_{\text{gap}}(\omega_n)$ which is based on the argument that beyond the frequencies associated with twice the superconducting energy gap, the superconducting material used to build the circuit becomes dissipative, and causes high energy mode to "decay away". In this case, we assume the superconducting material is aluminum, with the energy gap of $\Delta_{\text{gap}}/2\pi\hbar \sim 75\,\text{GHz}$.

model the qubit's finite size, we imagine that the qubit is centered around x_q, and has a spatial distribution governed by some function $p(x-x_q)$. The coupling Hamiltonian we calculated in Sec. 3.5 , which assumed the qubit interacts with the cavity only at a single point x_q, has to then be integrated along x. Doing so, modifies Eq. 3.44, such that $g_n^{(\pm)}$ is transformed to $g_n^{(\pm)}P(\omega_n)$, where $P(\omega_n)$ defines a spectral response function, and is the Fourier transform (with $\omega_n = k_n/v$, and k_n representing the wave number of the nth mode) of the spatial distribution function $p(x)$. This leads to $P(\omega_n)$ playing a role of a "filter" which determines how much the nth mode, at frequency ω_n, contributes to the total qubit–cavity coupling. Let us show this explicitly. In the case of charge qubit, from Sections 3.4 and 3.5, we see that the coordinate dependent term of the interaction Hamiltonian, for a given n, is simply $\cos\left(\frac{\omega_n}{v}x+\theta_n\right)$. Hence the total contribution to the coupling Hamiltonian is proportional to[7]

$$\begin{aligned}\int_{-\infty}^{\infty} p(x-x_q)\cos\left(\frac{\omega_n}{v}x+\theta_n\right)dx &= \frac{1}{2}\int_{-\infty}^{\infty} p(x-x_q)\left(e^{-i\left(\frac{\omega_n}{v}x+\theta_n\right)}+e^{i\left(\frac{\omega_n}{v}x+\theta_n\right)}\right)dx\\ &= \frac{1}{2}e^{-i\theta_n}\int_{-\infty}^{\infty} p(x-x_q)e^{-i\frac{\omega_n}{v}x}dx\\ &+\frac{1}{2}e^{i\theta_n}\int_{-\infty}^{\infty} p(x-x_q)e^{i\frac{\omega_n}{v}x}dx\\ &= \frac{1}{2}e^{i\theta_n+i\frac{\omega_n}{v}x_x}P\left(\frac{\omega_n}{v}\right)+\frac{1}{2}e^{i\theta_n+i\frac{\omega_n}{v}x_q}P\left(-\frac{\omega_n}{v}\right),\end{aligned} \tag{3.57}$$

where we have used a change of variables, and a definition of Fourier transform $\mathcal{F}(p(x)) = P(k_n) = \int_{-\infty}^{\infty} p(x)e^{-ik_nx}dx$, with $k_n = \omega_n/v$. If the profile is symmetric in frequency space (which we expect if we assume $p(x)$ is real–valued), namely if $P\left(\frac{\omega_n}{v}\right) = P\left(-\frac{\omega_n}{v}\right)$, we can rewrite the above as

$$\int_{-\infty}^{\infty} p(x-x_q)\cos\left(\frac{\omega_n}{v}x+\theta_n\right)dx = \cos\left(\frac{\omega_n}{v}x_q+\theta_n\right)P\left(\frac{\omega_n}{v}\right). \tag{3.58}$$

Hence in frequency space, the effect of the nontrivial spatial profile function is to scale the coupling strength $g_{n}(\pm)$ by a factor $P\left(\frac{\omega_n}{v}\right)$ — from now we will refer to this expression as only a function of ω_n, since we fix the speed of light in the cavity in all the following calculations.

Let us next consider a particular form of the spatial function $p(x)$ and calculate the corresponding $P(\omega_n)$. In the case of a charge qubit for example, we can assume that the coupling strength is mainly decided by the size of the coupling capacitor,

---

[7] The limits of integration in this integral should span over the full size of the cavity, namely between 0 and x_l. To simplify the calculation however, we will expand them to $-\infty$ and ∞ respectively. This approximation can be justified by noting that away from $x_q \pm \max(\sigma_{\text{Sigma}}, \sigma_{\text{rect}})$ the function $p(x)$ is small, and hence only contributes weakly to the total coupling.

and decays exponentially away from it. In a case where the qubit couples to the stripline cavity inductively, we would similarly expect that the coupling strength is largest for the portions of the cavity that is closest to the qubit loop and quickly decays for portions further away. To model this kind of behavior, we conveniently define $p(x)$ as by a convolution of a rectangular function with a Gaussian. Namely we take

$$p(x) = N \int_{-\infty}^{\infty} g_{\mathrm{rect}}(y) g_{\mathrm{Gauss}}(x-y) dy, \tag{3.59}$$

where N is a normalization constant and

$$g_{\mathrm{rect}}(x) = \Theta\left(x + \frac{\sigma_{\mathrm{rect}}}{2}\right) - \Theta\left(x - \frac{\sigma_{\mathrm{rect}}}{2}\right), \tag{3.60}$$

$$g_{\mathrm{Gauss}}(x) = e^{-\frac{x^2}{2\sigma_{\mathrm{Gauss}}^2}}, \tag{3.61}$$

with $\Theta(x)$ defined in Eq. 3.14, and σ_{rect} and σ_{Gauss} constants that ultimately determine the effective width of the qubit. We further choose the normalization N to satisfy $1 = \int_{-\infty}^{\infty} p(x) dx$, which for the case of $p(x)$ defined above leads to $N = \frac{1}{\sqrt{2\pi}} \frac{1}{\sigma_{\mathrm{rect}} \sigma_{\mathrm{Gauss}}}$. Hence putting it all together, the effective function $P(\omega_n)$ can be written as

$$P\left(\omega_n\right) = \frac{2v}{\sigma_{\mathrm{rect}} \omega_n} \exp\left(-\frac{\omega_n^2 \sigma_{\mathrm{Gauss}}^2}{2v^2}\right) \sin\left(\frac{\omega_n \sigma_{\mathrm{rect}}}{2v}\right). \tag{3.62}$$

Next, we can look at a few cases, each characterized by specific values of σ_{rect} and σ_{Gauss}. Fig. 3.3(a) shows $p(x)$ for $\sigma_{\mathrm{rect}}, \sigma_{\mathrm{Gauss}} = 100, 5\,\mu\mathrm{m}$ (red curve), $\sigma_{\mathrm{rect}}, \sigma_{\mathrm{Gauss}} = 300, 15\,\mu\mathrm{m}$ (green curve) and $\sigma_{\mathrm{rect}}, \sigma_{\mathrm{Gauss}} = 500, 25\,\mu\mathrm{m}$ (blue curve). Fig 3.3(b) shows the corresponding Fourier transforms presented in Eq. 3.62, and Fig. 3.3(c) $P(\omega_n)^2$, since we have already determined that the sum in the expression for δE_0 scales like $g_n^{(\pm)2}$, and hence like $P(\omega_n)^2$. From these plots, it is clear right away that in even in the case of largest qubit size considered ($\sigma_{\mathrm{rect}} = 500\,\mu\mathrm{m}$), the modes of frequencies greater than 150 GHz have an non negligible effect. In the case of the smaller, more realistically sized qubits, the spread of $P\left(\omega_n\right)$ is even greater, and in the case of the smallest qubit considered ($\sim 100\,\mu\mathrm{m}$), from plot in Fig. 3.3(c), frequencies up to as much as ~ 1 THz seem relevant. This brings us to our discussion of the second cutoff mechanism, which we consider next.

3.7.2 Dissipation of High Energy Modes

The arguments above, give an upper bound on the frequency cutoff, which puts a limit on which modes interact with the qubit. Here we mention another possible candidate that could have an impact on the shape of the spectral response function

$P(\omega_n)$. As was briefly discussed in Sec 2.1, beyond the frequencies associated with the superconducting gap (in particular beyond frequencies of the order $2\Delta_{\rm gap}/2\pi\hbar$), the material used to fabricate the cavity stops behaving like a superconductor. The result is that the high energy modes, beyond the gap, experience damping, which we can in turn associate with a frequency cutoff. One way to model this effect, at least classically, is analogous to what is considered in normal (non–superconducting) cavities or transmission lines. There, one can modify the description of the cavity shown in Fig. 3.2(a), and introduce series resistors along the inductors lx_0, as well as conductance shunting the capacitors cx_0 [78, 105]. The effect of such a change introduces a complex wave number, which then scales the normal modes by factors like[8] $\sim \exp(\pm\beta x)$ (the plus or minus signs corresponds to waves are traveling in the negative or positive directions respectively). The parameter β must clearly depend on the mode frequency as needs to be dominant only at frequencies beyond twice the superconducting gap. To our knowledge the precise structure of this dependence is currently not very well understood. In order to still model this cutoff behavior in our system however, we introduce a phenomenological version of the spectral response function $P(\omega_n)$, and define it as

$$P_{\rm gap}(\omega_n) = \Theta(\omega_n - \omega_{\rm gap}) \left(\exp\left(-\frac{\omega_n - \omega_{\rm gap}}{\gamma_{\rm gap}} \right) - 1 \right) + 1, \qquad (3.63)$$

with Θ, as before, the Heaviside function, $\omega_{\rm gap} = 2\Delta_{\rm gap}/\hbar$, and finally $\gamma_{\rm gap}$ representing a decay rate which governs how quickly higher energy modes stop being relevant. In the case of aluminum, we can take $\Delta_{\rm gap} = 3.4 \times 10^{-4}\,{\rm eV}$ [71], and conservatively approximate $\omega_{\rm gap}/2\pi = 150\,{\rm GHz}$. Assuming that the cutoff is "sharp", but stressing that its exact form is not entirely known, we further take $\gamma_{\rm gap}/2\pi = 1.5\,{\rm GHz}$. Fig. 3.3(d) shows an example of $P(\omega_n)^2$ from Eq. 3.62 with the parameters just outlined — we stress that the horizontal axis is in the units of THz as before. The resulting cutoff is dramatic and hence we can expect that the modes with frequencies beyond $\omega_{\rm gap}$ will have negligible on the total energy shift.

It is important to stress that our exact numerical results for the effective Casimir–Polder current discussed in the next section, will necessarily have a nontrivial dependence on just how we model the frequency cutoff, and therefore effectively how many cavity modes are considered to contribute to the qubit–cavity interaction. Given that our phenomenological model for how to treat the cutoff may be rather crude, an actual experimental realization of a measurement of a Casimir–Polder current discussed in the next section could, in principle at least, be helpful in shedding more light on how to best treat the frequency cutoff in superconducting circuit systems such as the one used here.

---

[8] In Sec. 3.4, we have written down the normal modes in terms of functions $\cos(k_n x + \theta_n)$, but they could clearly be rewritten in terms of functions $\exp(\pm k_n x)$.

3.8 Casimir–Polder Current — Results

We are finally ready to use the results from previous sections to discuss the Casimir–Polder current in our system. So far we have assumed that the flux through the boundary DC–SQUID is a fixed parameter. Following Casimir and Polder [19, 20] we now ask the question of what happens if this parameter is not fixed, but is instead allowed to vary (the implicit assumption here, is however that it can vary "slowly" on scales compared to dynamics of the cavity and qubit). In particular, in this section, we are interested in the variation due to the interaction energy between the stripline cavity and the qubit, which we have calculated in a form of the perturbative energy shift δE_0. Hence, in a way analogous to [1], we can define a Casimir–Polder current as a flux derivative of δE_0, namely[9]

$$I_{\mathrm{CP}} = -\frac{\partial \delta E_0}{\partial \Phi_s}. \tag{3.64}$$

Physically, I_{CP} can be interpreted as a current that is circulating around the DC–SQUID. In order to calculate the expression above, we need to sum all the mode contributions that make up δE_0. No closed form of Eq. 3.56 is known, but it can be calculated numerically. Once that is done, again numerically, we can differentiate it with respect to Φ_s in order to get I_{CP}, we have set out to calculate.

The actual value of I_{CP} that one obtains form our system is highly parameter–dependent. Ideally we would like this current to be as large as possible. In the next few sections we will look at how I_{CP} varies as we change different quantities, while keeping others fixed. Most of the discussion will also assume zero temperature, however in Sec. 3.8.4, under certain conditions, we will briefly consider the effects of this restriction being lifted.

There are certain sets of parameters that will stay constant for most of the discussion. For example we will assume that the same superconducting material is used in all cases. This fixes the values of inductance and capacitance per unit length, and hence both the speed of light in the stripline cavity and its characteristic impedance. We assume the material that makes up the circuit to be aluminum,

---

[9] To justify why the derivative shown in Eq. 3.64 represents the current around the DC–SQUID loop, we first note that the variable Φ_s is a flux that threads a *particular* circuit loop – namely the one of the boundary DC–SQUID. Furthermore, in the limit of small geometric inductance of the DC–SQUID (where $L_g \ll L_{J0}$), Φ_s is close to the total threaded flux (i.e., we assume that the small corrections due to the finite size of the geometric inductance, do not change the total loop flux by "much", meaning they do not change the structure of the normal modes in the cavity). This, along with the Feynman–Hellmann theorem [40, 61], which shows how in a quantum system, one can relate a generalized force (here a current) to an energy derivative with respect to a parameter (here a flux), we can conclude that Eq. 3.64 corresponds to the circulating current around the boundary DC–SQUID loop.

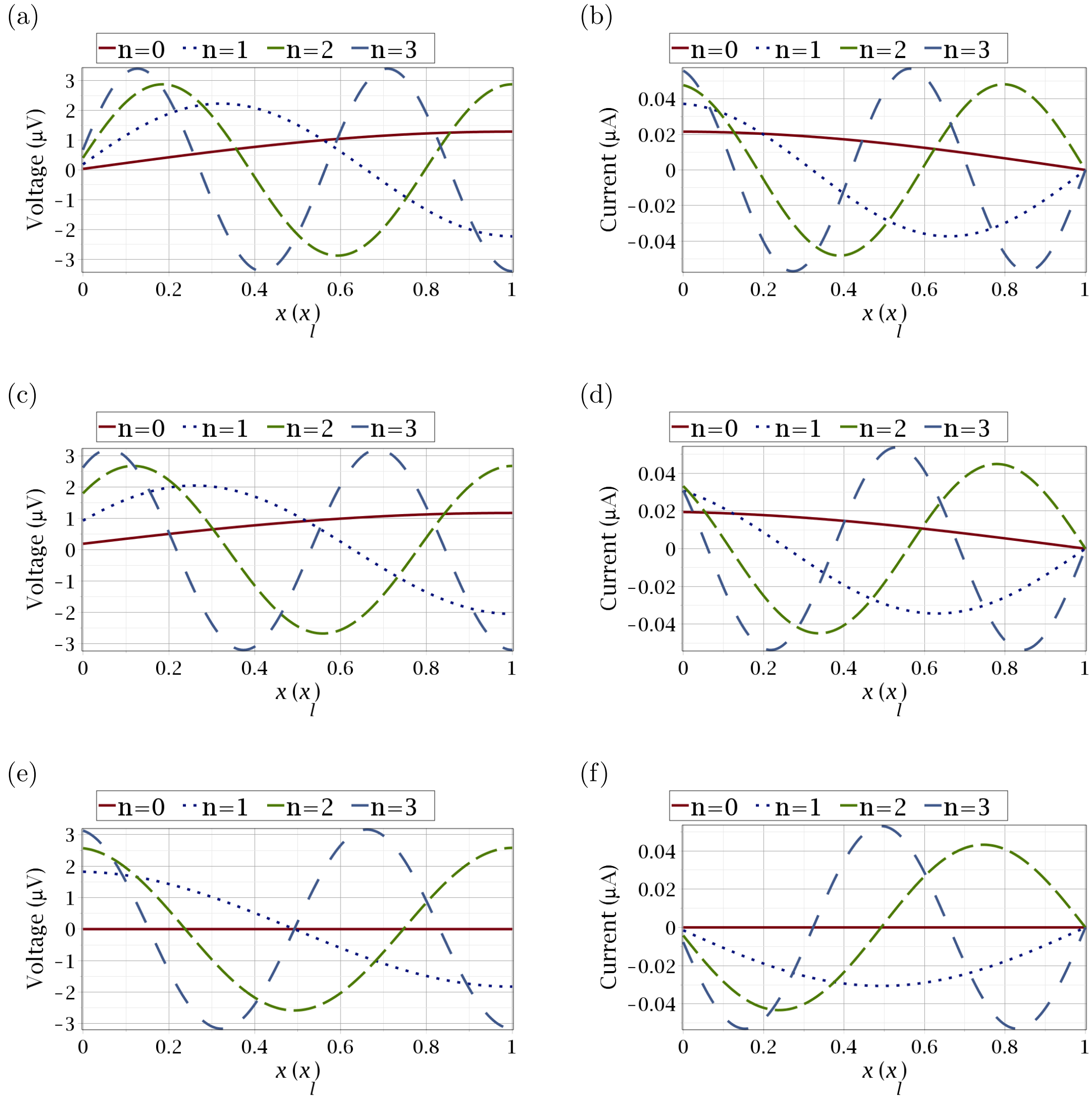

Figure 3.4: Profiles of the lowest four normal modes, ranging from $n = 0$ to $n = 3$, plotted as a ratio of the total stripline cavity length x_l. In the top row, plots (a-b) show results for the case of $f_s = 0$, in the middle row, plots (c-d) show the case of $f_s = 0.45$ and finally in the bottom row, plots (e-f) show the special case of $f_s = 0.5$. The left column shows the modes in terms of voltage (namely $\sqrt{\hbar\omega_n/2}u_n(x)$), while the right column the current ($\sqrt{\hbar/2\omega_n l^2}\partial_x u_n(x)$). The behavior of the modes is governed by the boundary conditions imposed on our system. See main text for discussion.

and take $l = 4.53 \times 10^{-7}\,\mathrm{H/m}$ and $c = 1.27 \times 10^{-10}\,\mathrm{F/m}$, values experimentally obtained in a similar system in [48]. These lead to $v = 1/\sqrt{cl} = 1.32 \times 10^{8}\,\mathrm{m/s}$ and $Z_0 = \sqrt{l/c} = 59.72\,\Omega$.

We will also mostly concentrate on a short stripline cavity, with $x_l = 0.01\,\mathrm{m}$, as is done many experimental setups. The main effect of x_l is to define the fundamental frequency of each mode, as can be observed from Eq. 3.27. Since we incorporate a frequency cutoff in our model, as was discussed in Sec. 3.7, keeping x_l small will keep the fundamental frequencies large, which will in turn limit the number of modes that contribute to the total energy shift δE_0. For example, with $x_l = 0.01\,\mathrm{m}$, with $P(\omega_n)$ as defined in Sec. 3.7, typically fewer than the lowest 30 modes end up having an effect on δE_0.

Another important parameter that will play a crucial role in the results is the plasma frequency of the DC–SQUID. It can be written as

$$\omega_s(\Phi_s) = \sqrt{|\cos(f_s\pi)|/L_{Js}C_{Js}}, \tag{3.65}$$

where as in other chapters, we have defined $f_s = \Phi_s/\Phi_0$. As was already hinted at in Sec. 3.4, this quantity plays a central role in our system, since it brings in the DC–SQUID flux dependence into the structure of the normal modes. We will use parameters that lead to $\omega_s(0)/2\pi = 107\,\mathrm{GHz}$, an experimentally easily realizable value. Clearly as the flux through the DC–SQUID changes, this quantity will decrease and be minimized at $f_s = \pm 0.5$. It is useful to understand just how different values of the DC–SQUID flux affect the structure of the different mode profiles. Fig. 3.4 shows a few lowest energy modes, starting with $n = 0$ up to $n = 3$. In the top row, plots (a-b) show results for the case of $f_s = 0$, in the middle row, plots (c-d) show the case of $f_s = 0.45$ and finally in the bottom row, plots (e-f) show the special case of $f_s = 0.5$. The left column shows the modes in terms of voltage (namely $\sqrt{\hbar\omega_n/2}u_n(x)$), while the right column the current ($\sqrt{\hbar/2\omega_n l^2}\partial_x u_n(x)$). The behavior of the modes is clearly governed by the boundary conditions imposed on our system. In the case of $f_s = 0$, the frequency of the modes shown is much lower than the value of $\omega_s(0)$, and hence the left boundary, at $x = 0$ is seen by these low energy modes as a (approximately) closed circuit, where the voltage is close to zero. It is worth stressing however that as n increases we see that the mode voltage at the left boundary tends to stray away from zero. This is because as n increases, the mode frequency ω_n increases, and therefore gets closer to the DC–SQUID plasma frequency $\omega_s(0)$, which results in the mode phase shift θ_n moving away from the value of $-\pi/2$ (see Eqs. 3.26 and 3.27). The boundary at $x = x_l$ on the other hand, was assumed to be an open circuit, with the boundary condition resulting in the current there being 0. This is fully consistent with the plots in the top row.

As we start varying the flux towards $f_s = 0.45$ in plots (c-d) and further towards $f_s = 0.5$ in (e-f) the effective plasma frequency of the DC–SQUID is lowered, and therefore, for the same reasons just outlined (since the mode frequencies are now of the same order as the effective plasma frequency) even the low frequency modes do not see the boundary as simply a closed circuit, but instead each mode gets a different phase shift, and hence sees the boundary differently. We will see in the next few sections, that this dependence of the mode profile structure, in particular near $f_s = 0.5$, will play a central role in our calculations of I_{CP}.

3.8.1 Varying qubit position x_q

The first set of results we will examine, consist of studying how the Casimir–Polder current I_{CP} changes as we vary the ratio between the position of the qubit in the stripline cavity and the cavity length — namely x_q/x_l. The results, for the set of parameters discussed in the last section, and with the qubit bias δn_{dc} set to zero, is shown in Fig 3.5. Both plots (a) as well as (b) show the same dataset, but in different formats, and the currents are presented in the units of nano Amperes. In the figure, we vary x_q/x_l between values of 0.1 and 0.9. We stay away from cases of $x_q/x_l = 0$ and $x_q/x_l = 1$ in order to safely neglect any potential boundary effects and account for the qubit's finite size. Furthermore, we stay away from the flux $|f_s| = 0.5$, in order to keep our 1d model description of the DC–SQUID valid.

From the plots, we see that in general, the magnitude of I_{CP} tends to get larger as the qubit gets closer to the boundary at $x = 0$ where the DC–SQUID is located. It is observed the largest in fact, at $x_q/x_l = 0.1$ and in the case of $f_s = 0.48$. This could be expected from our discussion in the last section, where we showed that near x_0 the voltage profile of the modes showed the greatest variation, in particular when the flux was near $f_s = 0.5$. Elsewhere along the stripline cavity, we observe oscillating areas of high (low) values of I_{CP} as x_q/x_l changes. We can predict that these correspond to regions where the variation of the mode profiles with respect to the DC–SQUID flux is largest (smallest) for a substantial number of the contributing modes.

Another observation we should make, is that I_{CP} is always anti–symmetric around the flux $f_s = 0$. This will be a recurring result throughout the rest of this chapter, and can be attributed to the fact that the flux dependence in our system is mathematically included through the expression for the effective plasma frequency of the DC–SQUID ω_s, which is a function of the cosine of f_s. Hence the energy shift is always symmetric around f_s, while its derivative, the current, anti–symmetric, as observed here.

3.8.2 Paramagnetic Vs Diamagnetic Contributions

We have already discussed in Sections 3.2 and 3.6 that the total value of I_{CP} consist of two main contributions — one coming from the paramagnetic qubit–cavity

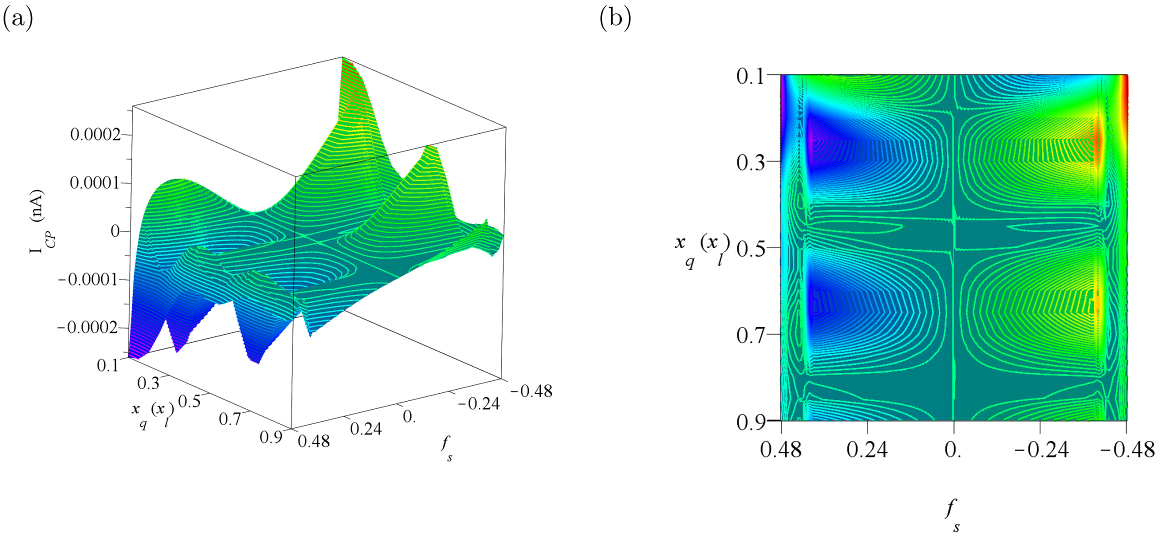

Figure 3.5: The Casimir–Polder current I_{CP} as a function of the DC–SQUID flux f_s as well as the ratio x_q/x_l. Both plots (a) and (b) show the same data, but in different formats. We can observe a general trend, that shows the magnitude of I_{CP} increasing as the qubit's position gets closer to the boundary containing the flux dependent DC–SQUID.

coupling, and the other, from the diamagnetic, field self–energy interaction. In this section, we again look at the case of a varying ratio of x_q/x_l, but now consider the two contributions $I_{\mathrm{CP}}^{\mathrm{diam}}$ and $I_{\mathrm{CP}}^{\mathrm{para}}$ that make up the total Casimir–Polder current. The results are shown in Fig. 3.6. Plots shown in (a-b) depict $I_{\mathrm{CP}}^{\mathrm{diam}}$, while in (c-d), $I_{\mathrm{CP}}^{\mathrm{para}}$. If we were to add both of these contributions together, we would reproduce the plots shown in Fig. 3.5 from the previous section.

It is clear that for the set of parameters used here, the two contributions are similar in magnitude. This in general does not have to be the case. For example looking at the general expression for the energy shift δE_0 shown Eq. 3.56 and at the expression 3.45, we can conclude that one key set of parameters that has an impact on the contributions of these two terms, consists of the capacitors that define the qubit's charging energy and the coupling energy between the qubit and the stripline cavity. Both of these could in principle be varied at the fabrication time of the circuit.

We also observe that the both $I_{\mathrm{CP}}^{\mathrm{diam}}$ and $I_{\mathrm{CP}}^{\mathrm{para}}$ have a complicated dependence on the qubit position as well as the flux through the DC–SQUID. At least in the set of parameters we have looked at here explicitly, Fig. 3.6 shows that they are often similar in magnitude but correspond to currents in different directions. This is not beneficial to maximising the total Casimir–Polder current, since the two contributions are often seen to cancel each other out.

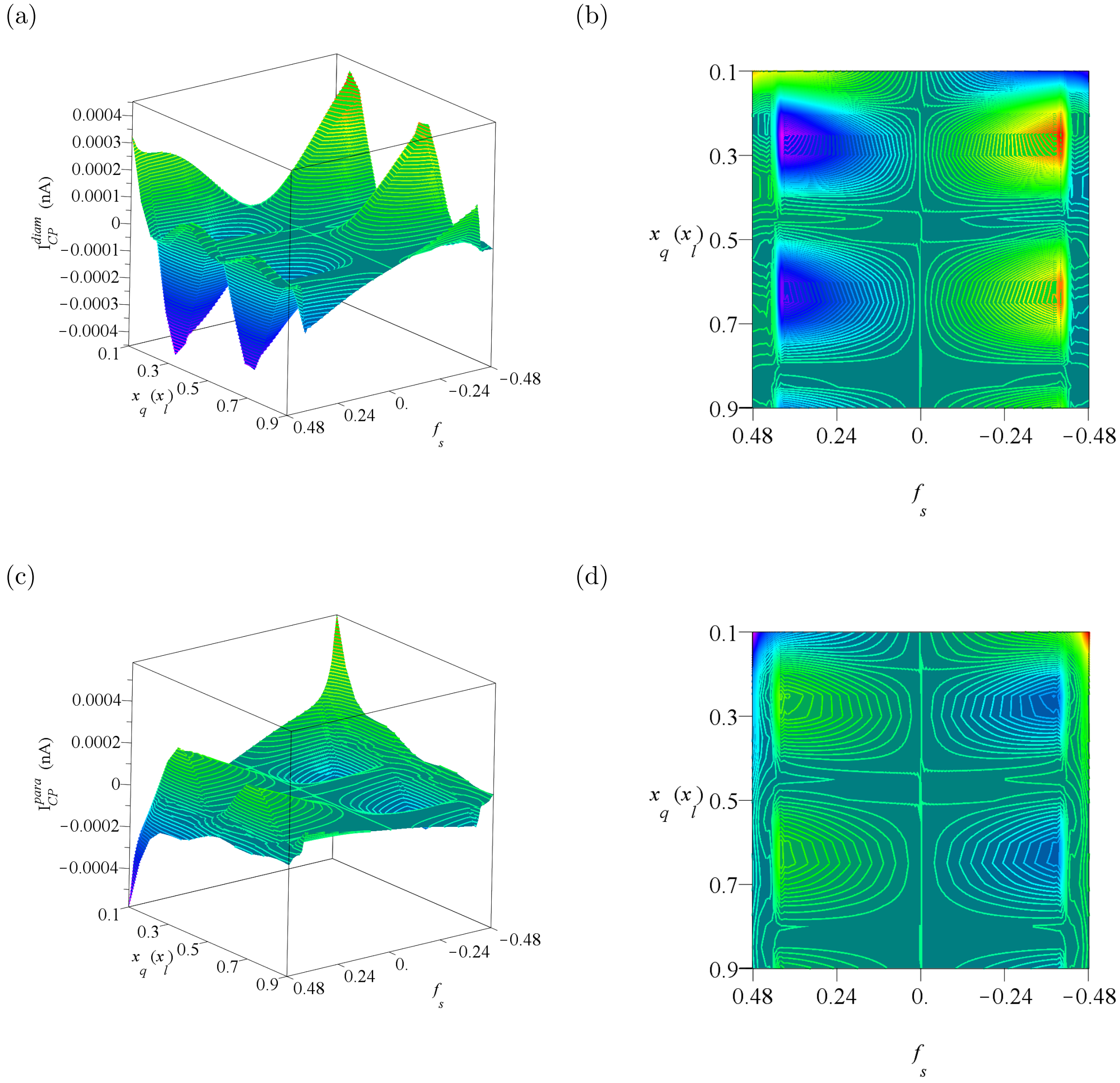

Figure 3.6: The Casimir–Polder current contributions $I_{\text{CP}}^{\text{diam}}$, shown in plots (a-b) and $I_{\text{CP}}^{\text{para}}$, shown in plots (c-d). The total Casimir–Polder current composes of the sum of $I_{\text{CP}}^{\text{diam}}$ and $I_{\text{CP}}^{\text{para}}$ and is shown in Fig. 3.5.

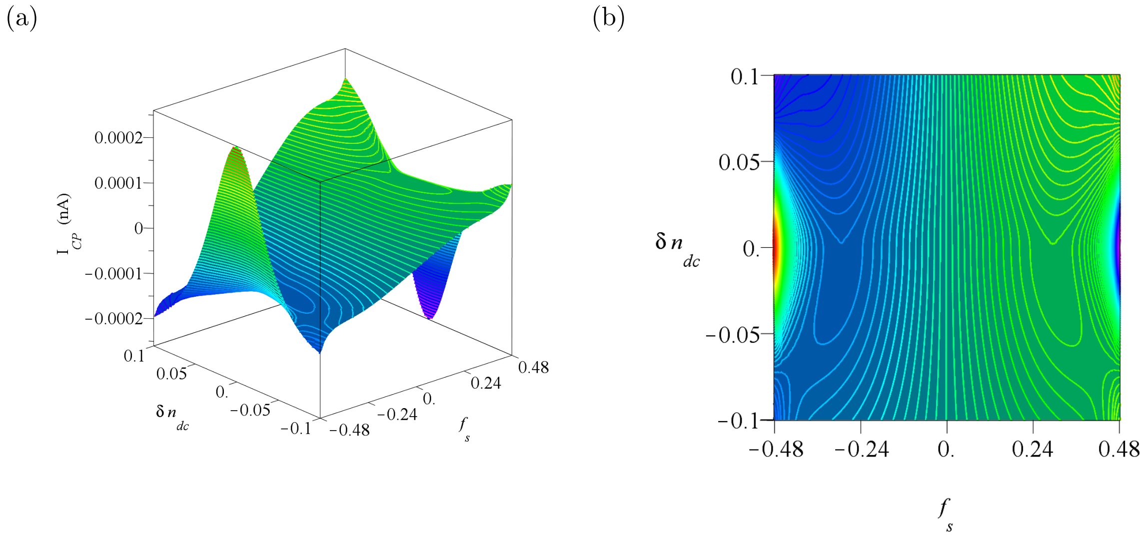

Figure 3.7: The Casimir–Polder current I_{CP} as a function of the DC–SQUID flux f_s as well as the qubit charge offset δn_{dc}. Both plots (a) and (b) show the same data, but in different formats. A nonzero charge offset introduces an effective permanent dipole moment, which in turn leads to a lack of symmetry around $\delta n_{\mathrm{dc}} = 0$ — see main text for more details.

3.8.3 Varying offset charge δn_{dc}

In this section we will look at the effect of varying the qubit charge offset δn_{dc}. We have already discussed that changing δn_{dc}, controls the effective coupling of the qubit to the stripline cavity. In particular, from Eq. 3.44 and the fact that $\tan\theta_q = -E_{Jq}/(8E_c\delta n_{\mathrm{dc}})$, we can deduce that at $\delta n_{\mathrm{dc}} = 0$ only coupling to the qubit via the σ_x term is relevant, while with $\delta n_{\mathrm{dc}} \neq 0$, coupling of the field to the σ_z qubit operator also contributes to the total energy shift. Furthermore, a nonzero δn_{dc} introduces, what can be interpreted as, a permanent dipole moment of the qubit through the second term of Eq. 3.56, which in turn, leads to non–symmetry around $\delta n_{\mathrm{dc}} = 0$ in the calculated energy shift, and therefore the resulting Casimir–Polder current. This can be seen directly from Fig. 3.7. As before, both plots (a) and (b) show the same data, but presented differently. We use the same set of parameters as in the previous sections, except fix the qubit at $x_q = 0.001\,\mathrm{m}$ from the left boundary where the DC–SQUID is located, which corresponds to the ratio $x_q/x_l = 0.1$. The δn_{dc} is varied between values of -0.1 and 0.1, and the largest magnitude of I_{CP} is observed at $\delta\mathrm{dc} = 0$ and at $f_s = 0.48$, the highest value of the DC–SQUID flux considered.

3.8.4 Finite Temperature

So far, in all the results we have presented, we have assumed that our system is at zero temperature. In this section, we will look at a more realistic scenario, by relaxing this condition and considering a small, but finite temperature. We should stress, however, that as was already outlined in Sec. 3.6, we will concentrate on a regime of parameters where $k_B T \ll \hbar\omega_q$, and neglect any effects due to the thermal occupation of the qubit's Hilbert space beyond the ground state. We will, however, allow for the degrees of freedom of the stripline cavity to be thermally excited (which would lead to $\langle n_k \rangle$ greater than zero in Eq. 3.56). In the previous sections, we have also assumed that the length of the cavity is $x_l = 0.01\,\mathrm{m}$. This corresponds to the frequency of the lowest mode $n = 0$, of $\sim 3.3\,\mathrm{GHz}$ — very much of the order of the qubit's frequency, which at $\delta n_{\mathrm{dc}} = 0$ is assumed to be $7\,\mathrm{GHz}$. In this section, we will assume an increased cavity length of $x_l = 0.1\,\mathrm{m}$, with the frequency of the lowest mode of $\sim 0.33\,\mathrm{GHz}$, with the qubit still close to the DC–SQUID boundary, at $x_q = 0.001\,\mathrm{m}$. Although the effect will be still small, this change will allow for it to be greater than would have been before, as the mean mode occupation numbers $\langle n_k \rangle$ will be larger. This very point can be observed directly from Fig. 3.8(a), where we plot the mean thermal occupation of a cavity mode as a function of frequency and temperature. So for example at a realistic experimental temperature of $T = 0.040\,\mathrm{K}$ we can expect the lowest energy mode to have on average around two photons (i.e $n_0 \sim 2$), with this number decreasing for higher indexed modes. Hence repeating the calculation of I_{CP} leads to results shown in Figures 3.8(b) and 3.8(c). Both plots show the same data, with the plot in (c) being a zoomed–in version of the plot shown in (b). We look at two cases of zero temperature (solid curves) and of $T = 0.040\,\mathrm{K}$ (dashed curves). Different colors correspond to different qubit charge offset — in particular we have $\delta n_{\mathrm{dc}} = 0.0$ (in red), $\delta n_{\mathrm{dc}} = -0.08$ (in blue), and $\delta n_{\mathrm{dc}} = 0.08$ (in green). It is clear from these plots that the difference in results between the two different temperatures is minor (at worst less than 10%), but is observable at high values of the DC–SQUID flux, near $f_s = 0.5$, and at the charge offset of $\delta n_{\mathrm{dc}} = 0$.

3.8.5 Can the value of I_{CP} be larger?

It is clear from the last few sections, and from looking at Eqs. 3.56 and 3.64 that this is a highly parameter–dependent system. In particular, since we do not have an analytical expression for the energy shift δE_0 (i.e., a closed form for the sum) and therefore the Casimir–Polder current, ensuring that we have the largest value of I_{CP} possible, for a set of physically realizable parameters, would require an involved numerical optimization over the full parameter space. We have clearly not done that, but instead discussed what happens when we vary certain selected parameters, while keeping others constant. It is very likely that such an optimization could

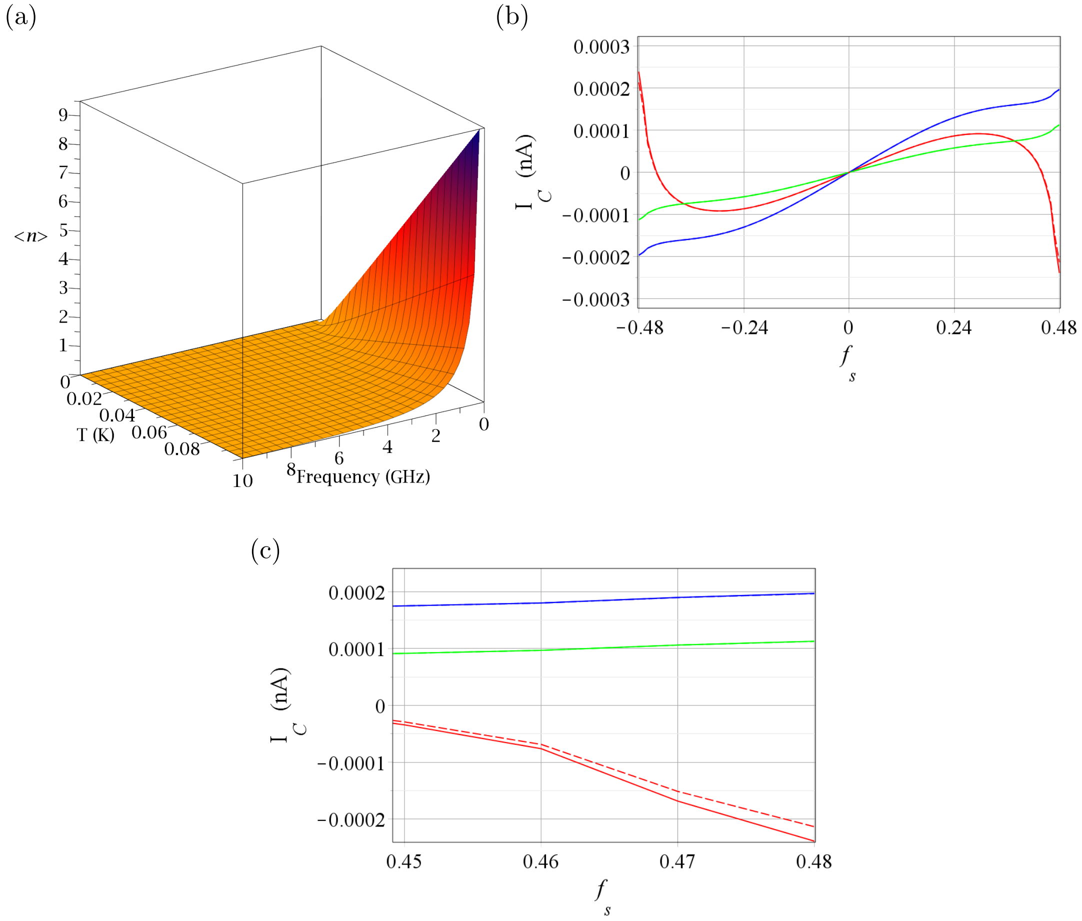

Figure 3.8: (a) Thermal occupation of a field mode, plotted as a function of frequency and temperature. Plots in (b) and (c) show the Casimir–Polder current in a circuit with $x_l = 0.1\,\mathrm{m}$ and with the qubit placed at $x_q = 0.001\,\mathrm{m}$, as a function of the qubit charge offset of $\delta n_{\mathrm{dc}} = 0.0$ (in red), $\delta n_{\mathrm{dc}} = -0.08$ (in blue), and $\delta n_{\mathrm{dc}} = 0.08$ (in green). Solid curves represent results at the temperature $T = 0$, while dashed curves at $T = 0.040\,\mathrm{K}$. The difference in results between the two different temperatures is very minor, and is only observable at high values of the DC–SQUID flux, near $f_s = 0.5$, and at the charge offset of $\delta n_{\mathrm{dc}} = 0$. The plot shown in (c) is a zoomed–in version of the plot shown in (b). The lack of symmetry between curves corresponding to $\delta n_{\mathrm{dc}} = -0.08$ and $\delta n_{\mathrm{dc}} = 0.08$ is discussed in main text.

increase the Casimir–Polder effect we studied, perhaps even significantly.

One could also envision some changes to the physical system that could be beneficial. For example it is likely that a more elaborate flux dependence of the boundary conditions could be helpful. In particular one could imagine having a DC–SQUID on both sides of the stripline cavity. This would allow for a larger effective phase shift seen by different modes, which under right circumstances could likely be engineered to increase the total flux dependence of the energy shift, and hence the Casimir–Polder effect. The drawback would be that the normal mode structure would become even more complicated. Following the discussion in Sec. 3.4, even in the same limits of a small size of the DC–SQUIDs, we would expect another equation that would have to be solved simultaneously along with Eqs. A.2 and A.3 in order to describe the normal modes $u_n(x)$ and their frequencies ω_n.

Yet another approach could involve coupling the stripline cavity that the qubit interacts with, to another cavity constructed out of left handed material (one where the placement of the capacitors and inductors is inverted in a schematic of Fig. 3.2(a)). It was shown in [36], that in such a system, the mode structure is very different from what we discussed in this chapter. In particular, the mode frequency is inversely proportional to the wave number, namely $\omega_n \sim 1/k_n$. This results in a mode profile $u_n(x)$ along the cavity that the qubit couples to, to be very similar for a large range of modes. Strategically placing a qubit at a point corresponding to a voltage node for all these modes, would likely lead to an increased value of the energy shift, and in some cases possibly I_{CP}.

In summary, it is very likely that by both optimizing over the values of physical parameters, and perhaps introducing some changes to the general circuit used, would lead to an enhanced Casimir–Polder effect — perhaps making it large enough that it could be more easily measurable.

3.9 Cavity Boundary Dependent Lamb Shift

While so far we have considered our superconducting circuit for the purpose of studying the Casimir–Polder–like current, we now also have all the necessary ingredients to look at it in the context of a flux–controllable Lamb shift. Similarly to the general Casimir–Polder effect, the Lamb shift is related to the changes in atom's energy level structure, due to its interactions with the electromagnetic field (vacuum typically). It was first theoretically explained by Bethe [5] and experimentally observed by Lamb and Retherford in 1947 [77]. In their setup, they used spectroscopic methods to measure the difference in ${}^2S_{\frac{1}{2}}$ and ${}^2P_{\frac{1}{2}}$ energy levels of the Hydrogen atom, and found that they are not degenerate, as one would expect from Dirac's 1928 theory. This result was of great significance and was, partly at least, responsible for a burst of activity in what would become the field of quantum electrodynamics.

Since then, many more experimental realizations in the atomic domain have been studied [15, 59, 82]. Furthermore, in 2008 an example of a Lamb shift was also demonstrated in a superconducting circuit[10] [43]. The authors considered a transmon qubit embedded in a stripline cavity very similar to the one described in Sec. 3.3. In our discussion, we will use the results already obtained in the rest of this chapter to present an expression of a Lamb shift that explicitly depends on the property of a tunable boundary — namely the DC–SQUID flux.

We initially concentrate on a case of a qudit, and later the special case of a qubit. Using the expression for the energy shift of the state shown in Eq. 3.50 that we have already calculated, we can write the total energy difference between the qudit being in its 1st excited state and the ground state. Using Eq. 3.55, we arrive at

$$\begin{aligned}\Delta E_{1,0} =&(\hbar\varepsilon_1 + \delta E_1) - (\hbar\varepsilon_0 + \delta E_0)\\ =&\hbar\left(\varepsilon_1 - \varepsilon_0\right) + \hbar\sum_k x_{1,2}^2 g_k^{(\pm)2}\left(\frac{\langle n_k\rangle + 1}{(\varepsilon_1 - \varepsilon_2) - \omega_k} + \frac{\langle n_k\rangle}{(\varepsilon_1 - \varepsilon_2) + \omega_k}\right)\\ &- \hbar\sum_k x_{1,0}^2 g_k^{(\pm)2}\left(\frac{\langle n_k\rangle + 1}{(\varepsilon_1 - \varepsilon_0) - \omega_k} + \frac{\langle n_k\rangle}{(\varepsilon_1 - \varepsilon_0) + \omega_k}\right)\\ &- \hbar z_1^2\sum_k \frac{g_k^{(\pm)2}}{\omega_k} + \hbar z_0^2\sum_k \frac{g_k^{(\pm)2}}{\omega_k}.\end{aligned} \tag{3.66}$$

The first term clearly corresponds to the qudit's "bare" energy difference between 1st excited and ground states, while the subsequent terms represent the very Lamb shift we setup to calculate. From now on let us call it δE_{Lamb}. It is easy to see that the third level of the qubit can be important as the expression above includes terms that depend on both ε_2 and $x_{1,2}$. We could follow the methods discussed in Sec. 3.5 to rewrite these variables in terms of physical circuit parameters, but instead here for the sake of simplicity, we will treat the qudit as a two level system — a qubit. Hence, with the help of Eq. 3.44 we can simplify Eq. 3.66 to

$$\delta E_{\text{Lamb}} =\hbar\sum_k g_k^{(\pm)2}\left(x_{0,1}^2(2\langle n_k\rangle + 1)\left(\frac{1}{\omega_q + \omega_k} + \frac{1}{\omega_q - \omega_k}\right) + \frac{z_0^2 - z_1^2}{\omega_k}\right). \tag{3.67}$$

We can expect that the frequency cutoff mechanisms introduced in Sec. 3.7 to still apply, and assume that $g_k^{(\pm)}$ can be replaced by $g_k^{(\pm)}P(\omega_k)$. Futhermore, as was the case with the energy shift of the qudit's ground state, it is clear that δE_{Lamb} is not defined when $\omega_k = \omega_q$. Here however, this is true regardless of the temperature of our system — this condition is true even when $T = \langle n_k\rangle = 0$. Hence in order for the

---

[10] We should stress that in [43], the authors considered a superconducting qubit interacting with a single field mode. In more standard descriptions of the Lamb shift however, one typically considers an atom interacting with a multi–mode field, as is done here.

perturbative Lamb shift above to be defined (as calculated using non–degenerate perturbation theory as above), we need for $g_k^{(\pm)2}/|\omega_q - \omega_k| \ll \omega_q + \omega_k$ to be satisfied.

Finally, in order to further rewrite this Eq. 3.67 above, for the particular case of the superconducting system considered in this chapter we note that (in the case of the charge qubit for example) we can rewrite $x_{0,1} = -\sin\theta_q$ and $z_1^2 - z_0^2 = 8\delta n_{\text{dc}} \cos\theta_q$. We can also point out perhaps the most important observation of this discussion. Since we have already shown that $g_{n}(\pm)$ depends on the DC–SQUID flux, which can be easily varied in a real experimental system, we have an elegant means to control the effective size of δE_{Lamb}.

3.10 Standard Casimir Effect

Besides the small digression of the last section, where we discussed a flux–dependent Lamb shift, throughout most of this chapter, we have mainly concentrated on the existence of the Casimir–Polder effect in a superconducting circuit. We showed that under some circumstances, the presence of the qubit can induce a current in the DC–SQUID located on the cavity boundary. In this section, we will consider an effect analogous to the Casimir (not Casimir–Polder) effect already reviewed in Sec. 3.1, where the system consisted of two large, parallel conducting plates, some distance apart, and where the mere presence of the field vacuum fluctuations can induce a force between the plates. The superconducting circuit that will model the analogue of such an effect, will consist of the same stripline cavity as in the previous sections, but this time, we will discard the qubit completely. The cavity boundaries, DC–SQUID at $x = 0$ and open circuit at $x = x_l$, will correspond to the conducting plates that enforce the field boundary conditions in a traditional system.

Before we look at the setting of our system in more detail, let us briefly review the mathematical nature of the Casimir force, and outline one way in which it can be calculated. In the case of two parallel plates, the general expression of the force on the mirrors can be written as $F_{\text{Casimir}} = -\partial_d U(d) = -\partial_d(E_0(d) - E_0(\infty))$ [85]. Here the $E_0(x) = \sum_n \frac{1}{2}\hbar\omega_n(x)$ represents the ground state energy of the field with the plates distance x apart, while $U(d)$ is the potential energy associated with placing the plates into a configuration where they are distance d away from one another. While clearly both $E_0(d)$ as well as $E_0(\infty)$ are infinite, their difference can be shown to be finite using the Euler–Maclaurin formula[11]. This leads to a well defined expression for the Casimir force.

Let us next look at the case of the superconducting circuit shown in Fig. 3.2(a). We concentrate on a case of zero temperature, and neglect the qubit, while only

---

[11] One typically also needs to enforce various frequency cutoff mechanisms, based on physical arguments. However it is important to stress that the final expression for F_{Casimir} is independent of these simplifications.

consider the stripline cavity. We assume that the cavity length x_l is a fixed parameter (in contrast to a case discussed above where the plates enforced the field boundary conditions, and hence the force was defined in terms of the distance between them), however we treat the flux through the DC–SQUID as the classical parameter that lets us define a generalized force (here a current). This, as in the case of the Casimir–Polder discussion in the rest of this chapter, will allow us to define a Casimir current, which we will denote as I_C.

In order to calculate I_C, we will follow the general procedure from above. First, let us note that the energy of the field's ground state, at a fixed value of the flux is

$$E_0(\Phi_s) = \sum_{n=0}^{\infty} \frac{1}{2}\hbar\omega_n(\Phi_s) \tag{3.68}$$

with Φ_s the flux through the DC–SQUID. Hence, we can define a quantity analogous to the potential energy from the standard Casimir effect, call it ΔE, as the difference between E_0 at different values of the flux. For convenience, let us chose one reference value of $\Phi_s = 0$, while the other, an arbitrary $\Phi_s = \Phi$, with $\Phi \neq 0$. Then we can write

$$\begin{aligned}\Delta E(\Phi) &= E_0(\Phi) - E_0(0) \\ &= \frac{1}{2}\hbar\sum_{n=0}^{\infty}\Delta\omega_n,\end{aligned} \tag{3.69}$$

with $\Delta\omega_n = \omega_n(\Phi) - \omega_n(0)$. This lets us define a Casimir current as simply

$$I_C = -\frac{\partial \Delta E}{\partial \Phi}. \tag{3.70}$$

For this expression to be valid, we need to ensure that ΔE is finite. We will look at this expression numerically shortly, but first, let us outline a brief sketch of an analytical proof of convergence. While it would be reasonable to include a frequency cutoff as in Sec. 3.7, based on physical considerations, it seems that this step here is not necessary.

Since we have already calculated the normal modes of the field inside the stripline cavity, let us start by reviewing the results from 3.4. The relationship between ω_n and the phase shift that each modes sees, θ_n, can be written as

$$\theta_n = \tan^{-1}\left(\frac{\omega_n^2 - \omega_s(\Phi_s)^2}{\omega_c\omega_n}\right) \tag{3.71}$$

$$\omega_n = \omega_v\left(n\pi - \theta_n\right), \tag{3.72}$$

where for the sake of notational brevity, we have defined $\omega_c = (C_{Js}Z_0)^{-1}$ and $\omega_v = v/x_l$. For a given n, these equations can be solved numerically, but in order to show the convergence of Eq. 3.69, we only need to concentrate on their behavior in a case of large n. First, using Eqs. 3.71 and 3.72, we can rewrite $\Delta\omega_n$ as

$$\begin{aligned}\Delta\omega_n &= \arctan\left(\frac{(\omega_s(0)^2 - \omega_s(\Phi)^2)\omega_c\omega_n}{\omega_n^4 + \left(\omega_c^2 - \omega_s(\Phi)^2 - \omega_s(0)^2\right)\omega_n^2 + \omega_s(\Phi)^2\omega_s(0)^2}\right)\\ &= \arctan\left(\frac{p_1(\omega_n)}{p_4(\omega_n)}\right),\end{aligned} \tag{3.73}$$

where we have taken $p_k(\omega_n)$ as the corresponding polynomials of degree k in ω_n. Our next step is to see how ω_n scales as n increases.

To do this, we first note that in a given physical system, ω_v, ω_c and ω_s are finite. We can therefore always find a value of n large enough, so that $\omega_n \gg \omega_v, \omega_c, \omega_s$. This lets us expand Eq. 3.71 in the limit of large ω_n. Keeping the first few terms, leads to

$$\theta_n = \frac{\pi}{2} - \frac{\omega_c}{\omega_n} + \frac{\omega_c^3}{3\omega_n^3} - \frac{\omega_s^2\omega_c}{\omega_n^3} + \mathcal{O}\left(\frac{1}{\omega_n^5}\right). \tag{3.74}$$

Next, solving Eq. 3.72 for θ_n and equating it with the expansion above, we arrive at

$$n\pi - \frac{\omega_n}{\omega_v} = \frac{\pi}{2} - \frac{\omega_c}{\omega_n} + \frac{\omega_c^3}{3\omega_n^3} - \frac{\omega_s^2\omega_c}{\omega_n^3} + \mathcal{O}\left(\frac{1}{\omega_n^5}\right). \tag{3.75}$$

This lets us rewrite ω_n as

$$\omega_n = \pi\left(n - \frac{1}{2}\right)\omega_v + \delta\omega_n. \tag{3.76}$$

$\delta\omega_n$ can only be solved for numerically, but we are only interested in its trend as $n \to \infty$. In particular, as n increases, $\delta\omega_n$ decreases, in the worst case, as[12] $\mathcal{O}(1/n)$. Next, we note that[13] at large ω_n, $\frac{p_4(\omega_n)}{p_1(\omega_n)} \in \Theta(\omega_n^3)$. Hence, using the newly found expression for ω_n in terms of n, we can conclude that $\frac{p_4(\omega_n)}{p_1(\omega_n)} \in \Omega(n^3)$, and hence for a large enough n we find

$$\frac{p_4(\omega_n)}{p_1(\omega_n)} > n^2. \tag{3.77}$$

---

[12] We are neglecting the fact that we have defined ω_n in terms of n as an infinite sum. A more rigorous proof would have to take this into account.

[13] Here we stress that Θ represents the *Big Theta* notation.

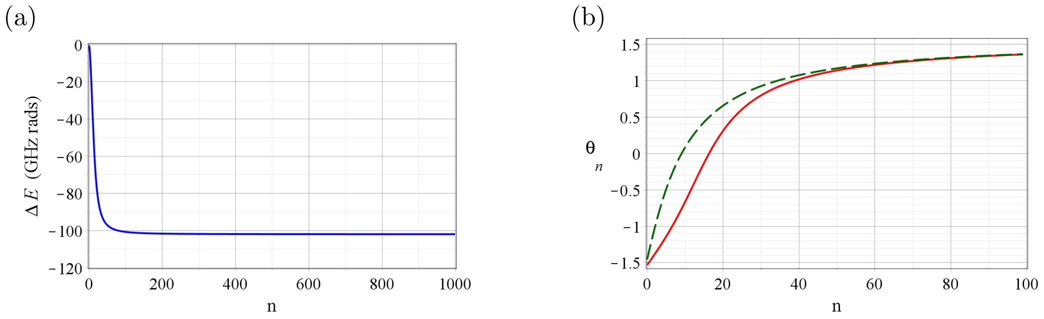

Figure 3.9: (a) ΔE as a function of mode number n for a fixed value of flux ratio $f_s = 0.40$ calculated numerically. Past $n \approx 200$ the value for ΔE stops changing, even as contributions from higher frequency modes keep being added. This is consistent with the expectation that ΔE is convergent. (b) The change of θ_n parameter, which corresponds to the phase shift seen by the nth mode, as a function of mode number n, shown for two values of DC–SQUID flux ratio f_s. The red, solid curve corresponds to $f_s = 0$, while the green, dashed curve, to $f_s = 0.40$. As n increases, in both cases θ_n tends to $\frac{\pi}{2}$, which physically corresponds to the fact that in the limit of high n (and hence high ω_n) all the modes see the boundary at $x = 0$ in the same way.

Therefore, since $\arctan(x)$ is a monotonically increasing function[14]

$$\arctan\left(\frac{p_1(\omega_n)}{p_4(\omega_n)}\right) < \arctan\left(\frac{1}{n^2}\right), \tag{3.78}$$

for $n \geq n_L$, with n_L appropriately chosen. This finally lets write $\Delta\omega_n$ as

$$\begin{aligned} \Delta\omega_n &= \sum_{n=0}^{\infty} \arctan\left(\frac{p_1(\omega_n)}{p_4(\omega_n)}\right) && (3.79)\\ &< \sum_{n=0}^{n_L-1} \arctan\left(\frac{p_1(\omega_n)}{p_4(\omega_n)}\right) + \sum_{n=n_L}^{\infty} \arctan\left(\frac{1}{n^2}\right). && (3.80) \end{aligned}$$

The first sum is clearly finite, as we are only summing over n_L elements, and the second term can now be also shown to be convergent (by for example an integral test). This lets us conclude that the series presented in Eq. 3.69 converges, and hence ΔE is finite.

We are now ready to look at a specific example of ΔE and I_C, in a system with

---

[14] We have assumed that $p_1(\omega_n)/p_4(\omega_n) > 0$, for large enough n, and therefore ω_n, without any loss of generality. This ratio could be negative (depending on which of $\omega_s(\Phi)$ or $\omega_s(0)$ is greater), and since arctan is an antisymmetric function, the minus sign could be simply taken outside of the sum in Eq. 3.69.

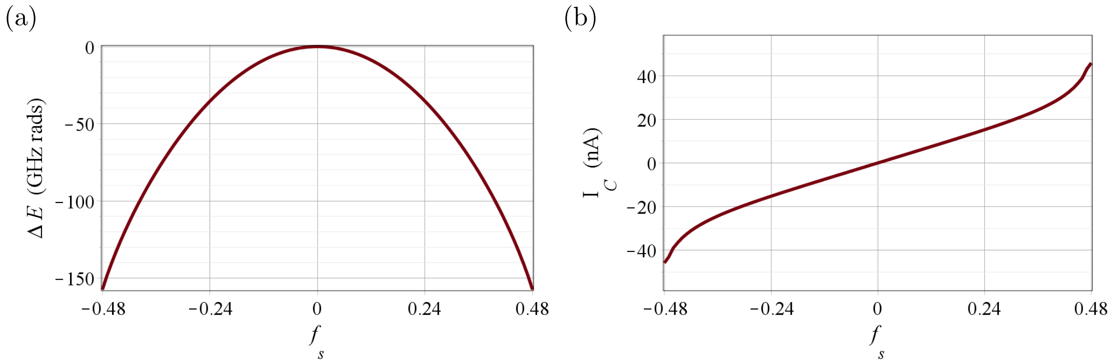

Figure 3.10: (a) ΔE plotted as a function of the DC–SQUID flux ratio f_s. ΔE is calculated numerically by executing the sum shown in Fig. 3.69 over a finite number of modes — enough to conclude convergence. (b) The Casimir current I_C plotted as a function of DC–SQUID flux ratio f_s (shown in the units of nA). I_C is obtained by numerically differentiating results for ΔE from part (a). As expected, ΔE is symmetric, while I_C is antisymmetric in f_s — see main text for more details.

realistic physical parameters. In particular, we will consider the same numerical values of various parameters as in the case of the Casimir–Polder discussion, in the previous sections of this chapter. We will assume that $x_l = 0.01\,\text{m}$, $l = 4.53 \times 10^{-7}\,\text{H/m}$ and $c = 1.27 \times 10^{-10}\,\text{F/m}$. As before, these lead to $v = 1/\sqrt{cl} = 1.32 \times 10^{8}\,\text{m/s}$ and $Z_0 = \sqrt{l/c} = 59.72\,\Omega$. Furthermore, we will fix the plasma frequency of the DC–SQUID at $f_s = 0$ as 107 GHz — a realistic value for a DC–SQUID in a circuit such as the one presented here.

These parameters let us numerically calculate ΔE from Eq. 3.69 by summing over the various contributions of the different modes. While we will only sum over a finite set of modes, it is important to stress that we need to consider all the modes that are required for the series to converge. Fig. 3.9(a) shows how for a fixed value of $f_s = 0.4$, ΔE scales as the mode number n increases. It is clear that in this case, past $n \approx 200$ the value for ΔE stops varying, even as contributions from higher frequency modes keep being added. In Fig. 3.9(b), we also look at how the θ_n parameter, which corresponds to the phase shift seen by the nth mode, as a function of mode number n, changes as the mode number n increases, here for two different values of DC–SQUID flux ratio f_s. The red, solid curve corresponds to $f_s = 0$, while the green, dashed curve, to $f_s = 0.40$. At low values of n, the various modes see a different relative phase shift, which depends on the DC–SQUID flux. As n increases, however, in both cases θ_n tends to $\frac{\pi}{2}$, which physically corresponds to the fact that in the limit of high n (and hence high ω_n) all the modes see the boundary at $x = 0$ in the same way.

We are now ready to see how both ΔE as well as I_C vary as a function of the DC–SQUID flux ratio f_s, with I_C calculated by numerically differentiating ΔE

with respect to Φ. Fig. 3.10(a), shows results for ΔE, while Fig. 3.10(b) for the Casimir current I_C. As we might expect, the results for ΔE are symmetric around f_s, while the Casimir current is antisymmetric. This is consistent with the results we observed in a Casimir–Polder case, in the previous sections, and is a direct consequence of the fact that the DC–SQUID flux dependence in our system is included through the DC–SQUID plasma frequency, which in turn mathematically scales through a symmetric cosine function. For the set of physical parameters that we study here, the maximum of I_C is observed close to f_s, and reaches almost $\sim 50\,\mathrm{nA}$. This number, while small, might be at the verge of being detectable.

3.11 Casimir and Casimir–Polder Current Measurement Prospects

So far, we have shown how to derive both Casimir as well as Casimir–Polder–like effects in a superconducting circuit system. A particularly important topic to address, is whether the currents associated with these effects, can be actually detected, and if so, how? In this section, we will briefly speculate on possible answers to these questions.

Over a set of realistic, experimentally viable parameters, without optimization, and subject to the cutoff mechanisms discussed in Sec. 3.7, we have shown that in our system, the magnitudes of the currents associated with the Casimir and Casimir–Polder–like effects, were of the orders $10^{-8}\,\mathrm{A}$ and $10^{-13}\,\mathrm{A}$ respectively. In both cases, these numbers correspond to the currents circulating around the DC–SQUID loop located on the boundary of the stripline cavity. These currents are small, but with modern technology, should be detectable. We stress however, that the Casimir–Polder current calculated here, is by definition, only due to the presence of the qubit. In a system we have considered, one has to expect that the total effective current that would be of importance in an experimental setting, would necessarily consist of both the Casimir as well as the substantially weaker Casimir–Polder currents simultaneously. Hence a good start as far as the experimental realization is considered, would be to look at the case of a Casimir effect in our circuit, and simply initially neglect the presence of the qubit altogether.

One way in which circulating currents can be measured, consists of inductively coupling a SQUID amplifier [87, 89] to the loop around which the current circulates. The natural frequency of the DC–SQUID that makes up the amplifier, depends on the total flux through its loop, which in turn depends on the strength of the circulating current being measured. A variety of flux discrimination approaches that use this fact will be briefly described in Sec. 4.10, mostly in the context of flux qubit measurement, but the principle behavior is similar here. The magnitudes of currents that we expect to be detectable, could be as small as $10^{-14}\,\mathrm{A}$, assuming long enough integration times and strong enough mutual inductance between the amplifier loop and the boundary DC–SQUID in our circuit [50].

Although a DC measurement (where the flux through the boundary DC–SQUID is kept constant) is likely possible, it might be beneficial to also consider slow AC measurements instead, as they are less susceptible to low frequency noise. This would lead to a scheme analogous to the standard Casimir forces detection mechanism shown in [13], where the force was experimentally measured to within 15% of the known theoretical value. The measurement procedure consisted of slowly driving the two plates, and showing that the effective frequency of their resulting motion has a correction that is in agreement with a presence of a "drag–like" force, which in turn scales as a function of separation between the plates exactly as Casimir predicted in his 1948 paper.

An analogous version of this experiment in our setting, would be to slowly modulate the flux through the DC–SQUID, for example around some constant value where we predicted the magnitudes of the Casimir or Casimir–Polder currents to be highest. The Casimir–like effects in our circuit, would introduce a correction to the circulating current expected purely from the effects of the drive, and hence a small shift to the effective frequency of its modulation. Of course various issues would have to be worked out, such as the effects of the interaction with the measuring DC–SQUID amplifier, the fact that in in our system we have neglected the effects of the geometric inductance of the boundary DC–SQUID, which would have to be accounted for, since they have an effect on the total circulating currents around the DC–SQUID, and so on.

Yet another scheme of interest that would explore at least some of the physics presented in this chapter, would be simply to perform a "standard" spectroscopic qubit measurement as is often done in applications related to quantum information. In the case of the charge qubit that we studied for example, this could either mean a direct charge offset measurement by coupling a single Cooper pair transistor directly to the qubit, or to use more modern techniques which consist of driving the cavity with a probe field, and observing its qubit–state–dependent properties (phase, magnitude). This kind of a measurement would help us confirm predictions related to the Lamb shift that was described in Sec. 3.9, where we were interested in the difference between various energy levels of our system (say excited and ground states of the qubit), but not necessarily the Casimir–Polder current we set out to measure. One easy way to see this, is to point out that by looking at differences between the energy levels we end up neglecting the diamagnetic coupling effects (the A^2–like term) that we have shown in Sec. 3.8.2 can be of fundamental importance to the total Casimir–Polder current. This is because the contributions of such a term are independent of the state of the qubit[15].

---

[15] This is not true when one calculates the higher order energy shift corrections, at which point the field self–interacting contributions would be dependent on the qubit state that is considered.

Hence to summarize, we believe a measurement of the effects calculated here is likely be possible, but more research is still required to work out its details and make it a reality.

3.12 Assumptions, Conditions and Model Limitations Review

In this second–last section of this chapter, we review the major assumptions that we have made throughout our discussion so far, and briefly touch on their various consequences.

1. **Series Convergence**
   In order to calculate the energy shift required to obtain the Casimir–Polder current numerically, the series expansion for δE_0 needs to be convergent. In Sec. 3.7 we discussed two physical mechanisms which ensure that to be the case, and defined a corresponding spectral response function $P(\omega)$ for each. The first was a result of the finite physical size of the qubit, while the second accounted for the fact that at frequencies beyond $2\Delta_{\mathrm{gap}}/\hbar$, the material that makes up the stripline cavity is in general no longer superconducting, which leads to damping of the high frequency modes. In a general case, the effective cutoff may be different depending on which mechanism dominates, but in our calculations, we have assumed that the qubit is small enough, and the latter scenario provides the leading cutoff contribution. Furthermore, we used $P(\omega)$, along with the length of the cavity, to establish over how many modes we actually have to sum in order to account for all of the non–negligible contributions. From Eq. 3.27 we see that $\omega_n \sim \frac{v}{x_l}$, hence it is clear that as x_l increases, the lowest frequency of the cavity will decrease, and therefore more modes will need to be accounted for. Finally, it is critical to reiterate here that the results shown in the Sec. 3.8 depend on just how we treat the frequency cutoff. Changing the form of $P(\omega_n)$, changes the Casimir–Polder currents that one would observe. Since a full understanding of the exact form of $P(\omega_n)$ that one would expect in our system is still an open problem, an actual Casimir–Polder experiment in a superconducting system such as the one discussed here, could be helpful in providing some insight.

2. **Perturbation theory validity**
   As shown in Sec. 3.6, we used non–degenerate perturbation theory to calculate the energy shift δE_0. In order for the expression to be useful, we need to ensure that it is valid over the range of parameters of interest. In particular, we

---

This, however, does not change the fact that the leading order term that is relevant in a Casimir–Polder effect, does not play a role when looking at qubit's energy differences.

want to be certain that the kth term of the sum that makes up δE_0 is smaller than $\omega_k + \omega_q$. Looking at Eq. 3.56, at zero temperature (when $\langle n_k \rangle = 0$), this condition is easily satisfied for reasonable physical parameters — in particular, if we note that all the terms scale inversely with ω_n, hence as k increases, the contributions of higher frequency modes decrease. However in the case of finite temperature, when $\langle n_k \rangle > 0$, the second term of Eq. 3.56 is divergent when the qubit is on resonance with a mode of the cavity field. Hence in order for the sum to be valid we need to satisfy the following condition

$$\frac{\langle n_k \rangle g_k^{(\pm)2} \sin^2\theta_q}{|\omega_q - \omega_k|} \ll \omega_k + \omega_q. \tag{3.81}$$

This condition implies that if the temperature is large, the energy of the lowest cavity mode cannot be "too small", and puts a limitation on how long our cavity should be. In the discussion above, therefore, we concentrate our discussion on cases of ether zero or very low temperatures.

3. **Linearity of a DC–SQUID**
In the derivation of the normal modes inside the stripline cavity, we treated the, in general nonlinear DC–SQUID, as a linear LC circuit. Let us briefly review the effects of this approximation. Using the notation from Sec. 3.4 where we defined the flux field along the cavity as $\Phi(x,t)$, we can define the flux across the DC–SQUID as $\Phi(0,t)$, or just Φ, for notational convenience. In the limit of small geometric inductance, we can write the full potential energy of the DC–SQUID as

$$U = -E_{Js}(\Phi_s)\cos(\Phi/\phi_0), \tag{3.82}$$

where $E_{Js}(\Phi_s) = \phi_0^2/L_{Js}(\Phi_s)$. Since in our system, the DC–SQUID is not biased with any DC current, we can expand this expression around $\Phi_s = 0$, which leads to

$$U \sim \frac{1}{2}\frac{E_{Js}(\Phi_s)}{\phi_0^2}\Phi^2 + \mathcal{O}(\Phi^4). \tag{3.83}$$

In order for this to be a valid representation of the DC–SQUID potential energy in our system, we need the spread of the wavefunction to be small. Mathematically, we can express this as

$$\Delta\Phi = \sqrt{\langle\Phi^2\rangle - \langle\Phi\rangle^2} \ll \phi_0. \tag{3.84}$$

This condition will clearly coincide with Φ's conjugate variable Q having a wide distribution. In a standalone DC–SQUID these conditions are satisfied as long as the Josephson energy $E_{Js}(\Phi_s)$ is much greater than the charging energy $E_{Cs} = e^2/2C_J$ [101], however, since here the DC–SQUID is an integral part of the more complicated system consisting of the stripline cavity, we have to be more careful. Using results shown in the Appendix C we can calculate an explicit expression for $\Delta\Phi$ assuming the full system is in its ground state. This leads to

$$\Delta\Phi = \sqrt{\sum_n \frac{\hbar}{2\omega_n} u_n^2(x=0)} \tag{3.85}$$

$$= \sqrt{\sum_n \frac{\hbar}{2\omega_n} \frac{\cos^2\theta_n}{\left(\frac{C_t}{2} + C_{Js}\cos^2\theta_n + \frac{1}{4Z_0\omega_n}\sin 2\theta_n\right)}}, \tag{3.86}$$

where we have used the explicit expression for the cavity normal modes calculated in Sec. 3.4. Substituting numerical values for various sets of parameters used throughout this chapter, leads to condition 3.84 being satisfied.

4. **Finite geometric inductance of a DC–SQUID**
Another implicit assumption that was made, was that the behavior of the DC–SQUID is dominated by the Josephson inductance $L_J(\Phi_s)$, and the effects of the geometric inductance L_g of the DC–SQUID loop has been neglected. This is usually a valid assumption as long as $L_J(\Phi_s) \gg L_g$, which can in practice be accomplished with appropriate choices of physical parameters. This assumption, along with the linearity of the DC–SQUID, is analogous to the claim that the "secondary" degree of freedom of the DC–SQUID (see Chapter 4 and Appendix D for a detailed discussion) can simply be approximated by Φ_s — the flux through the DC–SQUID. A finite geometric inductance L_g however, leads to a correction to this term, which in a realistic setting, where the DC–SQUID (and hence its geometric inductance) is not "small enough", might have to be considered.

3.13 Summary and Conclusions

In this chapter, we have studied Casimir and Casimir–Polder–like effects in a superconducting circuit system. We have done that by considering a stripline cavity with a boundary DC–SQUID, coupled to a superconducting qubit. For a set of realistic parameters, we found that the magnitudes of the currents associated with these effects, were of the orders $10^{-8}\,$A in the Casimir case, and $10^{-13}\,$A in the Casimir–Polder case. We have furthermore used the obtained results to describe a variable Lamb shift, that in principle could be controlled in situ by variations of the magnetic flux through a boundary DC–SQUID. Finally, we have briefly outlined prospects and difficulties related to the Casimir effect measurements in our system.

Chapter 4

Transient Dynamics of a Superconducting Nonlinear Oscillator

In this chapter, we study the finite temperature, transient dynamics of a circuit consisting of a DC–SQUID shunted with a large capacitance. The motivation behind this work, is an experiment performed by Britton Plourde's group at Syracuse University, where such a DC–SQUID was driven with short oscillatory pulses, and the resulting ringdown oscillations were observed. This was done for a variety of different applied flux values, as well as pulse amplitudes. Of particular interest, was the behavior of the system when subject to pulses with amplitudes that explored the nonlinear regions of the DC–SQUID's potential energy, as this is where the response can differ widely from a linear RLC circuit. Furthermore, since the experiment was performed at a temperature of ~ 0.300K, which corresponds to a thermal energy higher than the energy associated with the natural frequency of the oscillator, we also explore the important effects of thermal noise, and show that it can have a substantial impact on the response of the circuit, in particular when strong excitation pulses are applied. We end our discussion with a brief exploration of the applicability of the studied system to flux measurements.

4.1 DC–SQUID as a Nonlinear Oscillator

Nonlinear oscillations have been a subject of research for a very long time, as they can be found in a great variety of systems, both man–made and natural, ranging from simple swings or pendula, through motions of interstellar systems, to interacting atoms. Furthermore, within the past century, scientists and engineers have managed to explore nonlinearity for practical gain — good examples of this, are various amplifier designs in the study of electrical circuits. A subset of these are in fact built using DC–SQUIDs, which were introduced in Chapter 2. These systems include the Josephson bifurcation amplifiers (JBAs) [114, 122], microstrip superconducting quantum interference device amplifiers (MSAs) [62, 88], as well the Josephson parametric amplifiers [21, 58, 131]. Other useful applications of DC–SQUIDs, within the last couple of decades have been explored in the field of quantum information. There, DC–SQUIDs are used as building blocks for qubits [73], qubit couplers [42, 54, 104], and even as measuring devices [120] — more on this will be shown in Sec. 4.10. Once again the key feature that leads to their usefulness, largely results from the nonlinearity of the Josephson junctions, which DC–SQUIDs are built from.

In many applications presented above, the response of the DC–SQUIDs is often studied under one of two scenarios. The DC–SQUID oscillator is either driven with a continuous, sinusoidal drive, or biased with a simple DC current. In both of these cases, the behavior of the DC–SQUID is typically explored in its steady state. In the former scenario, at high enough drives, and when the drive frequency is near the oscillator's natural frequency, one can often observe a phenomenon known as bifurcation. It consists of having multiple solutions, with usually a large discrepancy in their amplitudes, that satisfy the system's nonlinear equations of motion. This very property of nonlinear oscillations is explored in some amplifier designs. A DC biasing current on the other hand, can be used to alter just how nonlinear a DC–SQUID's behavior is. In particular, biasing with a DC current of strength near the effective critical current of a DC–SQUID, and then applying a weak drive, will lead to a nonlinear behavior, while applying the same weak drive to a system that is biased with a small DC current (or no current at all), will lead to a largely linear response.

In contrast to the situations just discussed, in the experiment done at the Syracuse University and studied in the rest of this chapter, the behavior of the DC–SQUID oscillator was explored while it was excited with a brief transient signal. This meant the oscillator was pulsed with a short waveform with a cosine shape and a Gaussian–like envelope. Two different lengths of these pulses were experimentally looked at, the first of 1 ns, and the other of 5 ns. The implications of these numbers will be explored in Sec. 4.6 and beyond, but in it is worth mentioning that especially the shorter 1 ns pulse was roughly of the order of inverse natural frequency of the DC–SQUID oscillator.

In the next section, we will describe the actual experimental setup and explore some of the implications that certain parameter choices had on the general behavior of the system and subsequent theoretical modeling and simulations.

4.2 Experimental Setup

As was already mentioned, the experimental setup built at Syracuse, centers around a DC–SQUID shunted by a large capacitor. An optical micrograph of the fabricated device is shown in Fig. 4.1(a), with a zoomed–in view that lets one see the geometry of the complete system in more detail. Fig. 4.1(c), presents a schematic of the corresponding circuit, which, along with the DC–SQUID and shunt capacitor, also depicts the input and output capacitors, which will have an influence on the effective quality factor of the full circuit oscillator. Finally, Fig. 4.1(b), outlines the general path taken by the input pulses during an experimental run. The generation of these fast bias microwave waveforms was achieved by employing a FPGA based DAC board controlled by a computer. These pulses were then passed through a Gaussian filter, and later mixed with a carrier tone, producing a short microwave burst. The amplitude of the pulses could be controlled by varying extra attenuation with a step attenuator, which is shown in the diagram. The signal was attenuated even further, as it entered various stages of the fridge. It then interacted with the sample, that was enclosed in an aluminum box for magnetic shielding, which in turn was anchored to the cold plate of the ^{3}He fridge. The transmitted signal was then amplified by two High Electron Mobility Transistor (HEMT) amplifiers at the 4K stage of the fridge and another at room temperature, with a combined gain of 70 dB, and finally measured at room temperature by a sampling scope.

The Josephson junctions that make up the DC–SQUID, were fabricated out of Al-AlO$_x$–Al, and formed by a double–angle shadow–evaporation method [33]. The junctions were sub–micron in size, namely $530 \times 160\,\mathrm{nm}^2$, and with a single junction capacitance estimated to be 10 fF. Furthermore, by measuring the normal state resistance of a very similar junction, and through previous characterization of other samples [30], the single junction critical current was estimated to be $0.4\,\mu$A. A 150 nm film layer of SiO$_2$ formed a dielectric for both the shunt capacitor C_t, as well as the output capacitor C_{out}. The input capacitor C_{in} on the other, hand was interdigitated and was formed along with the microwave feed line in a 200 nm layer thick Al. While the standalone frequency of the DC–SQUID could be estimated at more than 100 GHz, the shunt capacitor C_t was chosen very large relative the single junction capacitances, which was meant to lower the effective frequency of the oscillator circuit to the much more manageable few GHz. The implications of this, will be explored in detail in Sec. 4.3. Also, the final numerical values of all the parameters that were used in circuit simulations will be discussed in Sec. 4.4 the DC–SQUID measurement and calibration procedures will be outlined. For an ever more detailed discussion of the experimental setup, we point the reader to [6].

4.3 System Model

We are now ready to look at a more detailed picture of the circuit and discuss how it can be modeled. We will start by analyzing a zero–temperature case, and later consider the effect that the thermal noise has on the evolution of the various degrees of freedom. A pictorial representation of our system is shown in Fig. 4.2(a).

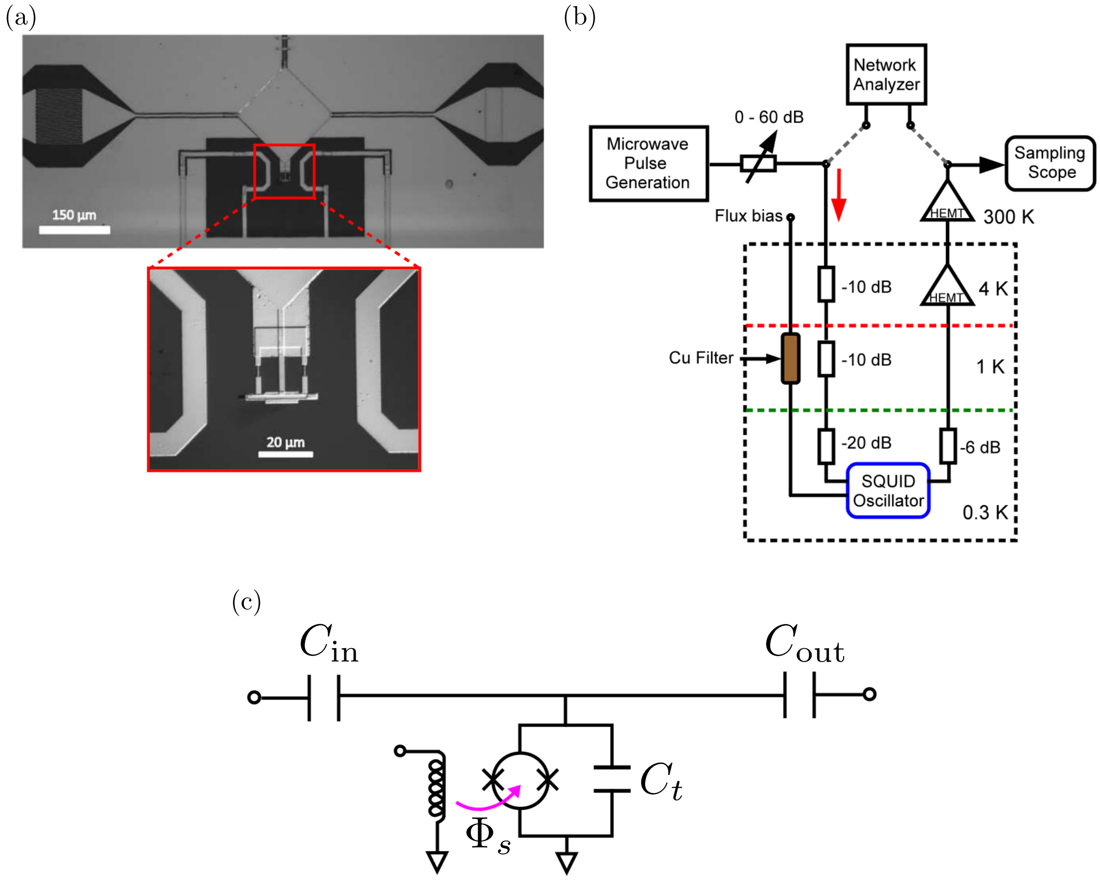

Figure 4.1: (a) Optical image of the fabricated circuit with a zoomed–in view of the DC–SQUID with on chip flux lines. (b) Schematic of general measurement setup. The network analyzer is used to measure the frequency response, while the pulse generation setup is used to measure the ringdowns in the time domain. (c) An equivalent schematic showing the input/output coupling capacitors, the DC–SQUID oscillator biased by an applied flux Φ_s and a coupling capacitor C_t. Figures created by Pradeep Bhupathi for [6] and used with permission.

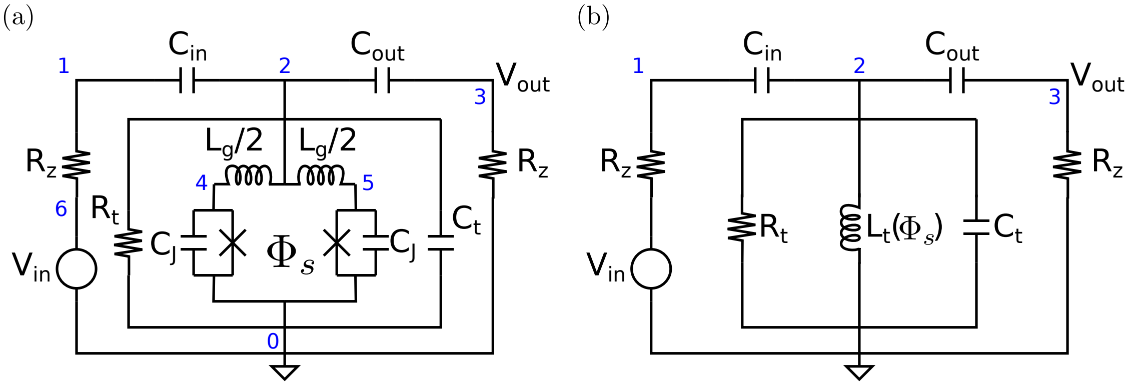

Figure 4.2: (a) Full circuit model of the SQUID oscillator of Fig. 4.1 and (b) reduced circuit, valid for at amplitude pulses, where the DC–SQUID is treated as an effective, flux–dependent inductance L_t.

The circuit is divided into branches, each a simple lumped element. As already mentioned in previous sections, the DC–SQUID is shunted by a large capacitor, and a noisy resistor (at temperatures $T > 0$), and connected to the input and output circuitry by capacitors C_{in} and C_{out} respectively. The connecting transmission lines are modeled as $50\,\Omega$ resistors. Our model assumes that the external flux is delivered directly to the DC–SQUID loop, and other branches have no intrinsic geometric inductance. We further neglect the mutual inductance in the system other than the one that mediates the external flux Φ_s. Finally, it is worth stressing that we assume the Josephson junctions that make up the DC–SQUID are themselves lossless, although this point will be discussed further in Sec. 4.5.

4.3.1 Zero–temperature Equations of Motion

To obtain the equations of motion in the zero–temperature case, we follow the methods shown in [16, 32], that were already discussed in some detail in chapter 2. With each node i, we associate a corresponding node flux Φ_i related to a node voltage by $\Phi_i = \int_{-\infty}^{t} dt' V(t')$. We express the currents across elements in terms of Φ_i, and using Kirchoff's current conservation conditions at each node i, arrive at the equations of motion

$$\begin{aligned}
\frac{1}{R_z}(V_{\text{in}} - \dot{\Phi}_1) =& C_{\text{in}}(\ddot{\Phi}_1 - \ddot{\Phi}_2) \\
C_{\text{in}}(\ddot{\Phi}_1 - \ddot{\Phi}_2) =& \frac{2}{L_g}(\Phi_2 - \Phi_4 + \Phi_s) + \frac{2}{L_g}(\Phi_2 - \Phi_5) \\
&+ C_t\ddot{\Phi}_2 + \frac{1}{R_t}\dot{\Phi}_2 + C_{\text{out}}(\ddot{\Phi}_2 - \ddot{\Phi}_3) \\
C_{\text{out}}(\ddot{\Phi}_2 - \ddot{\Phi}_3) =& \frac{1}{R_z}\dot{\Phi}_3 \\
\frac{2}{L_g}(\Phi_2 - \Phi_4 + \Phi_s) =& I_0 \sin\left(\Phi_4 \frac{2\pi}{\Phi_0}\right) + \frac{1}{R_i}\dot{\Phi}_4 + C_J\ddot{\Phi}_4 \\
\frac{2}{L_g}(\Phi_2 - \Phi_5) =& I_0 \sin\left(\Phi_5 \frac{2\pi}{\Phi_0}\right) + \frac{1}{R_i}\dot{\Phi}_5 + C_J\ddot{\Phi}_5
\end{aligned}$$

Next, taking the flux quantum $\Phi_0 = 2.07 \times 10^{-15}\text{Wb} = 2\pi\phi_0$, we perform a change of variables so that $\Phi_i = \frac{\Phi_0}{2\pi}\varphi_i = \phi_0\varphi_i$ — here, a difference $\varphi_i - \varphi_j$ for some $i \neq j$, corresponds to the superconducting phase difference. We further take $\varphi_\pm = \frac{1}{2}(\varphi_4 \pm \varphi_5)$, $C_\Sigma = C_{\text{in}} + C_{\text{out}} + C_t$, $L_J = \Phi_0/2\pi I_0$ and rewrite the external flux Φ_s in terms of the ratio $f_s = \frac{\Phi_s}{\Phi_0}$. After dividing all equations by ϕ_0, we have

$$\begin{aligned}
0 =& C_{\text{in}}\ddot{\varphi}_1 - C_{\text{in}}\ddot{\varphi}_2 + \frac{1}{R_z}\dot{\varphi}_1 - \frac{1}{\phi_0 R_z}V_{\text{in}} \\
0 =& - C_{\text{in}}\ddot{\varphi}_1 + C_\Sigma\ddot{\varphi}_2 - C_{\text{out}}\ddot{\varphi}_3 + \frac{1}{R_t}\dot{\varphi}_2 + \frac{4}{L_g}\left(\varphi_2 - \varphi_+ + \pi f_s\right) \\
0 =& - C_{\text{out}}\ddot{\varphi}_2 + C_{\text{out}}\ddot{\varphi}_3 + \frac{1}{R_z}\dot{\varphi}_3 \\
0 =& 2C_J\ddot{\varphi}_+ + \frac{2}{L_J}\sin\varphi_+\cos\varphi_- - \frac{4}{L_g}\left(\varphi_2 - \varphi_+ + \pi f_s\right) \\
0 =& 2C_J\ddot{\varphi}_- + \frac{2}{L_J}\sin\varphi_-\cos\varphi_+ - \frac{4}{L_g}\left(-\varphi_- + \pi f_s\right).
\end{aligned} \tag{4.1}$$

Thus, we end up with equations of motion of five degrees of freedom.

Elimination of Fast Degrees of Freedom

In order to further simplify Eqs. 4.1, we note that in our case, the capacitances (or "effective masses") of oscillators φ_+ and φ_- are two order of magnitude smaller than that of φ_2. This is due to the large shunt capacitor C_t, which in turn directly affects φ_2. Furthermore, the Josephson inductance L_J is much greater than the geometric inductance L_g – we can express this condition in terms of a parameter $\beta_L = L_g/L_J$, as simply $\beta_L \ll 1$. This allows us to apply a Born–Oppenheimer–like approximation and eliminate the fast-oscillating degrees of freedom φ_+ and φ_-. To do this, we first define a potential energy U that can be associated with our system. Neglecting terms due to the external drive, we have

$$\frac{U}{2E_J} = -\cos\varphi_+ \cos\varphi_- + \frac{1}{\beta_L}\left(\varphi_- - \pi f_s\right)^2 + \frac{1}{\beta_L}\left(\varphi_+ - (\varphi_2 + \pi f_s)\right)^2 . \tag{4.2}$$

Next, we fix the slow variable φ_2, and note that since $\beta_L \ll 1$, the second and third terms in Eq. 4.2 will dominate. Hence the minima of U will be close to $\varphi_+ = \varphi_2 + \pi f_s$ and $\varphi_- = \pi f_s$. By expanding U near these points, and minimizing, we can calculate the corrections to the minimum points. Keeping terms up to second order in β_L we arrive at

$$\begin{aligned} \varphi_-^{\min} =& \pi f_s - \beta_L \frac{\sin(\pi f_s)\cos(\pi f_s + \varphi_2)}{2} \\ &+ \beta_L^2 \frac{\cos(\pi f_x)\sin(\pi f_x)\cos(2(\pi f_x + \phi_2))}{4}, \end{aligned} \tag{4.3}$$

$$\begin{aligned} \varphi_+^{\min} =& \pi f_s + \varphi_2 - \beta_L \frac{\cos(\pi f_s)\sin(\pi f_s + \varphi_2)}{2} \\ &+ \beta_L^2 \frac{\cos(\pi f_x + \varphi_2)\sin(\pi f_x + \varphi_2)\cos(2\pi f_x)}{4}. \end{aligned} \tag{4.4}$$

These results are then substituted back into the expanded potential energy which leads to

$$U_{\text{eff}} = U_0 + U_1 + U_2, \tag{4.5}$$

now only in terms of φ_2, and with

$$\frac{U_0}{2E_J} = -\cos(\pi f_s)\cos(\varphi_2 + \pi f_s), \tag{4.6}$$

$$\frac{U_1}{2E_J} = -\frac{\beta_L}{2}\left(\sin^2(\pi f_s)\cos^2(\pi f_s + \varphi_2) + \cos^2(\pi f_s)\sin^2(\pi f_s + \varphi_2)\right), \tag{4.7}$$

and finally

$$\begin{aligned} \frac{U_2}{2E_J} =& \frac{\beta_L^2}{8}\big(\cos(\pi f_x)\sin^2(\pi f_x)\cos^3(\pi f_x + \varphi_2) \\ &+ \cos(\pi f_x + \varphi_2)\sin^2(\pi f_x + \varphi_2)\cos^3(\pi f_x) \\ &- 2\cos(\pi f_x)\cos(\pi f_x + \varphi_2)\sin^2(\pi f_x)\sin^2(\pi f_x + \varphi_2)\big). \end{aligned} \tag{4.8}$$

We have distinguished between the various contributions to the effective potential energy by specifying terms of different orders in β_L, namely with each U_i showing the contribution of the ith order term in β_L. It is worth stressing that U_2, for the set of numerical parameters used in the experiment, will have very little impact on the evolution of the system, and hence will be neglected in the simulations, but is still shown here for completeness. Putting it all together, we can write a set of effective equations of motion with U_{eff} as the potential energy, while keeping terms up to $O(\beta_L)$ as

$$\begin{aligned}
0 =& C_{\text{in}}\ddot{\varphi}_1 - C_{\text{in}}\ddot{\varphi}_2 + \frac{1}{R_z}\dot{\varphi}_1 - \frac{1}{\phi_0 R_z}V_{\text{in}} \qquad (4.9)\\
0 =& - C_{\text{in}}\ddot{\varphi}_1 + C_{\Sigma}\ddot{\varphi}_2 - C_{\text{out}}\ddot{\varphi}_3 + \frac{1}{R_t}\dot{\varphi}_2 + \frac{2}{L_J}\cos\left(\pi f_s\right)\sin\left(\varphi_2 + \pi f_s\right)\\
& - \beta_L\left(\frac{\sin(4\pi f_s + 2\varphi_2) + \sin(2\varphi_2)}{2L_J}\right) \qquad (4.10)\\
0 =& - C_{\text{out}}\ddot{\varphi}_2 + C_{\text{out}}\ddot{\varphi}_3 + \frac{1}{R_z}\dot{\varphi}_3. \qquad (4.11)
\end{aligned}$$

These represent a "standard" (non–stochastic) set of nonlinear differential equations and are valid when the effects of thermal noise are neglected. Our next step is to account for the nonzero temperature of the system.

4.3.2 Thermal Noise

We find that the accounting for thermal noise is of particular importance when reproducing the behavior of the experimental system in our simulations. In order to model these effects, we assume white noise and use the thermodynamic dissipation-fluctuation relation [98]. This consists of including a current noise source of strength $\sqrt{\frac{2k_B T}{R_i}}n_i$ in parallel with each resistor R_i. We take k_B to be the Boltzman constant, T the temperature of the system, and each $n_i(t)$ to represent a normally distributed random variable. Furthermore we assume that it satisfies the following equations

$$\begin{aligned}
\langle n_i(t)\rangle =& 0\\
\langle n_i(t)n_j(t')\rangle =& \delta(t-t')\delta_{i,j}.
\end{aligned} \tag{4.12}$$

Taking such noise into account, lets us write Eqs. 4.11, now in vector form as

$$\phi_0\mathbf{C}\ddot{\vec{\varphi}} + \phi_0\mathbf{R^{-1}}\dot{\vec{\varphi}} + \frac{1}{\phi_0}\vec{\nabla}_{\varphi}U_{\text{eff}} + \mathbf{N}\vec{n} + \vec{I}_{\text{dr}} = 0. \tag{4.13}$$

Here $\vec{\varphi} = (\varphi_1, \varphi_2, \varphi_3)^T$, $\vec{\nabla}_\varphi = (\partial/\partial\varphi_1, \partial/\partial\varphi_2, \partial/\partial\varphi_3)^T$, $\vec{I}_{\text{dr}} = (-V_{\text{in}}/R_z, 0, 0)^T$ and $\vec{n} = (n_1, n_2, n_3)^T$. The matrices corresponding to $\mathbf{C}$ and $\mathbf{R^{-1}}$ can be written as

$$\mathbf{C} = \begin{pmatrix} C_{\text{in}} & -C_{\text{in}} & 0 \\ -C_{\text{in}} & C_\Sigma & -C_{\text{out}} \\ 0 & -C_{\text{out}} & C_{\text{out}} \end{pmatrix}, \mathbf{R^{-1}} = \begin{pmatrix} \frac{1}{R_z} & 0 & 0 \\ 0 & \frac{1}{R_t} & 0 \\ 0 & 0 & \frac{1}{R_z} \end{pmatrix}, \tag{4.14}$$

and $\mathbf{N}$ as simply

$$\mathbf{N} = \sqrt{2k_B T \mathbf{R^{-1}}}. \tag{4.15}$$

U_{eff} represents the effective (undriven) potential energy derived in Sec. 4.3.1, however with only terms up to order $O(\beta_L)$, since higher order terms have little observable effects on the evolution. Hence we can write

$$\vec{\nabla}_\varphi U_0 = \begin{pmatrix} 0 \\ 2E_J \cos(\pi f_s) \sin(\varphi_2 + \pi f_s) \\ 0 \end{pmatrix}, \tag{4.16}$$

and

$$\vec{\nabla}_\varphi U_1 = \beta_L \begin{pmatrix} 0 \\ -\frac{E_J}{2} \left(\sin(4\pi f_s + 2\varphi_2) + \sin(2\varphi_2)\right) \\ 0 \end{pmatrix}. \tag{4.17}$$

The Eqs. 4.13 form a set of stochastic (often called Langevin) differential equations. We can numerically solve them for any φ_i, but each solution only gives us a single "realization". In order to compare simulations to data obtained from the experiment, we can average many such realizations, which will be shown explicitly in the following sections. A discussion that presents the details of numerically solving Eqs. 4.13 is shown in Appendix E.

4.4 Measurement and Parameter Estimation

In order for us to be able to simulate the experimental system, we need to establish numerical values of the different circuit parameters. This was done at Syracuse through calibration procedures and axillary measurements, which will be discussed in this section. As already mentioned, the full circuit diagram which labels all the unknown variables, is shown in Fig. 4.2(a). The geometric inductance of the circuit was calculated via finite–element methods, using a program called FastHenry [68]. It resulted in a value of $L_g = 43 \times 10^{-12}$H. Both the input and output load resistors, which effectively modeled transmission lines that coupled the DC–SQUID oscillator to the outside world were taken as $R_z = 50\,\Omega$. Furthermore, as already mentioned in Sec. 4.1, the critical current of each of the Josephson junctions that makes up the DC–SQUID, was estimated to be $0.4\,\mu$A by separate room–temperature measurements.

In order to obtain numerical values for the rest of the parameters, the 2–port transmission function $|S_{21}|$ was obtained for our particular circuit. This was done by sending a weak continuous signal with a typical power of $-125\,\mathrm{dBm}$ to the input of the DC–SQUID oscillator, while measuring and recording the output. The transfer function is defined as $S_{21} = 2V_{\mathrm{out}}/V_{\mathrm{in}}$, such that the matched load of $R_z = 50\,\Omega$ would give a full transmission, meaning $S_{21} = 1$.

To calculate $|S_{21}|$ that can be compared with the experimental measurements, we used a simplified model circuit of our system, shown in Fig. 4.2(b). Here, it was assumed that the drive is necessarily weak, and therefore the response of the DC–SQUID will be linear. In this limit, and continuing with assumptions presented in Sec. 4.3 of $\beta_L \ll 1$, and dominating shunt capacitance C_t, the DC–SQUID was modeled as just an effective inductance L_t, which was taken as time–independent, but varied as a function of the applied flux Φ_s. One way to calculate such L_t, is to directly use the DC–SQUID potential energy shown in Eq. 4.5. We can Taylor–expand it around a minimum (i.e., a steady state value) of φ_2, call it φ_2^{min}, which results in[1]

$$L_t = \phi_0^2 \left(\left.\frac{\partial^2 U_{\mathrm{eff}}}{\partial \varphi_2^2}\right|_{\varphi_2=\varphi_2^{\mathrm{min}}} \right)^{-1} . \tag{4.18}$$

We assume that φ_2^{min} can be calculated numerically for a given fixed value of the applied flux Φ_s by minimizing the potential energy from Eq. 4.5. For brevity, we do not explicitly show this expression, as it is long, but can be easily obtained. Hence using Eq. 4.18, we can think the DC–SQUID along with the shunt capacitance C_t, and the resistance R_t, which models the internal losses due to the DC–SQUID shunt capacitance, as a simple parallel LCR circuit. The final step is to account for the input and output capacitances C_{in} and C_{out} as well as the load resistances R_z. We once again stress that in our model we assume that the junctions were lossless.

Hence finally taking the $\parallel$ symbol to represent parallel impedance, we arrive at an expression for S_{21} which reads

$$\begin{aligned} S_{21}(\omega, \Phi_s) =& \frac{2V_{\mathrm{out}}}{V_{\mathrm{in}}} \\ =& 2\frac{R_z}{Z_{\mathrm{out}}} \frac{(Z_t \parallel Z_{\mathrm{out}})}{(Z_t(\Phi_s) \parallel Z_{\mathrm{out}}) + Z_{\mathrm{in}}}, \end{aligned} \tag{4.19}$$

---

[1] There are various ways to approximate L_t, and a detailed discussion on this topic is presented in Appendix D.

where Z_t is the combined impedance of the parallel LCR tank circuit,

$$Z_t(\Phi_s) = \left(\frac{1}{R_t} + \frac{1}{i\omega L_t(\Phi_s)} + i\omega C_t\right)^{-1} \tag{4.20}$$

and $Z_{\text{in}} = \left(R_z + \frac{1}{i\omega C_{\text{in}}}\right)$, $Z_{\text{out}} = \left(R_z + \frac{1}{i\omega C_{\text{out}}}\right)$ are the input and output impedances respectively.

During the measurement, multiple $|S_{21}|$ traces were recorded for various values of the applied flux through the DC–SQUID, which effect was to vary the natural frequency of the circuit. A resulting density plot of $|S_{21}|$ is shown in Fig. 4.3.

The horizontal axis represents the applied flux in the units of single flux quantum Φ_0, the vertical axis the frequency of the applied signal, while the out–of–page direction the amplitude of the resulting output pulse. The magenta symbols corresponds to peaks of the numerical fit to the S_{21} function shown in Eq. 4.19. To fit this resonance, $I_0 = 0.4\mu$A, $C_{\text{in}} = 0.15$pF and $L_g = 43$pH were fixed while C_t, C_{out} and R_t were allowed to vary (for a given fixed applied flux Φ_s). Measured S_{21} curves between $\pm 0.5\Phi_0$ were fit with the same fixed parameters and the best fit parameters extracted. This resulted in the following: $R_t = 264.9\,\Omega$, $C_t = 5.07$pH, $C_{\text{out}} = 0.99$pH, which could be used in the simulations discussed in the following sections. A function of the form $f(\Phi_s) = \sqrt{a + b|\cos(c\Phi_s + d)|}$ was also used to fit these resonance peaks between $\pm 0.3\,\Phi_0$ to extract the periodicity and scale the flux axis with the fit parameters a, b, c and d. $f(\Phi_s)$ is shown in grey dashed line on top of the measured S_{21} plot in Fig. 4.3. From the plot in Fig. 4.3, we observe that the frequency is periodic in the applied flux Φ_s, highest at ~ 3.2 GHz at $\Phi_s = n\Phi_0$, with n integer, and lowest, close to zero, near $\Phi_s = \frac{1}{2}n\Phi_0$ – the "arches" are fully consistent with what one would expect in a system like this [117].

4.5 Model limitations

In our model, we neglect the resistance associated with each Josephson junction. This is reasonable when the amplitude of the current applied to the junctions is smaller than their critical current, as the resistance in those cases is large enough that its effect on damping of the junction's phase can be neglected. However, in the instances when the driving current exceeds the critical current, each junction feels a resistance that can be of the order of its normal–state resistance R_n [117], which for the DC–SQUID oscillator studied here is $684\,\Omega$. Nevertheless, in our circuit, the dominant source of noise is the $50\,\Omega$ outside load that couples to the DC–SQUID oscillator via C_{out} (as can be seen from Fig. 4.2). When this load is mathematically transformed as an impedance parallel with the oscillator, over the frequency ranges of the input pulses we apply, its resistive component is never more than $100\,\Omega$, hence a few times smaller than all other sources of noise in the system

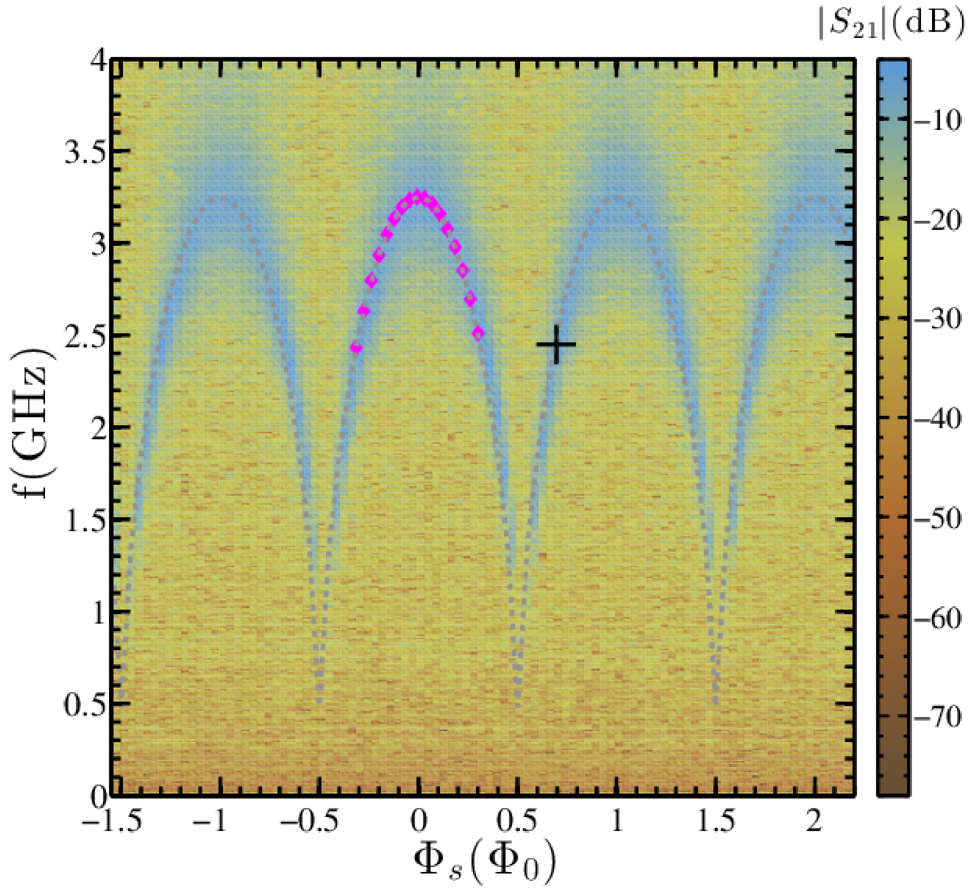

Figure 4.3: Density plot of $|S_{21}|$ vs. flux, frequency of the DC–SQUID oscillator as measured from a network analyzer at -125 dBm input power and with the DC–SQUID oscillator at 300 mK; The magnitude of $|S_{21}|$ in dB is shown in color bar to the right. The dashed line and magenta symbols are from fits to the DC–SQUID modulation as described in the text. The marker in black indicates the flux bias at which the pulsed measurements were taken. Plot created by Pradeep Bhupathi for [6] and used with permission.

(and therefore its effect is by far the most dominant, since the amplitude of the noise currents scales inversely with resistance).

Furthermore, we neglect any quantum corrections to the noise correlation function and treat it, just as the rest of the system, fully classically. This is typically a reasonable assumption in the limit of $\hbar\omega \ll 2k_BT$ with ω being the applied flux dependent, natural frequency of the oscillator circuit. In the case of the experimental parameters used here, this limit is largely satisfied, although in the worst case, when the flux through the DC–SQUID is close to integer multiple of flux quantum (where the effective natural frequency of the oscillator is largest) we are slowly approaching a case where $\hbar\omega \leq 2k_BT$. Let us then estimate the next order correction to the correlation function that one would get from considering quantum effects in the noise, and hence see how that translates to the amplitude of the noisy current in our model. To do this, we first write the noise correlation function that accounts for the quantum behavior as

$$\langle N_i(t)N_j(t')\rangle = \frac{1}{R}\hbar\omega\coth\left(\frac{\hbar\omega}{2k_BT}\right)\delta(t-t')\delta_{i,j}. \tag{4.21}$$

with

$$\langle N_i(t)\rangle = 0. \tag{4.22}$$

We can next expand the second line in of Eq. 4.21 in $\hbar\omega/2k_BT$ to obtain

$$\langle N_i(t)N_j(t')\rangle \sim \frac{2k_BT}{R}\left(1+\frac{1}{3}\left(\frac{\hbar\omega}{2k_BT}\right)^2 + O\left(\left(\frac{\hbar\omega}{2k_BT}\right)^4\right)\right)\delta(t-t')\delta_{i,j}. \tag{4.23}$$

In our case, ω is largest when the applied flux Φ_s is near integral values of Φ_0, where it was shown to be $\omega/2\pi \sim 3.2\,\text{GHz}$. Taking the experimental temperature of $T = 0.300\text{K}$ then leads to $\frac{\hbar\omega}{2k_BT} \sim \frac{1}{4}$. Substituting these values into Eq. 4.23, results in

$$\langle N_i(t)N_j(t')\rangle \sim \frac{2k_BT}{R}\left(1+\frac{1}{48} + \mathcal{O}\left(\left(\frac{\hbar\omega}{2k_BT}\right)^4\right)\right)\delta(t-t')\delta_{i,j}. \tag{4.24}$$

The first term in Eq. 4.24 is equivalent to the classical white noise correlation function shown in Eq. 4.12 (with $N_i = \sqrt{\frac{2k_BT}{R_i}}n_i$), while the second shows the first order correction due to the quantum effects. The amplitude of the noisy current can be though of as the square root of Eq. 4.24, and in the limit of the small correction can be calculated as $\sim 1/24$th of the full classical contribution. Given that this is the worst case, and this correction gets smaller as the flux that is threaded through the DC–SQUID shifts away from integer multiple of Φ_0, we neglect it in our simulations.

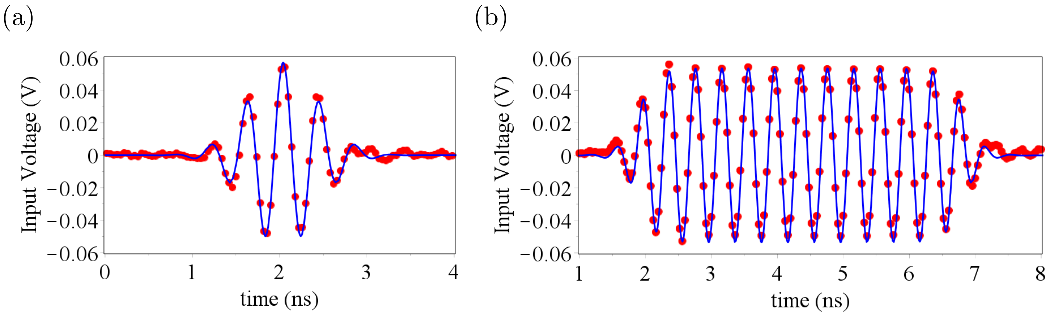

Figure 4.4: Input pulses used to excite the DC–SQUID oscillator. Each consists of a cosine with a Gaussian–like envelope (see main text for exact forms). The red dots correspond to the experimental data, while the blue curves show a fit used in simulations. (a) A short pulse represented by f_{short} from Eq. 4.25. (b) Long pulse represented by f_{long} from Eq. 4.26.

4.6 Input Pulses

In this section we briefly look at the input pulses that were used to excite the DC–SQUID oscillator in the experiment. In all cases, the pulses consisted of a cosine tone, at frequencies resonant with the DC–SQUID at a particular flux, and with an envelope that shortened them to either a "short" 1 ns or "long" 5 ns time frame. The experimental samples were fit with functions f_{short} or f_{long}, and the resulting fits were then used in the simulations. In the case of the short pulses, the fit function that works best, is simply

$$f_{\text{short}}(t) = A_d \exp\left(-\frac{(t-t_0)^2}{2\sigma^2}\right)\cos(\omega_d(t-t_0)), \tag{4.25}$$

while the long pulses were fit to

$$f_{\text{long}}(t) = A_d\left(g_d\left(t-t_0+\frac{\sigma}{2}\right) - g_d\left(t-t_0-\frac{\sigma}{2}\right)\right)\cos(\omega_d(t-t_0)), \tag{4.26}$$

with $g_d(x) = \frac{1}{\exp(-dx)+1}$, a Fermi function. In both of these, t_0 represents the center of the pulse in time, σ its "width", ω_d the angular frequency of the underlying cosine tone and A_d, the maximum pulse amplitude. The drive frequency $\omega_d/2\pi$ was taken as either 2.4 GHz, which corresponded to the DC–SQUID being at resonance near the applied flux of $\Phi_s \sim 0.30\Phi_0$, or as 3.2 GHz, which in turn corresponded to the natural frequency near the integral values of the applied flux. Fig. 4.4 shows two example 2.4 GHz pulses, both in their short (part (a)) and long (part (b)) forms. The red dots represent the experimental data, while the blue curves the corresponding fits. In the following sections we will mostly concentrate the discussion on the short 1 ns, 2.4 GHz pulses obtained using f_{short}, as arguably when

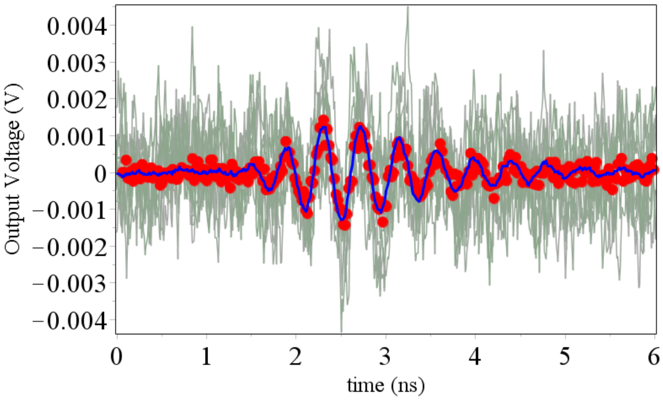

Figure 4.5: An example of an output voltage rigndown (of variable $\phi_0\dot{\varphi}_3$) when the system is exited with a short 1 ns pulse. The green lines in the background represent a small subset of single realizations that are averaged in order to produce the blue line, which in turn can be directly compared with the experiment. The experimental data for the same set of parameters as the simulations is shown with red dots.

they were used to excite the circuit, the response was most interesting, however, we will also outline differences observed when the longer pulses generated with $f_{\rm long}$ were used.

4.7 Voltage Ringdowns

While we can simulate the evolution of an arbitrary degree of freedom, of particular interest is $\dot{\Phi}_3 = \phi_0\dot{\varphi}_3$, as it corresponds to the output voltage, which is precisely what was measured in the experiment. As already mentioned, we have two controls that can be varied in a given experimental run; the applied flux ratio $f_s = \Phi_s/\Phi_0$, and the amplitude of the input pulse. The rest of the parameters are fixed and their numerical values obtained through various calibration procedures, that were already discussed in Sec. 4.4. Therefore for a given set of parameters, we can obtain a single voltage ringdown, which corresponds to a time trace of the voltage measured at the output of the circuit (at node 3 in Fig. 4.2(a)). This can then by compared to the simulations, which are repeated many times and later averaged. An example of such a ringdown is shown in Fig. 4.5. Here, the system is excited with the short 1 ns pulse. The green lines in the background represent a small subset of single realizations that we average over in order to produce the blue line, which in turn can be directly compared with the experiment. The experimental data for the same set of parameters as the simulations, namely applied flux ratio of $f_s = 0.30$, and input pulse amplitude of -20 dB, is shown with red dots. To gain some understanding of our system, it is therefore instructive to vary the control

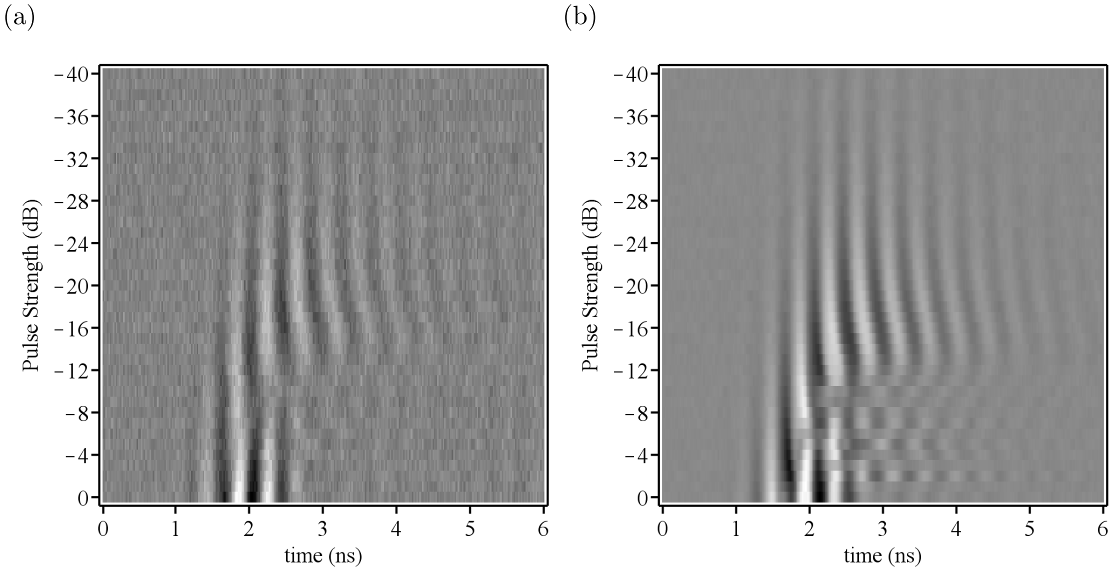

Figure 4.6: Density plots that show the amplitude dependence of ringdowns at a non–integer flux bias for the 1 ns input signal, at 2.4 GHz. (a) Experimental data. (b) Simulations. The pulse strength on y-axis is shown in the units of dB with negative numbers implying decreasing amplitude of the input pulse. The ringdown time on the x-axis is in nanoseconds, with the ringdown amplitude shown in color scale.

"knobs" — the applied flux and the amplitude of the input pulse, while measuring the resulting ringdowns. The bulk of the following discussion will concentrate on short 1 ns pulses with the underlying drive frequency (i.e. $\omega_d/2\pi$ from Eq. 4.25) of 2.4 GHz. This frequency corresponds to the effective natural frequency of the DC–SQUID circuit at the applied flux ratio of $f_s \sim 0.30$, hence by simply varying the flux around this value, we can observe the off–resonant circuit response for cases of both above and below resonance. Later, in Sec.4.9, we will conclude with a short discussion of results obtained when both longer input pulses were used, and where their frequency was resonant with DC–SQUID oscillator at a flux ratio $f_s \sim 0$.

4.8 Short Pulses

4.8.1 Amplitude Scans

We first look at amplitude scans, where we fix the applied flux ratio f_s, and vary the amplitude of the of the microwave burst, which pulses the DC–SQUID. Figure 4.6 displays density plots of such a case, obtained with experimental data (a) and from simulations (b). The flux ratio f_s is fixed at 0.30, which corresponds to the natural frequency of the DC–SQUID of $\sim$ 2.4 GHz, satisfying a resonance condition. The y-axis, is the attenuation setting from the highest (-40 dB) to the lowest attenuation (0 dB) corresponding to increasing burst amplitude and the x-axis is the ringdown time in nanoseconds. The color scale indicates the amplitude of the ringdown, darker color implying a smaller value. With increasing pulse strength, the frequency of the ringdowns starts to decrease. This becomes particularly pronounced for attenuation levels less than 20 dB. This shift to lower frequencies arises because the fictitious particle, whose position coordinate can be described by the φ_2 degree of freedom, begins to explore the nonlinear (flatter) part of the potential energy landscape. Beyond the amplitude of ~ -12 dB, we observe a sharp drop in the resulting ringdowns. The effect is due to the fact that the strength of the drive is now of the order of the critical current of the DC–SQUID. The stochastic nature of the thermal noise causes different realizations to escape the potential well at different times, which in turn causes a substantial decay in voltage ringdown strength. This phenomenon is discussed in more detail in the next section.

4.8.2 Escape from the Potential Well

The problem of particle escape from a potential well due to thermal noise, has been investigated both theoretically as well as experimentally in a variety of studies [4, 53, 56, 57, 74]. In a case of a DC–SQUID, this rate can be approximated to be proportional to $\Omega \exp\left(-U_b/k_B T\right)$ where U_b represents the potential energy barrier height that the particle has to overcome, and Ω the natural frequency along the direction of escape. In our case, since we do not “tilt” the potential with a DC biasing current, the escape time (inverse rate) can be shown to be much larger than the typical experimental run time. This is true over almost all settings of the applied flux ratio f_s, except when $f_s \simeq 0.5$, where the potential barrier is close to being flat.

Thermal fluctuations however, still end up playing an important role in the evolution of the system. In particular, we find that during strong pulses that excite the system to amplitudes in the vicinity of the DC–SQUID's critical current, the thermal fluctuations can cause a strong mixing in the phases of various realizations, resulting in a damping of the ringdowns. To our knowledge, no detailed analytical study of this effect, with strongly time depended pulses has been performed yet, but we can still study the situation numerically. To do this, we once again fix the applied flux ratio at $f_s = 0.30$ as in the previous section, and concentrate on two different pulses; the first at an amplitude of -16 dB, and the other at the amplitude of -9 dB. From Fig. 4.6, we can see that these correspond to cases where substantial ringdown voltage is observed (the former case) and where the ringdowns are dramatically suppressed (the latter case).

In order to understand this behavior in more detail, we look at the evolution of the individual realizations, that so far have been averaged to obtain results compa-

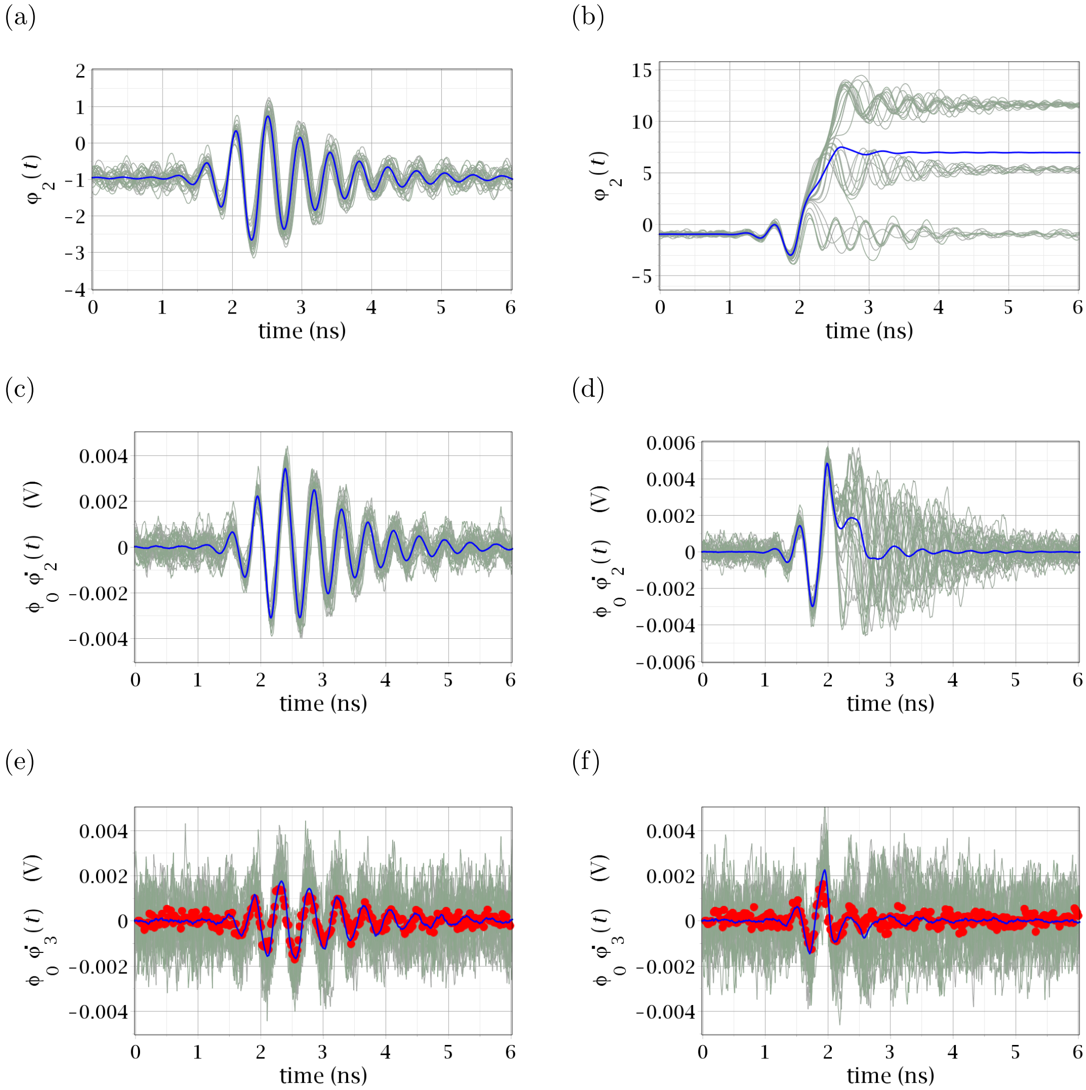

Figure 4.7: Low and high drive response. Each column shows plots of φ_2, $\phi_0\dot{\varphi}_2$ and $\phi_0\dot{\varphi}_3$ (the output voltage) respectively. In plots (a, c, e) the amplitude of the input pulse is low with respect to the effective critical current of the DC–SQUID, whereas in (b, d, f) it is high. The green curves show (a small subset) of individual realizations used to calculate the averages (blue curves). In the case of the third row we also show the experimental data for the same parameters (red dots) and how it compares to the simulation results. From the plots, one clearly sees how when the drive amplitude is low, all the realizations stay within the same potential well (see plot (a)), and their phase only varies slightly. In the case of high input signal amplitude, we observe that different realizations tend to end up in different wells at different times, as shown in plot (b), which introduces a relative phase shift between them. This in turn leads to faster decay of the average voltage across the DC–SQUID, as presented in plot (d), and at the output of the circuit, as shown in plot (f).

rable with the experiment. We should stress however, that while the behavior of the full circuit is largely governed by the dynamics of the DC–SQUID, the experiment only provides us access to the external voltage — voltage at node 3 in Fig. 4.2 — which in our simulations is represented mathematically as $\phi_0\dot{\varphi}_3$. To directly observe the stochastic nature of the escape from the potential well, we need to look at the individual realizations of the full system. Of particular interest are simulation variables φ_2, which represents the phase (i.e. the effective "position") of the DC–SQUID degree of freedom that dominates the evolution of the system, $\phi_0\dot{\varphi}_2$, which represents the voltage across the DC–SQUID (or alternatively an effective "velocity" of the particle in the well), and finally $\phi_0\dot{\varphi}_3$, which is the voltage that we can directly compare to the experimental data. Fig. 4.7 shows plots that describe the evolutions of these variables as a function of time. The left column shows data for a case of the low amplitude, $-16\,\mathrm{dB}$ pulse, while the left column shows the case of high amplitude, $-9\,\mathrm{dB}$ pulse. The topmost row represents $\varphi_2(t)$, the middle row $\phi_0\dot{\varphi}_2(t)$, and finally the bottom row the output voltage, namely $\phi_0\dot{\varphi}_3(t)$. In each case, the green curves represent (a subset of) realizations that are averaged (curves in blue). The red dots in the plots from the bottom row, represent experimental data for the same set of parameters as the simulations. The key signature of the escape can be seen in the topmost row. Here, when the pulse amplitude is low (plot (a)), virtually all the realizations stay within the same potential well — one concludes this by noting that they all oscillate around the same value of φ_2, namely $\varphi_2 \sim -0.30\pi$. In the case of the high amplitude pulse (plot (b)), different realizations "jump out" to differ potential wells. The stochastic nature of the noise causes these jumps to happen at different times, which leads to a randomly shifted phase, as well as a different steady state value of φ_2. This has a substantial effect on the "velocity" (or $\dot{\varphi}_2$) of these realizations, as shown in the central row of figure Fig. 4.7. The result is a randomization in the phase of $\dot{\varphi}_2$, and as therefore, of $\dot{\varphi}_3$, which is proportional to the output voltage of the circuit. As we see from the experimental voltage (red dots), the agreement of the measured data with the simulations is good. Finally, we stress that including the stochastic effects of thermal noise in our simulations has been crucial in reproducing this behavior.

4.8.3 Flux Scans

We explore the voltage ringdowns behavior further by studying their dependence on the magnetic flux applied to the DC–SQUID. Here, the amplitude and frequency of the microwave burst is fixed, while we vary the flux applied to the DC–SQUID through one period of a flux quantum. Initially, we study a case where the pulse frequency once again is chosen to correspond to resonance at the DC–SQUID flux ratio $f_s \sim 0.30$. The density plots of the flux modulated ringdown traces are shown in Fig. 4.8 for three different pulse amplitudes. The left column (plots (a), (c) and (e)) shows results obtained from experimental data, while the right column (plots

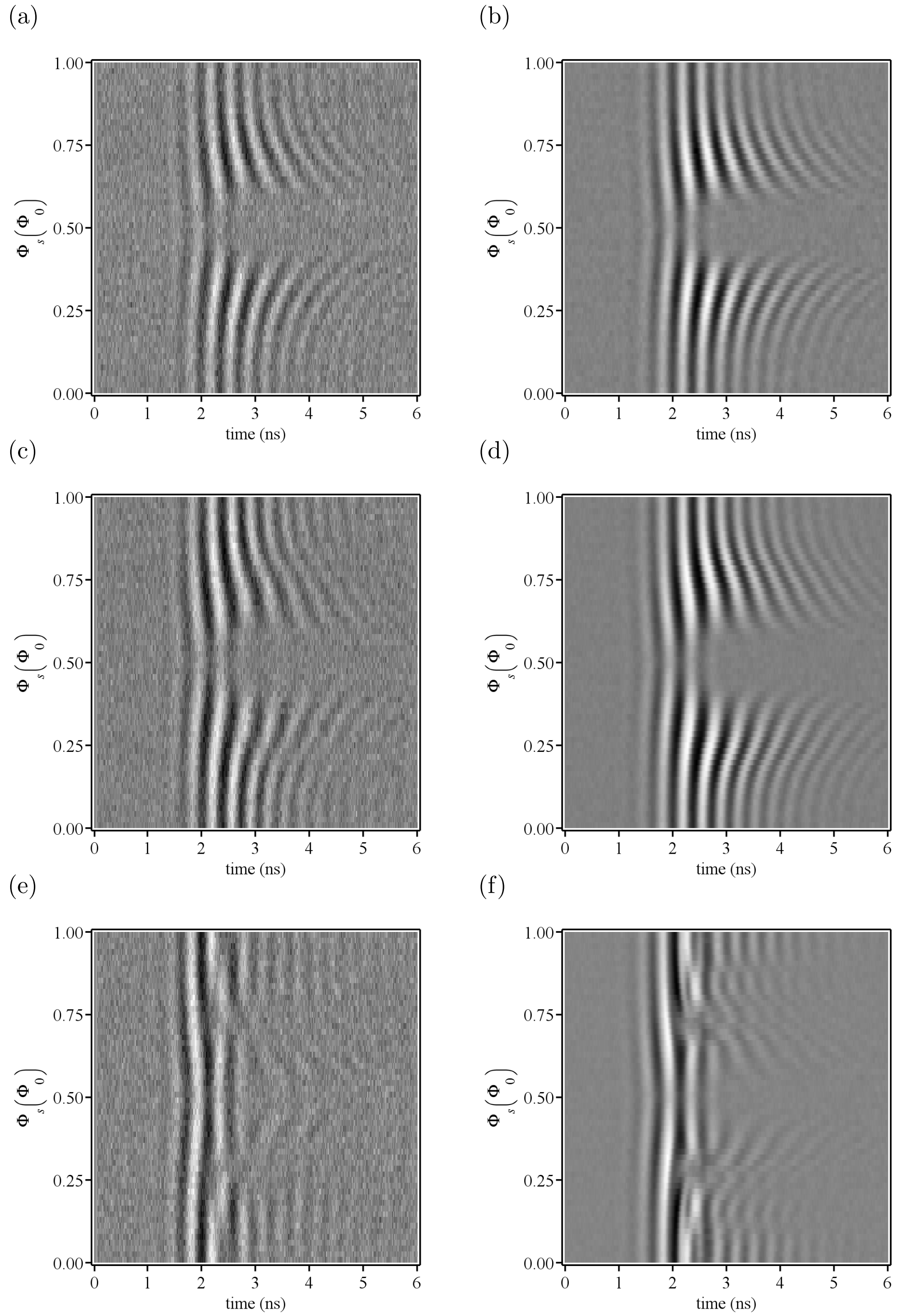

Figure 4.8: Fixed amplitude flux scans with the applied flux ratio f_s between 0 and 1, and with the 1ns at 2.4 GHz input pulse. The left column (plots (a), (c) and (e)) shows experimental data, while the right column (plots (b), (d) and (f)), uses data obtained by running stochastic simulations. The amplitude of the input pulse increases from top to bottom, with the topmost row showing results for −20 dB pulses, the middle row for −15 dB pulses and finally the bottom row for −10 dB pulses. As the amplitude increases, one clearly observes the effects of the nonlinearity of the system. See main text for a detailed discussion.

(b), (d) and (f)) shows the corresponding simulations. The topmost row has a “low” input pulse amplitude of $-20\,\mathrm{dB}$, well below the critical current of the DC–SQUID, the central row shows data for an input pulse of $-15\,\mathrm{dB}$, while the bottom row for a “high” amplitude of $-10\,\mathrm{dB}$. As before, the darker areas correspond to lower ringdown amplitudes. By varying the applied flux through the DC–SQUID, we are changing its effective inductance, and hence its natural frequency. It is worth stressing that this nonlinear dependence of the natural frequency on the applied flux is true, even in the limit of small oscillations of the DC–SQUID (where $|\varphi_2| \ll 1$), as was already discussed in Sec. 4.4. Let us first concentrate on the topmost row of Fig. 4.8. Here the drive amplitude is still small and the nonlinearity of the potential energy in φ_2 is only beginning to play a role, yet as the applied flux ratio f_s varies between 0 and 1, the ringdowns tend to “fan out”. As expected, the amplitude is largest near the flux ratio of $f_s \sim 0.30$, since this is where the DC–SQUID is resonant with the input pulse, and it is suppressed elsewhere. The results are also consistent with the fact that the natural frequency (up to zeroth order in β_L), is proportional to $\sqrt{\cos(\pi f_s)}$. Hence, near $f_s \sim 0$, the variations in the ringdown structure are small, while at the same time, one sees a very abrupt suppression near $f_s \sim 0.5$. Here the effective natural frequency of the DC–SQUID is very small and the short input pulse is just not able to induce strong oscillations. This is an adiabatic regime, where the excitation of the circuit strongly follows the input pulse. This ringdown suppression due to a highly off–resonant pulse can be confirmed further by studying individual realizations, and showing that they stay in the same potential energy well as they started in (in contrast to what is observed during an escape — see Sec. 4.8.2). Furthermore, a very similar ringdown structure can be obtained in a case where a simple harmonic oscillator, with the same flux dependent form of natural frequency, is driven with the same pulse. The situation is largely similar in the middle row of Fig. 4.8. The key difference here, is that now not only is the natural frequency of the system nonlinear in the applied flux, but the amplitude of the input pulse is large enough for the DC–SQUID degree of freedom φ_2, to start exploring the nonlinear regions of the potential energy well, in particular around the applied flux for which the DC–SQUID is resonant with the input pulse (near $f_s \sim 0.30$). This in turn affects the degree of variation of the ringdown frequency with respect to f_s, as can be seen in the plots. Finally, in the bottom row we see a case of a strongly driven system. The resulting plots show an overall suppression of ringdown oscillations across all values of f_s, when compared to the instances with smaller drive amplitudes. In this case, the reason is two–fold. By once again studying the individual realizations as in Sec. 4.8.2, we can conclude that for the applied flux away from $f_s = 0.5$, the main contribution to the suppression, is the randomization of the phase of φ_2 due to the stochastic escape from the potential well. Near $f_s = 0.5$ however, as in the case of low amplitude pulses, the main reason for the suppression is the off–resonance condition where the frequency of the pulse is much greater that the natural frequency of the DC–SQUID.

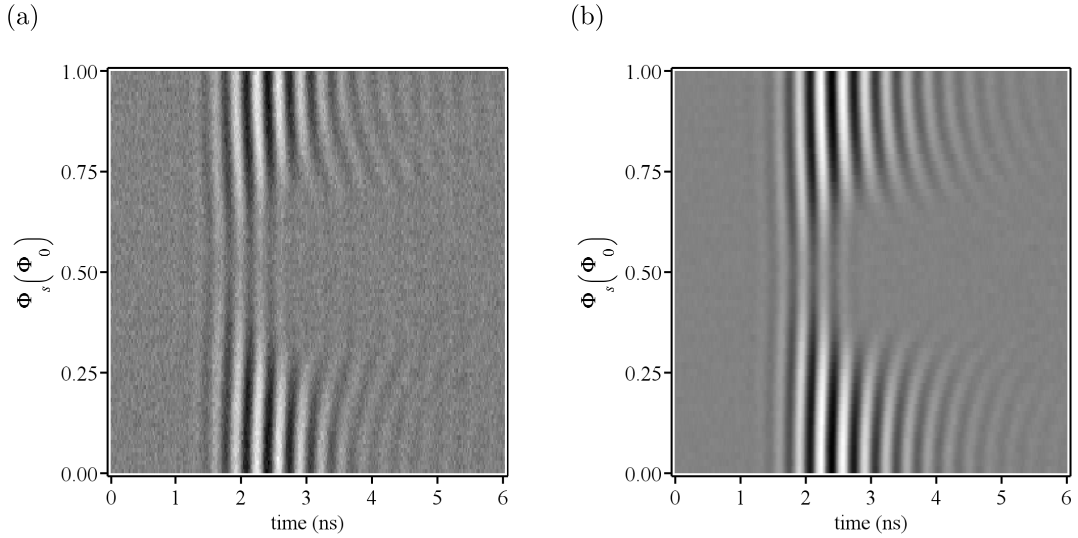

Figure 4.9: Flux scans due to fixed amplitude (at $-15\,\mathrm{dB}$), 1ns, at $3.2\,\mathrm{GHz}$ input pulses. Plot in (a) shows experimental results whereas (b) the corresponding simulations. The response is largest near $f_s = 0$ where the input signal is resonant with the system.

Before we move onto longer pulses, let us also consider a case where the driving signal is still governed by Eq. 4.25, but where the underlying drive frequency $\omega_d/2\pi = 3.2\,\mathrm{GHz}$. In this situation, the input signal is at resonance with the DC–SQUID at the integral values of the applied flux — namely where $f_s = 0$. The resulting flux scans are shown in Fig. 4.9, where once again the plot on the left, in (a) shows data obtained experimentally and on the right, in (b) from simulations. As we would expect, one sees the strongest response near resonance, and the ringdowns are seen to decay away as the applied flux ratio f_s approaches 0.5. The associated decrease in the resulting frequency of the voltage ringdowns as the applied flux changes from $f_s = 0$ is still visible, but it happens at a slower rate than in the case of Fig. 4.8 where the pulse was resonant at $f_s = 0.30$. Once again this is because the natural frequency dependence of the DC–SQUID on the applied flux is smallest near $f_s = 0$.

4.9 Long Pulses

In this section, we can move onto a brief discussion of the longer pulses that were studied in the experiment. As was outlined in Sec. 4.6, the functional form of these was slightly different from the short pulses that were used in the last section. In f_{short} from Eq. 4.25, the envelope is a Gaussian function, while in f_{long} from Eq. 4.26 a combination of Fermi functions. Even so, the arguments describing the response

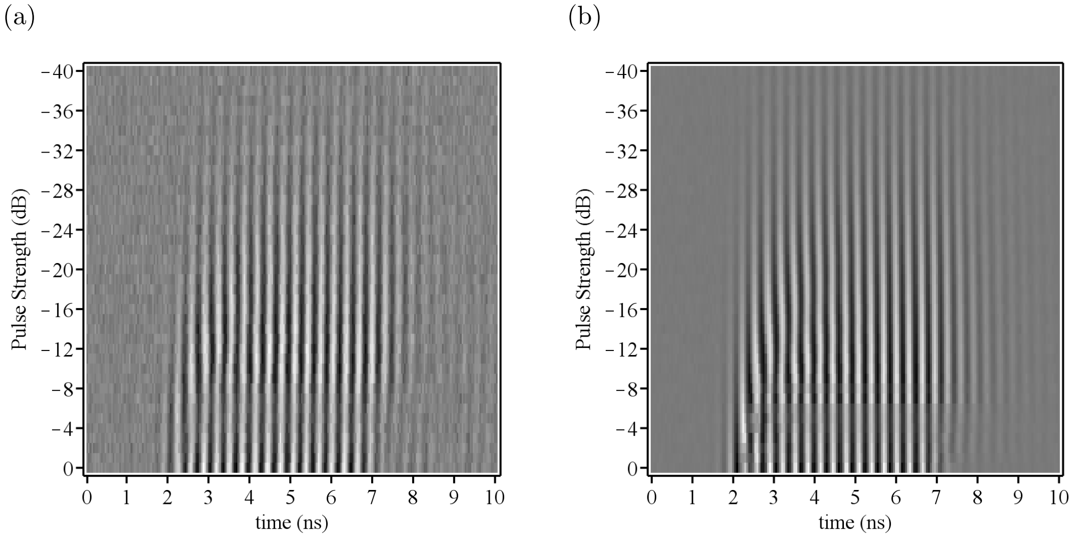

Figure 4.10: A comparison of the amplitude dependence of ringdowns at a non–integer flux bias for a “long” 5 ns input signal, at 3.2 GHz. (a) Experimental data. (b) Simulations. The pulse strength on the y-axis is shown in units of dB, with negative numbers implying decreasing amplitude of the input pulse. The ringdown time on the x-axis is in nanoseconds. The ringdown amplitude is shown in color scale, with darker colors representing lower values.

of the DC–SQUID circuit are largely the same.

First, let us look at an amplitude scan of a 5 ns input pulse at 3.2 GHz, that is modeled in simulations using f_{long} from Eq. 4.26. As outlined in the last paragraph of the previous section, this kind of pulse is resonant with the DC–SQUID circuit at the applied flux ratio of $f_s = 0$. The general structure of the output signal is similar to what was shown in Sec. 4.8.1, but now the excitation lasts longer. We also observe a significant reduction in the ringdown amplitude past a certain level of attenuation — in this case this level is few dB larger than in the case of the 2.5 GHz pulses shown earlier, namely near -9 dB. The mechanism here is identical to what we studied in Sec. 4.8.2 — the thermal noise causes different realizations to escape the potential energy well at different times, which in turn leads to a randomization of the phase across the DC–SQUID (φ_2), and therefore the resulting voltage across both the DC–SQUID ($\phi_0\dot{\varphi}_2$) and the output load resistor ($\phi_0\dot{\varphi}_3$). The reason why in the case of short 2.4 GHz pulses studied earlier, this decay was observed at a lower value of attenuation (weaker signal), can be attributed to the fact that when the circuit was excited with 2.4 GHz pulses, the corresponding applied flux was set at $f_s = 0.30$, while in case of 3.2 GHz pulses, it was at $f_s = 0$. This resulted in the potential well being deeper in the latter scenario, which in turn required stronger excitations before escape could be observed.

The final plots we present, are flux scans that are a result of long input pulses,

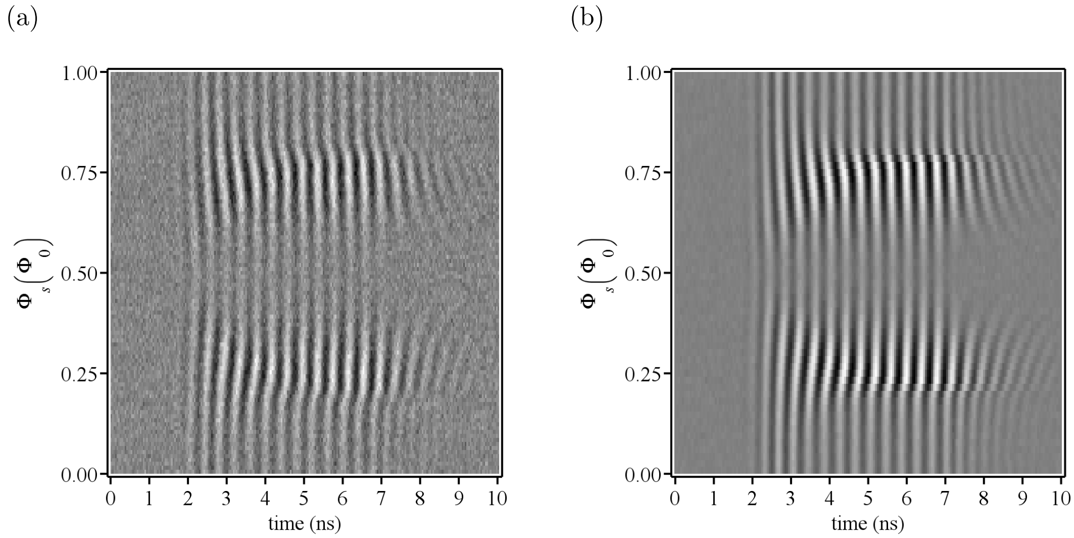

Figure 4.11: Fixed amplitude flux scans with the applied flux ratio f_s between 0 and 1, and with the 5 ns at 2.5 GHz input pulse. (a) Experimental data. (b) Simulations.

at[2] 2.5 GHz, and applied at an amplitude of −21 dB. The resulting ringdowns are shown in Fig. 4.11. The actual input signal is active over the time range $\sim 2-7$ ns, as can bee seen from Fig. 4.4(b). As we would expect, results show excitations with highest amplitudes near the flux of 0.30, where the circuit is resonant with the driving signal. Furthermore, during the now longer drive we see substantial oscillations even away from the resonance, but as soon as the drive is turn off, past the time of $\sim$ 7 ns, one can observe a similar structure to that of Fig. 4.8(a) and (b).

4.10 Application to Flux Measurements

The high sensitivity of DC–SQUIDs to magnetic flux makes them useful in applications related to precise flux detection. They have been played a central role in various metrology experiments [25, 26, 35, 79, 83] and more recently in the field of quantum computing, as measurement devices for flux qubits [22, 27, 81, 120, 123]. In these proposals, a flux qubit is typically coupled inductively to a DC–SQUID and hence affects the net applied flux that is threaded through the device. The two most widely used modes of operation in these approaches, have been to either

---

[2] The reason why the frequency of the drive in the input pulse used here is 2.5 GHz and not 2.4 GHz as in the case of short pulses, is simply that it was better fit of the input pulse $f_{\rm long}$ shown in Eq. 4.26 to the experimental data provide by the Syracuse team. The flux was still biased at $f_s = 0.30$, in order to stay consistent with the experiment.

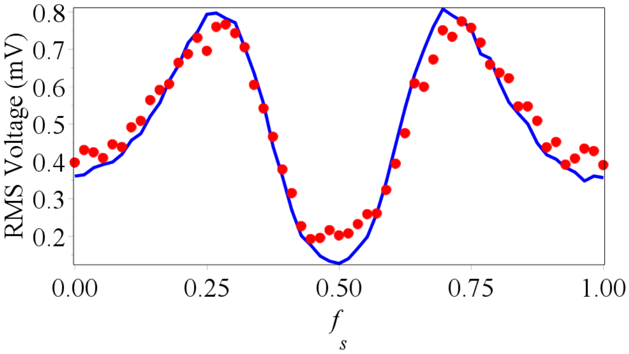

Figure 4.12: Root mean square voltage V_{rms} as a function of the applied flux ratio f_s, calculated over a time range between 2.1 and 3.4 ns. The plot uses data obtained with the -20 dB amplitude input pulses, and is the same as in top row of the flux scans from Fig. 4.8. The red dots represent results calculated from the experimental data (plot (a) in Fig. 4.8), while the solid red line is produced using the simulations (plot (b) in Fig. 4.8). By biasing the flux through the DC–SQUID near a point where the slope is high, for example at $f_s \sim 0.36$, one can have a means to distinguish between various flux states.

bias a DC–SQUID with an appropriately selected DC current, such that the DC–SQUID is put in a "running state" (where the voltage across is nonzero) with a high probability if a qubit is in one state, and with negligible probability when the qubit is the other state, or alternatively, instead of a DC current bias, to drive the DC–SQUID with a continuous sinusoidal signal, and observing a resulting phase shift that is qubit–state dependent. Yet another proposal [111] (as of this writing, only theoretical) has been to very briefly, but strongly, pulse the DC–SQUID and observe the produced ringdowns, which under the right conditions, will have the amplitude and (possibly) phase differ depending on the qubit state. This is somewhat analogous to what is presented in the experiment described here (although clearly in our case the flux differences are due to a global flux biasing as no qubit is actually present). Furthermore, the proposal outlined in [111], shows a full quantum treatment of the qubit and DC–SQUID system, but only considers an ultra short, much shorter than the inverse characteristic qubit frequency, DC pulse, whereas here, due to high temperature, the experiment has been considered to be classical and the pulses presented, time dependent.

Nevertheless, it is still useful to briefly explore just how the process of discrimination between two (or more) different flux states could be accomplished. First, one can expect that the total applied flux through the DC–SQUID, would consist of some biasing flux f_{bias} plus some source flux that is to be measured, say f_{source} (with both terms described in terms of ratios of flux quantum Φ_0). One could then imagine sending a pulse through the DC–SQUID, analogous to what was considered here, and recording the corresponding ringdown voltage. Some post processing of this ringdown signal, such as for example taking its root–mean–squared value, call it $V_{\rm rms}$, integrated over a well chosen time range, would provide a "signature" of the source flux. As long as these signatures of various values of $f_{\rm source}$ can be distinguished, one has an effective flux meter. For a given input pulse, assuming that $V_{\rm rms}$ is a well behaved function of f_s, a way to find the best $f_{\rm bias}$ over a range of flux where $V_{\rm rms}$ is monotonic (for example), could be simply to look for the largest slope of $V_{\rm rms}$ with respect to f_s, namely maximizing $\partial V_{\rm rms}(t_{\rm int}, f_s)/\partial f_s$ over all possible flux f_s between 0 and 0.5 (due to symmetry) and integration times $t_{\rm int}$. This would give the greatest contrast between the cases of $f_{\rm bias} + f_{\rm source}$ and $f_{\rm bias} - f_{\rm source}$. Fig. 4.12 shows an explicit example of this kind of flux discrimination, where we calculate the $V_{\rm rms}$ over a time range between 2.1 and 3.4 ns. The data that is being used corresponds to the input signal at $-20\,$dB amplitude, and is the same as in the flux–scans from Figs. 4.8(a) and (b). The dots represent results obtained from the experimental data, while the solid line is produced from the evolution calculated through simulations.

We can further make a crude calculation of the required sensitivity that one would need with the data from Fig. 4.12 to distinguish between two hypothetical flux qubit states. Setting the bias flux at $f_{\rm bias} \sim 0.36$ the slope is roughly $5\,{\rm mV}/\Phi_0$. If we assume a conservative noise temperature of 150 mK for a $\sim 3\,$GHz amplifier with a bandwidth of 100 MHz [31, 108], the rms voltage noise at the amplifier input would be $\sim 200\,$nV. If we take the $5\,{\rm mV}/\Phi_0$ slope for the signal at the output extracted from Fig. 4.12, and divide by the net gain of the HEMT amplifiers ($\sim 55\,$dB), this becomes $9\,\mu{\rm V}/\Phi_0$ at the DC–SQUID oscillator output. We consider a peak–to–peak qubit flux signal of $22\,{\rm m}\Phi_0$, which is reasonable, considering the back-action on the qubit would also likely be significantly less compared to a switching DC–SQUID measurement, since the DC–SQUID never enters the running state. This then corresponds to a SNR of ~ 1. So, we would be right at the threshold for reading out the ringdowns and distinguishing between the two qubit states in a single shot. We should further stress that one could likely do better by both using more sensitive amplifiers and optimizing various parameters. Of particular importance would be integration time $t_{\rm int}$, the pulse amplitude, as well as the quality factor of the DC–SQUID oscillator, all of which the $V_{\rm rms}$ curves are highly dependent on.

4.11 Summary and Conclusions

In conclusion, we have studied the transient behavior of a DC-SQUID operated as a nonlinear oscillator under pulsed AC radiation. We have reproduced experimental results obtained by Britton Plourde's group at Syracuse University. We theoretically applied signals of various amplitudes and biased the DC–SQUID with flux over the range of a single flux quantum, while observing the resulting voltage ringdowns. In order to account for the nonzero temperature of the experiment, we used the Johnson–Nyquist approach and modeled resistors as noisy current sources. This let us numerically reproduce the stochastic escape dynamics observed when the SQUID was driven with high–amplitude pulses. Finally, we briefly discussed the potential applicability of the system, and in particular the observed ringdown dynamics, to flux measurement. We found a good general agreement between the experimental data and results obtained through numerical simulations.

Chapter 5

Measurement Dynamics of a Qubit Coupled to a Harmonic Oscillator

In this chapter we study the quantum dynamics of a qubit coupled to a harmonic oscillator. While this kind of a system may be interesting in a variety of situations, we consider it in the context of a measurement. In particular, following [111, 116], a one that describes a superconducting system consisting of a flux qubit being measured by an inductively coupled DC–SQUID. We concentrate our discussion on a special case where the interaction between the qubit and the probe commutes with the free evolution of the qubit, and point out how in this regime the measurement can be thought of as quantum non–demolition (QND). We furthermore, calculate the effective dephasing rate of the qubit, which we relate to maximum rare at which the observer can learn about the qubit's state. By solving the corresponding master equation of our system we also explore the more complicated cases where the qubit–probe interaction no longer commutes with the free evolution of the qubit, and provide numerical evidence of the effective relaxation process associated with such a scenario. Finally, we conclude with a discussion that looks at how well, in some regimes of parameters, specific Kraus maps representing rotations and dephasing can mimic the often complicated evolution of the qubit.

We point out that the calculations shown in Sec. 5.6 were aided by Jay Gambetta.

5.1 Open Quantum Systems and the Lindblad Master Equation

We begin with a brief general discussion of open quantum systems, and in particular, introduce the Lindblad master equation, which will play an important role in modeling the process of a measurement presented throughout the rest of this chapter. We do not provide detailed mathematical derivations here, as they can be found in any text on open quantum systems — good examples are [14, 18]. Instead, we briefly show the final form of a Lindblad master equation, and discuss the various important assumptions that are needed in order to derive it.

In 1926 Schrödinger published a paper in which he introduced his famous equation, that has been been invaluable in explaining the quantum behavior of nature [109]. The Schrödinger's equation, written as

$$i\hbar\frac{\partial}{\partial t}|\Psi\rangle = H|\Psi\rangle, \tag{5.1}$$

with H the system's Hamiltonian and $|\Psi\rangle$ its state, dictates how a quantum system evolves in time[1]. We typically assume that it is valid in cases where the system in question is closed, meaning, it does not interact with the world outside of itself. This assumption is often not realistic when applied to real–world examples, but in some rare instances, where the interaction energy of the system with its environment is weak relative to the other energies involved, the effects of such an interaction may be small enough to be neglected completely. There are also other cases, where one needs to understand the effects of the environment on the main system (but not necessarily the evolution of the environment itself). These instances can be often described using master equations, which represent generalizations to the Schrödinger's original equation, which under certain conditions help us model open quantum systems.

Mathematically, we can imagine that the combined state of both the system we are interested in, as well as the environment that it couples to, can be described by a density matrix ρ_{tot}, which spans over the combined Hilbert spaces of both the system and environment, namely, $\rho_{\text{tot}} \in \mathcal{H}_{\text{sys}} \otimes \mathcal{H}_{\text{env}}$. Furthermore, let us assume that the combined Hamiltonian can be written as

$$H = H_{\text{sys}} + H_{\text{env}} + H_{\text{int}}, \tag{5.2}$$

with H_{sys}, H_{env} and H_{int} the Hamiltonians of the system, environment, and their interaction respectively. We could write the Schrödinger's equation for this system (here in terms of the density matrix[2]) as

$$\dot{\rho}_{\text{tot}} = -\frac{i}{\hbar}[H_{\text{sys}} + H_{\text{env}} + H_{\text{int}}, \rho_{\text{tot}}], \tag{5.3}$$

---

[1] We stress that the Schrödinger equation is not the only way to understand the evolution of quantum systems. Feynman's path integral approach [41] or Heisenberg's matrix mechanics [60] provide other ways.

[2] The Schrödinger equation written in this form is often called the Liouville–von Neumann equation.

and, in principle at least, solve it. Then by tracing out the degrees of freedom of the Hilbert space $\mathcal{H}_{\text{env}}$, obtain the solution for the evolution of the system's density matrix $\rho_{\text{sys}}(t) = \text{Tr}_{\text{env}}(\rho_{\text{tot}}(t))$ at any time of interest t. Of course this is usually not practical. We regard the environment as "big", with typically many more degrees of freedom as the system, but also, as we have already outlined, we may have not actually be interested in the dynamics of the environment, only its effects on the evolution of the system.

Hence, there are methods of reducing Eq. 5.3 to a differential equation for only $\rho_{\text{sys}}(t)$, which includes the environmental effects. We point the reader to references [18] or [14] for the details, and here only list the central assumptions in the derivation:

1. **Separable Initial State**
   This assumption implies that there are no correlations between the initial states of the environment and the system. Mathematically, we can express this condition as
   $$\rho_{\text{tot}}(0) = \rho_{\text{sys}}(0) \otimes \rho_{\text{env}}(0). \tag{5.4}$$
2. **Born Approximation**
   We implicitly assume that the coupling between the system and environment is "weak" and that the environment is "big"[3]. Here, these conditions imply that the environment does not change during the evolution[4], and therefore (due to Assumption 1, above) the environment and the system remain separable for all time.
3. **Markov Approximation**
   Markov approximation assumes that the environment is (effectively) memoryless, or more precisely, that the time scale for the decay of its correlations, is much shorter than the time scale of the system's dynamics.

Following the mathematics in the references, along with the assumptions above, one can arrive the following general form of a Lindblad master equation[5]

$$\dot{\rho}_{\text{sys}}(t) = -\frac{i}{\hbar}[H_{\text{sys}}, \rho_{\text{sys}}(t)] + \sum_k d_k \mathcal{D}[A_k]\rho_{\text{sys}}(t), \tag{5.5}$$

---

[3] For the mathematical definitions of "weak" and "big" in the context of this assumption, we point the reader to, for example, [18]

[4] Meaning its density matrix remains constant.

[5] The form of Eq. 5.5 is not the only way to model the evolution of the reduced system. Another widely employed method is to use the Bloch–Redfield master equation [8, 106].

with

$$\mathcal{D}[A_k]\rho_{\mathrm{sys}}(t) = A_k\rho_{\mathrm{sys}}A_k^\dagger + \frac{1}{2}\left(A_k^\dagger A_k\rho_{\mathrm{sys}}(t) + \rho_{\mathrm{sys}}(t)A_k^\dagger A_k\right), \tag{5.6}$$

The left hand side, and the first term on the right hand side of Eq. 5.5 clearly correspond to the unitary evolution due to the Hamiltonian of the system H_{sys}. The other terms, characterized by the sum, correspond to the effects that the environment has on the system. The operators A_k are often called Lindblad operators, and their form depends on both how one models the environment, as well as on the type of system–environment coupling that is present (namely the form of H_{int}).

Two important examples that will play a role in the following discussion, are a qubit that through the interaction with its environment undergoes pure dephasing at a rate Γ, and a harmonic oscillator that decays to its environment at a rate κ. The full master equations for such systems can be written as

$$\dot{\rho}_{\mathrm{q}}(t) = -\frac{i}{\hbar}[H_{\mathrm{q}}, \rho_{\mathrm{q}}(t)] + \Gamma\mathcal{D}[\sigma_z]\rho_{\mathrm{q}}(t), \tag{5.7}$$

and

$$\dot{\rho}_{\mathrm{osc}}(t) = -\frac{i}{\hbar}[H_{\mathrm{osc}}, \rho_{\mathrm{osc}}(t)] + \kappa\mathcal{D}[a]\rho_{\mathrm{osc}}(t), \tag{5.8}$$

respectively. Hence the corresponding Lindblad operators associated with these processes are σ_z and a, with appropriate prefactors Γ and κ respectively [14], and with a representing a lowering operator.

5.2 Quantum Measurement

In this section we introduce the concept of measurement in quantum mechanics. As was the case in Sec. 5.1, this is a very involved topic with many detailed resources widely available. We will only touch on a few key points that are central to the following discussion. For a much more complete presentation we point the reader to references such as [12, 63, 96] or [129].

The quantum measurement postulate is arguably the most interesting of the quantum postulates [96]. It states that quantum measurements can be described in terms of a collection of operators M_m which act on the system being measured, that we can describe in terms of a state $|\Psi\rangle$. The index m corresponds to the outcome of the measurement, with the corresponding probability of observing m, being

$$p(m) = \langle\Psi|M_m^\dagger M_m|\Psi\rangle. \tag{5.9}$$

The state of the system right after the measurement resulting in m is expected to be

$$\frac{M_m|\Psi\rangle}{\sqrt{p(m)}}. \tag{5.10}$$

Finally, due to the fact that the sum of the probabilities of the individual outcomes m must sum to 1 (since we always expect some outcome), we have a completeness relation on the measurement operators M_m that reads

$$\sum_m M_m^\dagger M_m = \mathbb{1}. \tag{5.11}$$

This postulate, as presented here, is clearly very general. A special class of measurements that is often considered, consists of what are called *projective measurements* or alternatively *von Neuman measurements*. A projective measurement can be described by an observable M, a Hermitian operator, which has a spectral decomposition

$$M = \sum_m m P_m, \tag{5.12}$$

with P_m being a projector onto the eigenspace of M, and m the corresponding eigenvalue. The projectors P_m can be associated with M_m from Eqs. 5.9 and 5.10, by simply insisting that each M_m is a Hermitian operator, and that $M_m M_{m'} = M_m \delta_{m,m'}$. It then follows that in a case of projective measurements the probability of outcome m is simply

$$p_{\text{proj}}(m) = \langle\Psi|P_m|\Psi\rangle, \tag{5.13}$$

and the state right after the measurement

$$\frac{P_m|\Psi\rangle}{\sqrt{p_{\text{proj}}(m)}}. \tag{5.14}$$

Let us consider an example of a projective measurement on a single qubit. We assume that the qubit is in some arbitrary state $|\Psi\rangle = \alpha|0\rangle + \beta|1\rangle$ with $|\alpha|^2 + |\beta|^2 = 1$. We then imagine measuring the qubit's orientation along the z–axis[6], which corresponds to the observable σ_z. The relevant projective operators are then $P_0 = |0\rangle\langle 0|$ and $P_1 = |1\rangle\langle 1|$, with eigenvalue of $+1$ and -1 respectively. The outcomes of such a measurement can be easily shown to be $+1$ with the of $|\alpha|^2$ and -1 with the probability of $|\beta|^2$. We could rewrite this process in terms of the

---

[6] There is no loss of generality here, since if the observable we wish to measure is along a different axis, we can simply relabel those axis as the z–axis.

qubit's density matrix and obtain

$$\rho_{\mathrm{sys}} = |\Psi\rangle\langle\Psi| = \begin{bmatrix} |\alpha|^2 & \alpha\beta^* \\ \alpha^*\beta & |\beta|^2 \end{bmatrix} \xrightarrow{\text{measure } \sigma_z} \begin{bmatrix} |\alpha|^2 & 0 \\ 0 & |\beta|^2 \end{bmatrix}. \tag{5.15}$$

Hence the projective measurement process has eliminated the off–diagonal components of the density matrix and turned it into a classical mixture. This kind of a process can be described as a *dephasing map*[7], as it gets rid of the relative phase between the $|0\rangle$ and $|1\rangle$.

A direct projective measurement is generally thought of as an idealization — it tells us what happens to the quantum object being measured, but does not shed much light on how the measuring device should operate in order to achieve a given measurement [12]. In practice, it is often more realistic to model the measurement process of a quantum system (a qubit in our case), by considering a scenario where it couples to a detector (which we may alternatively call *meter* or *probe*) — such a measurement is called *indirect.* The interaction between the probe and the qubit can build up correlations between their respective states, and hence by observing only the state of the detector, one effectively measures the qubit. Of course one could ask the question of why stop at modeling the detector? There could be other systems at play in getting the information to the observer — maybe the detector's state has to be interpreted or processed by a computer, which in turn has to display the information on a screen for the observer to see, and so on. Such a chain of events is called a von Neumann chain. The postulate of quantum mechanics, however, states that at some point, before the measurement result reaches the mind of the observer, one has to break this chain and apply the projective postulate. This is regarded as the Heisenberg's cut. The key reason why it often makes sense to model the detector along with the qubit, and apply the projective postulate to the detector and not the qubit being measured, is that detectors are typically treated as macroscopic objects with decoherence rates much larger than those of the system itself. For a much more detailed discussion on this topic, we point the reader to reference [129].

Finally, let us outline the concept of a quantum non–demolition (QND) measurement. QND measurements are a special class of quantum measurements, that satisfy the following conditions [12]

1. **No precision limit**
   There is no fundamental constraint on the precision of the measurement.
2. **No perturbation necessary**
   There need not be any perturbation to the quantity being measured.

---

[7] We will discuss dephasing maps in much more detail in Sec. 5.11.

3. **Standard perturbation to conjugate quantity**
   The quantity that is conjugate to the measured observable is perturbed in accordance with the uncertainty principle.

These kinds of measurements are useful as they are usually considered least disturbing to the system being measured.

A sufficient criteria that one can use to determine if a measurement is QND, is to check if the measurement observable, say q, commutes with the Hamiltonian of the system H, namely if

$$[H, q] = 0. \tag{5.16}$$

Such a criteria is sufficient, but in fact not necessary. A weaker (but harder to work with) criteria is that the observable q commutes with unitary evolution operator U, which generates the combined evolution of the object being measured as well as the probe — for a detailed discussion of this topic, we point the reader to [12].

Let us mention a crude example that will be useful in the following sections. If we choose the measurement process of a qubit, where the observable is $q = \sigma_z$ and the full system's Hamiltonian $H = \sigma_z \otimes A_{\rm probe}$, with $A_{\rm probe}$ some operator acting on the Hilbert space of the probe. Such a measurement, by Eq. 5.16, is clearly QND. On the other hand, if we were to choose $H = \sigma_x \otimes A_{\rm probe}$ instead, the criteria shown in Eq. 5.16 would not be satisfied. We note however, that if we were to choose the measurement time to be very short (but yet the measurement strong enough to fully dephase the qubit), much shorter than the time scale associated with the evolution of the qubit due to H, one might still end up with an approximately QND measurement — see for example [110].

5.3 System Hamiltonian and the Corresponding Superconducting Circuit

We are now ready to discuss the particular measurement process that we study throughout the rest of this chapter, in more detail. The system that we consider, consist of a qubit coupled to a probe (detector) which we model as a harmonic oscillator. While in the general setting one might envision both the qubit as well as the probe interacting with their own environments, here we assume that the coupling of the qubit to its environment (and hence the effect of that coupling) is substantially less dominant than all the other energies in the system. This allows us to mainly concentrate on the dynamics of the qubit due to only the measurement process mediated through the coupling to the detector. A schematic representation of this scenario is shown in Fig. 5.1(a). The measurement process consists of preparing a qubit in some state, and simply interacting the probe with the qubit for some time. If the interaction time is long enough, or alternatively the qubit–probe coupling strong enough, we expect the qubit to be fully dephased by the interaction (i.e., its density matrix reduced to a classical mixture), mimicking the behavior of the process shown in Eq. 5.15. Furthermore, due to this interaction, the information about the state of the qubit gets imprinted in the degrees of freedom of the oscillator, which can be then extracted by the observer (by for example studying the momentum observable of the probe). Of particular interest to us, is to understand how quickly the dephasing process of the qubit occurs, relative to the times associated with the free evolution of the qubit or probe.

Throughout most of this Chapter we consider a particular Hamiltonian that could in principle describe many different physical systems, but it is worth describing at least one specific physical implementation. Therefore, as an example of a physical system that can model the process just outlined, we consider a flux qubit coupled to a symmetric DC–SQUID, which plays the role of the probe. A diagram that shows this setup is presented in Fig. 5.1(b). The qubit shown here, has an optional “extra” junction (shown in blue), which forms a secondary, smaller loop — such a variation of a flux qubit provides another means of control, and allows for a tunable tunneling energy [97]. Assuming that the geometric inductance of the smaller loop, can be neglected, the coupling between the flux qubit and the DC–SQUID is mediated by the mutual inductance[8], labeled M, while the environmental degrees of freedom that the DC–SQUID interacts with are represented by a general impedance Z_0. This very setup has already been briefly discussed in Chapter 4, Sec. 4.10, but for a more detailed analysis we point the reader to [110, 111, 116]. As in Chapter 4, in the limit of small geometric inductance, and with a large shunting capacitor C_t, the DC–SQUID can be treated as a single degree of freedom oscillator, with the minimum of its potential energy dependent on the total flux threaded through the DC–SQUID as well as the biasing current I_b. As we have already discussed in Chapter 2, the flux of through the DC–SQUID depends on the state of the qubit[9]. Furthermore, it was shown in [110, 116], that in the lowest order approximation, where the DC–SQUID is treated as a simple harmonic oscillator, the qubit and the DC–SQUID only couple when the biasing current I_b, is close to the effective critical current of the DC–SQUID. This, therefore, gives us a physical means of controlling the measurement process (more specifically, the measurement time and strength) on–demand by simply turning the biasing current I_b on and off. In contrast to the discussion in Chapter 4, here we assume that the

---

[8] Here, in order for the Hamiltonian derivation from [110, 116] to hold, we assume that the geometric inductance of the larger qubit loop is substantially greater than the inductance of the smaller loop. The goal of discussing this scenario is only to provide a physical justification for a limit where tunneling element Δ in the qubit's Hamiltonian could be taken arbitrarily close to zero.

[9] This is because the qubit's different computational states correspond to the currents circulating around the qubit loop in different direction — these currents can be written as $\pm I_p$. This in turn results in the contribution of the qubit's flux through the DC–SQUID being $\pm M I_p$.

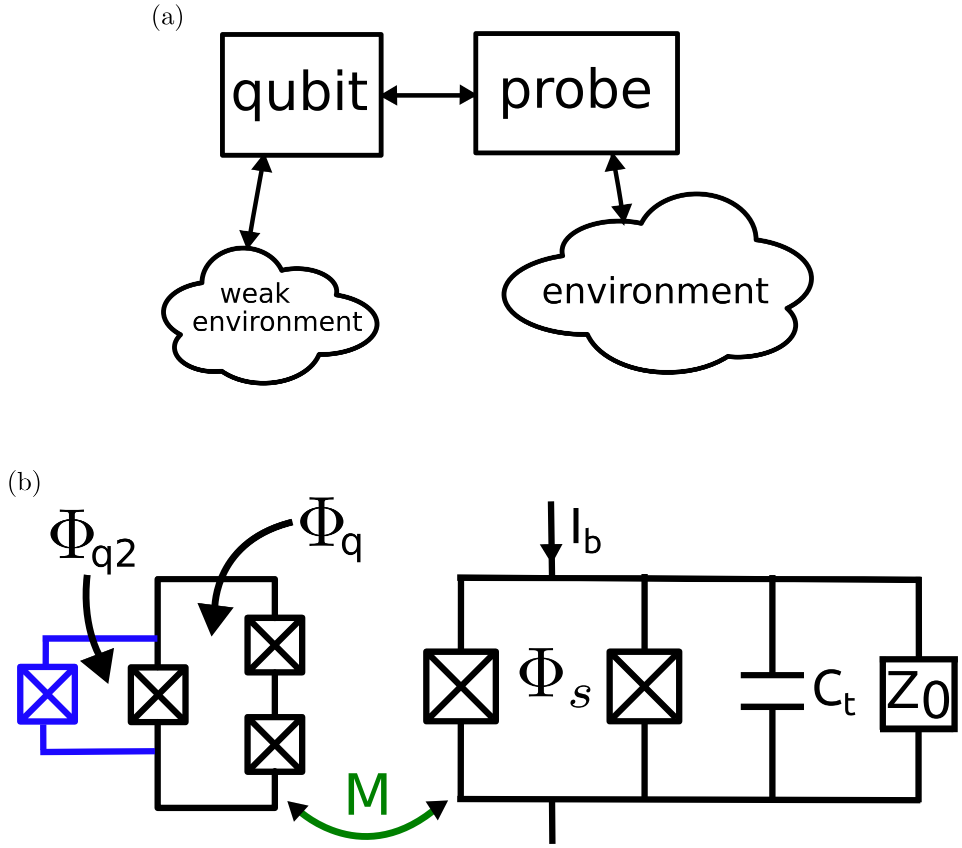

Figure 5.1: (a) A schematic showing a qubit coupled to a measuring probe, along with their respective environments. It is assumed that strength of the interaction of the qubit and its environment is weak when compared to the other energy scales in the problem. (b) An example system that could be used to implement a setup from (a), consisting of a flux qubit coupled to a DC–SQUID which is shunted by a large capacitance C_t. The qubit presented here has an optional "extra" junction (shown in blue), which forms a secondary, smaller loop — such a variation of a flux qubit provides another means of control, and allows for a tunneling gap energy [97]. Assuming that the geometric inductance of the smaller loop, can be neglected, the key means of interaction between the qubit and DC–SQUID is the mutual inductance, labeled M. The qubit as well as the DC–SQUID can be individually threaded with fluxes Φ_q, Φ_{q2} as well as Φ_s respectively. Furthermore, the coupling between the qubit and the DC–SQUID can be controlled by a biasing current I_b. Z_0 in the diagram represents the effective environment that the DC–SQUID is coupled to. We assume that the qubit's interaction with its own environment is weak and therefore neglect its effects.

biasing current, when turned on, is not oscillating but constant.

Following [110, 111, 116], we can write down the Hamiltonian of the full circuit shown in Fig. 5.1(b) as

$$H = H_q + H_{\text{osc}} + H_{\text{q−osc}} + H_{\text{env}} + H_{\text{osc−env}} \tag{5.17}$$

with

$$H_q = \frac{\hbar\epsilon}{2}\sigma_z + \frac{\hbar\Delta}{2}\sigma_x, \qquad H_{\text{osc}} = \hbar\Omega a^\dagger a, \qquad H_{\text{q−osc}} = \hbar\gamma\sigma_z(a^\dagger + a), \tag{5.18}$$

where ϵ is the qubit energy, Δ its tunneling element, Ω the frequency of the oscillator and γ the qubit–oscillator coupling strength. As we already noted, we assume that γ has a form of a square pulse, but we will concentrate on the evolution of the system when it is finite[10]. $a^\dagger$ and a represent the raising and lowering operators acting on the Hilbert space of the probe. As in [111], we treat the environment of the DC–SQUID as a bath of harmonic oscillators [17] with Ohmic spectral density, which, following the discussion in Sec. 5.1, leads to the effective master equation

$$\dot{\rho}_{\text{sys}}(t) = -\frac{i}{\hbar}[H_q + H_{\text{osc}} + H_{\text{q−osc}}, \rho_{\text{sys}}(t)] + \kappa\mathcal{D}[a]\rho_{\text{sys}}(t), \tag{5.19}$$

where we assume that $\rho_{\text{sys}} \in \mathcal{H}_q \otimes \mathcal{H}_{\text{osc}}$, and κ to represent photon loss in the DC–SQUID. By solving this master equation, we can fully characterize the time evolution of our system and in particular the qubit as it undergoes measurement.

5.4 Qubit Measurement Dynamics

Our main goal is to understand how the qubit evolves, as the measurement process takes place. This can be done in principle by solving the full master equation shown in Eq. 5.19 and tracing out the degrees of freedom of the probe. There are two key drawbacks to this approach however. The first consists of the fact that if we are interested in understanding the qubit's evolution, solving the full Eq. 5.19 comes with a substantial computational overhead. In some regimes of parameters, the Hilbert space of the probe may be highly occupied, which would mean that many energy levels have to be considered in order to obtain an accurate evolution, and that can result in long computation times. The second, perhaps an even bigger limitation, is that it may not be easy to gain intuition about the qubit's dynamics from the results, unless they are repeated for various parameter configurations. In particular, since the probe decays at a rate κ, we might guess that the qubit will

---

[10] For the relationship between these parameters and physical circuit parameters, we point the reader to [111].

dephase at a rate dependent on κ, but at this stage, the functional dependence of such a rate on κ and the other Hamiltonian parameters in unclear.

Hence our goal in the next section will be to simplify the master equation shown in Eq. 5.19 to one that only encompasses the degrees of freedom of the qubit. The key result will be a derivation of a measurement induced dephasing rate Γ_d as well as a brief mention of an effective relaxation rate. We will distinguish between important regimes of parameters that lead to the measurement being either QND, approximately QND, or non–QND.

The numerical solutions to the master equations presented throughout the rest of this chapter are obtained using either an open source python solver called QUTIP [66], or in the case of the plots shown in Fig. 5.5, using an in–house solver written mostly by Jay Gambetta.

5.5 Polaron–type transformation

In order calculate the effective master equation for the evolution of the qubit, we will take advantage of a polaron–type transformation. It has recently been shown to be very useful in many studies [9, 46, 112]. The mathematical treatment presented here, will closely follow discussions found in [9, 46], with the key difference being the type of Hamiltonians that are considered. In those publications, the qubit interaction is dispersive, and the qubit mainly couples to photon number operator $a^\dagger a$, whereas in our case it couples to the oscillator's displacement $a^\dagger + a$.

The key idea of a polaron transformation is to go into a frame in which it the oscillator stays in its ground state. For example if we we consider a simple harmonic oscillator that is in a time–dependent coherent state $|\Psi\rangle = |\alpha(t)\rangle$, we can imagine applying a unitary transformation $U = D(-\alpha(t))$, where $D(\alpha) = \exp(\alpha a^\dagger - \alpha^* a)$ is the standard displacement operator, to the state $|\Psi\rangle$. In is then clear that $U|\Psi\rangle = |0\rangle$, and the oscillator in a frame defined by U will remain in its ground state.

In the case of an oscillator coupled to a qubit, we consider a polaron–type transformation that depends on the state that the qubit is in. In particular we define

$$\mathbf{P} = D(\alpha_e)|e\rangle\langle e| + D(\alpha_g)|g\rangle\langle g|, \tag{5.20}$$

where $|j\rangle\langle j|$, with $j \in \{e, g\}$, representing the projective operators on the qubit's excited and ground states, and α_j being complex numbers. In the next section we apply this transformation to the full master equation shown in Eq. 5.19.

5.6 Measurement Induced Dephasing Rate[11] in the Regime Where $\Delta = 0$

We start with a special case, where we define the measurement process to be QND, by the definition presented in Eq. 5.16. We accomplish this by setting $\Delta = 0$ in the full system Hamiltonian $H = H_q + H_{\text{osc}} + H_{\text{q−osc}}$ defined in Eq. 5.18. Furthermore, in Appendix F we explicitly show that in this special case, the evolution of the probe can be described in terms of coherent states $|\alpha_e(t)\rangle$ and $|\alpha_g(t)\rangle$, with $\alpha_e(t)$ and $\alpha_g(t)$, time–dependent complex numbers that correspond to the qubit being in either excited or ground state respectively (we will shortly drop the explicit time dependence for brevity). In particular we have

$$\alpha_j(t) =\alpha_j^s + \left(\alpha_j(0) - \alpha_j^s\right) \exp\left(-i\left(\Omega + \gamma\right) t - \frac{\kappa t}{2}\right) \tag{5.21}$$

for $j \in \{e, g\}$, with α_j^s representing steady state solutions $\alpha_e^s = -\frac{2i\gamma}{2i\Omega+\kappa}$ and $\alpha_g^s = -\alpha_e^s$.

Hence we start by transforming the full density matrix ϱ into the polaron frame, which gives

$$\varrho^{\mathbf{P}} = \mathbf{P}^\dagger \varrho \mathbf{P}. \tag{5.22}$$

Next, we rewrite the master equation in this new frame as

$$\begin{aligned}\dot{\varrho}^{\mathbf{P}} =& -\frac{i}{\hbar}[H^{\mathbf{P}}, \varrho^{\mathbf{P}}] + \kappa\mathcal{D}[a^{\mathbf{P}}]\varrho^{\mathbf{P}} \\ &- \mathbf{P}^\dagger\dot{\mathbf{P}}\varrho^{\mathbf{P}} - \varrho^{\mathbf{P}}\dot{\mathbf{P}}^\dagger\mathbf{P},\end{aligned} \tag{5.23}$$

with $H^{\mathbf{P}} = \mathbf{P}^\dagger H\mathbf{P}$ and $a^{\mathbf{P}} = \mathbf{P}^\dagger a\mathbf{P}$. In order to aid further calculations, we define an operator

$$\Pi_\alpha = \alpha_g|g\rangle\langle g| + \alpha_e|e\rangle\langle e|, \tag{5.24}$$

that lets us write

$$a^{\mathbf{P}} = a + \Pi_\alpha \tag{5.25}$$

$$(a^\dagger)^{\mathbf{P}} = a^\dagger + \Pi_\alpha^* \tag{5.26}$$

$$(a^\dagger a)^{\mathbf{P}} = a^\dagger a + a\Pi_\alpha^* + a^\dagger\Pi_\alpha + |\Pi_\alpha|^2 \tag{5.27}$$

$$(a^\dagger + a)^{\mathbf{P}} = a^\dagger + a + \Pi_{\text{Re}\alpha} \tag{5.28}$$

Using these expressions and the fact that $\sigma_z^{\mathbf{P}} = \sigma_z$, the transformed Hamiltonian

---

[11] Calculations in this section were aided by Jay Gambetta.

can be written as

$$\begin{aligned} H^{\mathbf{P}} = {}& \hbar\Omega \left(a^{\dagger} a + a^{\dagger} \Pi_{\alpha} + a \Pi_{\alpha}^{*} + |\alpha_g|^2 |g\rangle\langle g| + |\alpha_e|^2 |e\rangle\langle e| \right) \\ & + \frac{\hbar\epsilon}{2}\sigma_z + \hbar\gamma \left(a^{\dagger} + a + \Pi_{\alpha} + \Pi_{\alpha}^{*} \right) \sigma_z . \end{aligned} \tag{5.29}$$

Next, noting that

$$\frac{d}{dt} D(\alpha(t)) = \left(\left(\dot{\alpha}(t) a^{\dagger} - \dot{\alpha}(t)^{*} a \right) + \frac{1}{2} \left(\alpha(t) \dot{\alpha}(t)^{*} - \alpha(t)^{*} \dot{\alpha}(t) \right) \right) D(\alpha(t)) \tag{5.30}$$

we can write

$$\begin{aligned} -\mathbf{P}^{\dagger} \dot{\mathbf{P}} \varrho^{\mathbf{P}} - \varrho^{\mathbf{P}} \dot{\mathbf{P}}^{\dagger} \mathbf{P} = & - \left[\dot{\Pi}_{\alpha} a^{\dagger} - \dot{\Pi}_{\alpha}^{*} a, \varrho^{\mathbf{P}} \right] \\ & - i \left[\mathrm{Im}(\dot{\alpha}_e \alpha_e^{*}) |e\rangle\langle e| + \mathrm{Im}(\dot{\alpha}_g \alpha_g^{*}) |g\rangle\langle g|, \varrho^{\mathbf{P}} \right] . \end{aligned} \tag{5.31}$$

Finally, with the help of Eqs 5.25–5.28, we can also calculate the transformed version of the Lindblad term, which reads

$$\begin{aligned} \mathcal{D}[a^{\mathbf{P}}] \varrho^{\mathbf{P}} = {}& \mathcal{D}[a] \varrho^{\mathbf{P}} - \frac{1}{2} [a^{\dagger} \Pi_{\alpha} - a \Pi_{\alpha}^{*}, \varrho^{\mathbf{P}}] + \frac{|\beta|^2}{4} \mathcal{D}[\sigma_z] \varrho^{\mathbf{P}} \\ & + \frac{\beta^{*}}{2} a [\varrho^{\mathbf{P}}, \sigma_z] + \frac{\beta}{2} [\sigma_z, \varrho^{\mathbf{P}}] a^{\dagger} - i \frac{\mathrm{Im}[\alpha_g \alpha_e^{*}]}{2} [\sigma_z, \varrho^{\mathbf{P}}], \end{aligned} \tag{5.32}$$

where for convenience we have defined $\beta = \alpha_e - \alpha_g$. Finally, using Eqs 5.29, 5.31, 5.32 and simplifying, we can rewrite 5.23 as

$$\begin{aligned} \dot{\varrho}^{\mathbf{P}} = & - i\Omega \left[a^{\dagger} a, \varrho^{\mathbf{P}} \right] - i \frac{\epsilon}{2} \left[\sigma_z, \varrho^{\mathbf{P}} \right] - i \frac{\gamma}{2} \left[\left(\Pi_{\alpha} + \Pi_{\alpha}^{*} \right) \sigma_z, \varrho^{\mathbf{P}} \right] \\ & + \kappa \mathcal{D}[a] \varrho^{\mathbf{P}} + \frac{\kappa |\beta|^2}{4} \mathcal{D}[\sigma_z] \varrho^{\mathbf{P}} + \frac{\kappa \beta^{*}}{2} a \left[\varrho^{\mathbf{P}}, \sigma_z \right] + \frac{\kappa\beta}{2} \left[\sigma_z, \varrho^{\mathbf{P}} \right] a^{\dagger} \\ & - i \frac{\kappa \mathrm{Im}[\alpha_g \alpha_e^{*}]}{2} \left[\sigma_z, \varrho^{\mathbf{P}} \right] . \end{aligned} \tag{5.33}$$

This equation, while complicated, gives us the full evolution of our system in the polaron frame. It is worth stressing that the raising (lowering) operator always acts on the density matrix from the right (left), hence if the oscillator starts its evolution in the ground state, it will continue in the ground state — this is precisely the reason why the polaron transformation is useful here.

Ultimately we are interested in the evolution of the qubit, in an untransformed, lab frame. We can therefore write

$$\rho^{q} = \mathrm{Tr}_{\mathrm{osc}}[\mathbf{P} \varrho^{\mathbf{P}} \mathbf{P}^{\dagger}], \tag{5.34}$$

with ρ^{q} representing the lab frame density matrix of the qubit only. Since we expect the oscillator to stay in its ground state, we rewrite $\varrho^{\mathbf{P}}$ as[12]

$$\varrho^{\mathbf{P}} = \sum_{i,j=e,g} \varrho^{\mathbf{P}}_{i,j} |i\rangle\langle j| \otimes |0\rangle\langle 0|. \tag{5.35}$$

Then substituting Eq. 5.35 into 5.34 leads to

$$\begin{aligned}
\dot{\rho}_q =& \frac{d}{dt} \mathrm{Tr}_{\mathrm{osc}}[\mathbf{P}\varrho^{\mathbf{P}}\mathbf{P}^{\dagger}] \\
=& \frac{d}{dt}\left(\sum_{i,j} \varrho^{\mathbf{P}}_{ij} \langle 0|D^{\dagger}(\alpha_j)D(\alpha_i)|0\rangle\right) \\
=& e^{-i\theta}\langle 0|D(\beta_{ij})|0\rangle \left(\dot{\varrho}^{\mathbf{P}}_{ij} - i\dot{\theta}\varrho^{\mathbf{P}}_{ij} - \frac{1}{2}\varrho^{\mathbf{P}}_{ij}\frac{d}{dt}|\beta_{ij}|^2\right),
\end{aligned} \tag{5.36}$$

where we have taken $\beta_{ij} = \alpha_i - \alpha_j$ and $\theta_{ij} = \mathrm{Im}(\alpha_j \alpha_i^*)$. To obtain the last line, we used the fact that

$$\langle 0|D^{\dagger}(\alpha_j)D(\alpha_i)|0\rangle = e^{-i\theta_{ij}}\langle 0|D(\beta_{ij})|0\rangle \tag{5.37}$$

and

$$\frac{d}{dt}\langle 0|D(\beta_{ij})|0\rangle = -\frac{1}{2}\langle 0|D(\beta_{ij})|0\rangle \frac{d}{dt}|\beta_{ij}|^2. \tag{5.38}$$

The $\dot{\varrho}^{\mathbf{P}}_{ij}$ in the last line of Eq. 5.36 can be rewritten in terms of $\varrho^{\mathbf{P}}_{ij}$ using Eq. 5.33, by noting that $\dot{\varrho}^{\mathbf{P}}_{ij} = \langle i,0|\dot{\varrho}^{\mathbf{P}}|j,0\rangle$ (we skip the details of this for brevity). rinally, noting from Eq. 5.34 and 5.35 that

$$\rho^q_{ij} = \langle i|\rho^q|j\rangle = e^{-i\theta}\langle 0|D(\beta_{ij})|0\rangle \varrho^{\mathbf{P}}_{ij}, \tag{5.39}$$

and rewriting all instances of α_e and α_g in terms of the parameters of the Hamiltonian using Eq. 5.21, we arrive at a set of four differential equations for each of ρ^q_{ij}. Rewriting them in a more accessible form, leads to a simple master equation for only the degrees of freedom of the qubit. It can be written as

$$\dot{\rho^q} = -i\frac{\epsilon}{2}[\sigma_z, \rho^q] + \frac{1}{2}\Gamma_d(\gamma, \Omega, \kappa, t)\mathcal{D}[\sigma_z]\rho^q, \tag{5.40}$$

---

[12] We could be more general here and instead choose to write $\varrho^{\mathbf{P}} = \sum_{n,m=0}^{\infty}\sum_{i,j=e,g} \varrho^{\mathbf{P}}_{n,m,i,j}|i\rangle\langle j| \otimes |n\rangle\langle m|$ and then explicitly show that the only relevant case is when $n = m = 0$. This is done in [9, 46] for the dispersive system that is used there.

with

$$\Gamma_d(\gamma, \Omega, \kappa, t) = \frac{8\gamma^2}{\kappa^2 + 4\Omega^2} \left(\kappa - e^{-\frac{t\kappa}{2}} \kappa \cos(\Omega t) + 2e^{-\frac{t\kappa}{2}} \Omega \sin(\Omega t) \right). \tag{5.41}$$

Eq. 5.40 tells us how the qubit evolves and how its evolution depends on the parameters associated with the full system — namely the probe frequency Ω, the coupling of the qubit to the probe γ, as well as the probe decay rate κ. Γ_d is the main result of this section, and can be defined as a measurement induced dephasing rate of the qubit. In the limit where $\Delta = 0$, which we have considered, it is exact, as no approximation have been made[13]. Furthermore, since no other decay channels of the qubit have been considered[14], Γ_d tells us the maximum rate at which information about the qubit's state can be transfered to the probe, and therefore the observer.

5.7 Qubit Dynamics Results with $\Delta = 0$

We can now explore how well the effective, reduced master equation we have just calculated describes the qubit's evolution. In order to do this, we can compare results obtained from solving it, to the results obtained from solving the full master equation shown in 5.19. We reiterate that even though, due to the time dependence of Γ_d, in general the Eq. 5.40 is not trivial to solve analytically, it is substantially easier to solve numerically over Eq. 5.19, which in some regimes of parameters (for example when $\gamma \gg \Omega$) could require many more computational resources.

Figure 5.2 shows plots of the expectation values of σ_x (in red), σ_y (in blue), σ_z (in green) and of the purity of the qubit's state (in black), defined as $\mathrm{Tr}((\rho^q)^2) = \frac{1}{2}\left(\mathbb{1} + \langle\sigma_x\rangle^2 + \langle\sigma_y\rangle^2 + \langle\sigma_z\rangle^2\right)$. The plot shown in (a) presents results of an initial qubit's state $|+_x\rangle = \frac{1}{\sqrt{2}}(|0\rangle + |1\rangle)$, whereas in (b) of a state $|+_y\rangle = \frac{1}{\sqrt{2}}(|0\rangle + i|1\rangle)$. In both cases the probe is assumed to be in its ground state at the start of the evolution. Each plot shows two sets of results, the first of the full master equation solution (solid lines), while the second of the reduced case (solid circle symbols). The particular set of parameters used were [15] $\Omega = 2\pi$, $\gamma = \Omega$, $\epsilon = \Omega/2$ and $\kappa = \Omega/20$.

As we would expect, the plots show excellent agreement between the reduced and full master equation solutions. This is because in the case where $\Delta = 0$,

---

[13] Beyond the approximations related to the fact that the master equation shown in 5.19 is a good representation of the true evolution of the system.

[14] As one could expect, including a for example pure dephasing channel into the qubit's own environment via a Lindblad operator $\Gamma_{\mathrm{q-deph}}\mathcal{D}[\sigma_z]\rho_{\mathrm{sys}}$ in Eq. 5.19, would lead to the same term being added to Eq. 5.40, acting on ρ^q instead of ρ_{sys}.

[15] The numerical values of the various parameters are written in terms of Ω, and Ω is chosen so that its period is 1 — these of course could be trivially scaled to more realistic values one would see in an experiment.

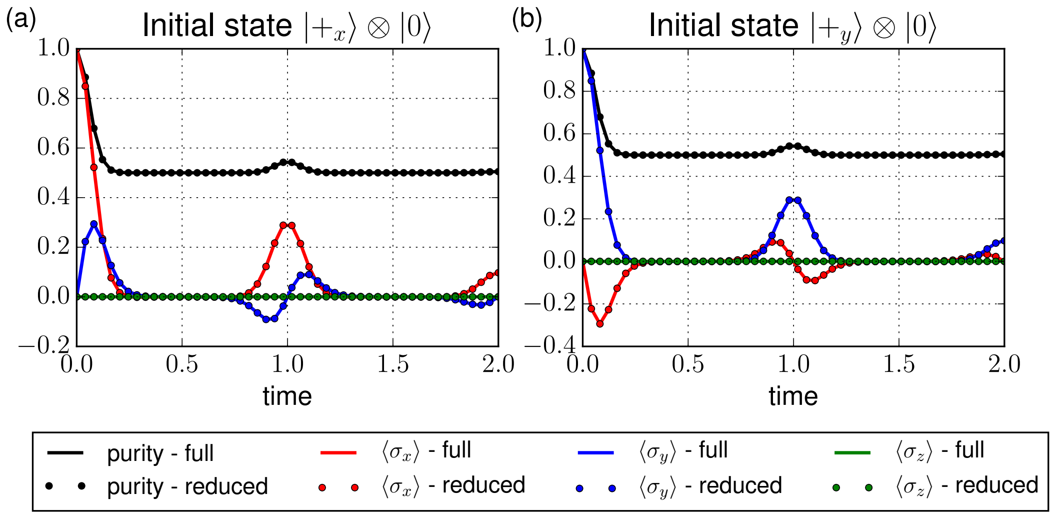

Figure 5.2: Evolution of the qubit in the limit where $\Delta = 0$. The plots show the expectation values of σ_x (in red), σ_y (in blue), σ_z (in green) as well as purity (in black). (a) presents results with an initial qubit state $|+_x\rangle = \frac{1}{\sqrt{2}}(|0\rangle + |1\rangle)$, whereas (b) the state $|+_y\rangle = \frac{1}{\sqrt{2}}(|0\rangle + i|1\rangle)$. In both cases the probe is assumed to be in its ground state at the start of the evolution. Solid (circle symbol) curves show the evolution obtained by solving the full (reduced) master equation. The other parameters used are set at $\Omega = 2\pi$, $\gamma = \Omega$, $\epsilon = \Omega/2$ and $\kappa = \Omega/20$.

Eq. 5.40 is an exact representation of the qubit's dynamics. From both of the plots we observe that as the qubit evolves, it is being dephased. This can be seen from the purity curves, but also by noting that as time advances, both $\langle\sigma_x\rangle$ as well as $\langle\sigma_y\rangle$ tend to get closer to zero. For the set of parameters we have chosen, we observe that shortly after the evolution starts, the qubit's purity goes down a value of $\frac{1}{2}$, which implies the qubit is in a perfectly mixed state, but later on, near the time that is a multiple of $2\pi/\Omega$, it jumps up again, although to a lower value than at the time $2\pi/\Omega$ earlier. The qubit gains back some of its coherent information at the cost it being temporarily "erased" from the probe — i.e. at this point in time, just by looking at the state of the probe, one cannot distinguish what state the qubit is in[16]. The reason why the purity is lower with every consecutive period of the oscillator, is that the state of the oscillator decays to its environment at a rate κ.

5.8 Qubit Dynamics Results with $\Delta \neq 0$, Large κ

Let us now allow Δ to be finite, but consider a special case where κ is large relative to all the other energies of the system. In such a situation, a (slightly modified)

---

[16] Since we do not explicitly study the evolution of the probe here, we do not show this, but this effect is discussed in [110].

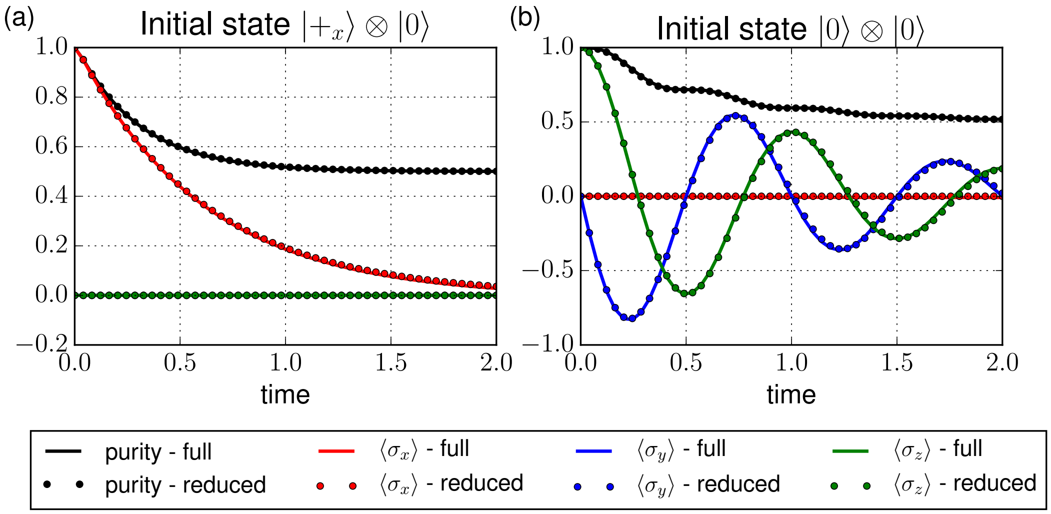

Figure 5.3: Evolution of the qubit with $\Delta = 2\pi$ and $\kappa = 30\Delta$. The plots show the expectation values of σ_x (in red), σ_y (in blue), σ_z (in green) as well as purity (in black). (a) presents results with an initial qubit state $|+_x\rangle = \frac{1}{\sqrt{2}}(|0\rangle + |1\rangle)$, whereas (b) the state $|0\rangle$. In both cases the probe is assumed to be in its ground state at the start of the evolution. Solid (circle symbol) curves show the evolution obtained by solving the full (reduced) master equation. The other parameters used are set at $\Omega = 2\pi$, $\gamma = \Omega$ and $\epsilon = 0$.

reduced master equation from Eq. 5.40 still provides a very good description of the evolution of the qubit. In general, when $\Delta \neq 0$, the coherent states that we have calculated in Appendex F are no longer a good description of the evolution of the degrees of freedom of the oscillator — and therefore the polaron transformation is not useful, since in the polaron frame, an oscillator that starts in a ground state, will not stay stay there as the time evolves. In [46] however, it has been shown that in the limit of $\beta \ll 1$, which in our case can be accomplished with a large κ, up to the lowest order in β, the correction of a finite Δ to Eq. 5.40 is simply $-i\frac{\Delta}{2}[\sigma_x, \rho^q]$. This case of small β, effectively means that the coherent states of the oscillator α_e and α_g do not have the time to separate during the system's evolution. Or put another way, the state inside the oscillator decays out to the environment before it has a chance to evolve.

In Fig. 5.3 we present the time–dependent expectation values of the qubit Pauli operators as well as the purity of the density states. In Fig. 5.3(a) we look at an initial state of $|+_x\rangle$ as before, but in plot (b) we show the case of the initial state $|0\rangle$. This is particularly interesting as in this regime, the combination of finite Δ as well as a large κ also leads to decay of $\langle\sigma_z\rangle$. The numerical values of all the parameters are taken as $\Omega = 2\pi$, $\Delta = \Omega$, $\gamma = \Omega$, $\epsilon = 0$ and $\kappa = 30\Omega$.

In Fig. 5.3(a) we observe the purity of the qubit approach $\frac{1}{2}$ as before, but without recurring spikes. This is due to the fact that as soon as the state gets transfered into the degrees of freedom of the probe, it decays right away — the oscillator is always close to being in its ground state. In (b), by studying $\langle \sigma_z \rangle(t)$, and due to the finite size of Δ, we now observe a population loss. The rate of this $\langle \sigma_z \rangle$ decay, could in principle be approximated from Eq. 5.40 as in the regime where κ is large relative to the other energies in the system, the last two terms of Γ_d quickly tend to zero. This leads to an effective (and constant) depahsing rate of

$$\Gamma_d^{\text{eff}} = \frac{8\gamma^2 \kappa}{\kappa^2 + 4\Omega^2}, \tag{5.42}$$

and therefore an easily obtainable analytic solution the qubit's master equation (although this is not done here).

Lastly, we stress that this regime of operations does not lead to a good measurement. In the indirect measurement scheme discussed in Sec. 5.2, in order for the observer to be able to extract the state of the qubit, it has to imprint its information on the probe, and more importantly the corresponding state of the probe has to differ depending on what state the qubit is in. Here, with the very large decay rate out of the oscillator, the probe has no time to provide the observer with distinguishable enough scenarios, and hence provides no information about the measurement result.

5.9 Qubit Dynamics Results with $\Delta \neq 0$, Small κ

The final situation we consider is one where Δ is finite but the decay rate κ is not large, as it was in Sec. 5.8. Here, we expect the effective reduced master equation to not be valid except in the limits of very small Δ relative to the other energies, and at very short times. As was already mentioned, the presence of finite Δ causes a more complicated interaction as it mixes the various coefficient of the decomposition of the qubit's density matrix[17]. We can however consider a case of a short time and a very large qubit–oscillator coupling. In this case, we ad–hoc treat the contribution due to Δ, in the reduced master equation, is as in Sec. 5.8, by simply $-i\Delta\,[\sigma_x, \rho^q]$.

Figure. 5.4 shows the corresponding results. The parameters used are $\Omega = 2\pi$, $\gamma = 10\Omega$, $\kappa = \Omega/20$ and $\epsilon = 0$. Plot (a) shows results with an initial state $|+_x\rangle$, while plot (b) with $|0\rangle$. Because γ is so much larger than all the other energies in the problem, it dominates the evolution. The qubit is now dephased at a very fast rate (note different x–axis range from previous plots). From (b) we observe that the evolution causes the loss of population, which along with a nonzero κ, could be interpreted as a T_1 process. We stress that the ad–hoc use of the reduced master equation here has very limited success. Again from plot (b), we observe

---

[17] So for example in Appendix F, Eqs. F.18 and F.19 would get extra contributions from P_{ge} and P_{eg} respectively — this dramatically complicates the resulting solutions.

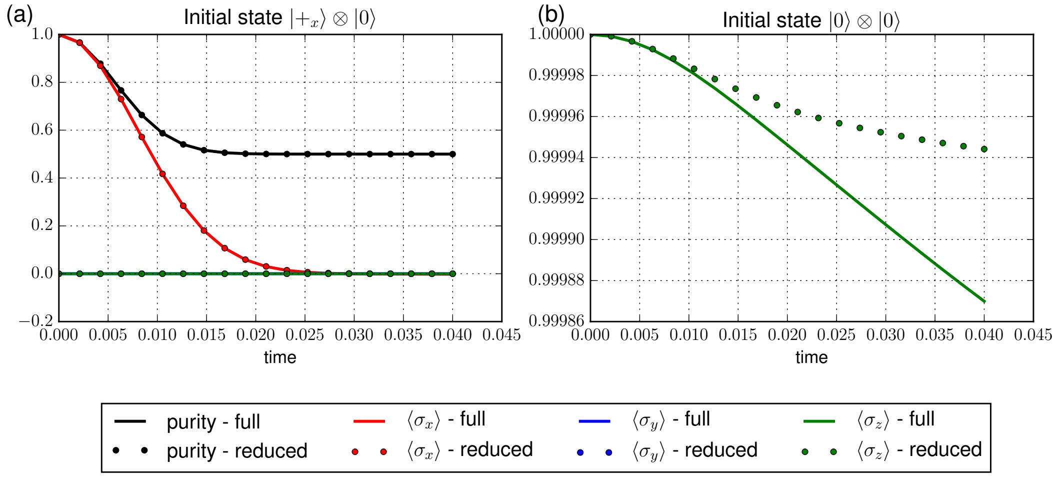

Figure 5.4: Short time evolution of the qubit with $\Delta = \pi/5$ and $\gamma = 20\pi$. The plots show the expectation values of σ_x (in red), σ_y (in blue), σ_z (in green) as well as purity (in black). (a) presents results with an initial qubit state $|+_x\rangle = \frac{1}{\sqrt{2}}(|0\rangle + |1\rangle)$, whereas (b) the state $|0\rangle$. In both cases the probe is assumed to be in its ground state at the start of the evolution. Solid (circle symbol) curves show the evolution obtained by solving the full (reduced) master equation. The other parameters used are set at $\Omega = 2\pi$, $\epsilon = 0$, and $\kappa = \pi/10$.

that past the time of 0.01, the full numerical solution starts to diverge from the approximate solution obtained with the reduced master equation. The key point to make about this scenario is that as long as the γ is very large, one could still arrive at an approximately QND–like measurement. In particular if we were to turn off the qubit–oscillator coupling γ at time ~ 0.025, the qubit would be in a fully mixed state, and yet only a small portion of its population would be lost. Since in this case κ is not overly large relative to the energy of the probe Ω, we could expect that it could oscillate for long enough so that its signal could be used to distinguish between the states of the qubit. This very scenario is studied in detail in [110] although with a smaller γ.

5.10 Evolution of the Probe — Potential Future Research Direction

Our goal in this chapter has been to discuss the behavior of the qubit as it evolves together with the coupled probe. In order to fully study the setup presented here as a measurement, however, we would also need to more closely look the behavior of the probe. In particular, we would need to show that any kind of evolution that dephases the qubit and produces a maximally mixed state, also displaces the oscillator enough so that the two pointer states, each associated with a different qubit state, can be actually distinguished. This kind of study in an identical system has been done in [110], but concentrated on the case where Δ is small and the qubit–probe coupling large. We consider a more detailed discussion of other parameter regimes a potential future research direction that could build on the results presented here.

In the next section we keep on discussing the dynamics of the qubit, but now in terms the Kraus map representation.

5.11 Kraus Maps Approximations of the Master Equation Evolution

Let us now switch gears for a while. So far we have studied the dynamics of the qubit's evolution by a means of solving the master equation. We considered two cases, the first where we have treated the full system of the qubit as well as the oscillator, only to trace out the degrees of freedom of the oscillator at the end, and the second, where we have attempted to account for the effects of the presence of the oscillator (and its environment) by calculating an expression for a reduced master equation, only for the degrees of freedom of the qubit, and solving it directly.

In this section, we discuss another means of describing a quantum evolution through linear maps defined in terms of Kraus operators. We compare the evolution obtained through solving the (full) master equation to two different Kraus maps — the first representing a dephasing map, and the other a combination of dephasing and rotation. The motivation behind this kind of comparison is to see how well a crude guess at an evolution map, resembles the real evolution. Our guesses for the two different Kraus maps are motivated by the form of the Hamiltonian of the system.

5.11.1 Kraus Map Representation and the χ–Matrix

As already hinted in the last couple of paragraphs, we can describe the evolution of a quantum system by means of linear maps, which in turn can be expressed in a convenient way using the Kraus representation (often also called the *operator–sum representation*), which we describe here. Mathematically, we consider an operator Λ, which transforms a density matrix ρ to another density matrix, namely $\rho \to \Lambda(\rho)$. We assume that Λ obeys the following constraints [96]. It needs to be:

1. **Linear**
   If $\rho = \alpha\rho_1 + (1-\alpha)\,\rho_2$, then $\Lambda(\rho) = \alpha\Lambda(\rho_1) + (1-\alpha)\,\Lambda(\rho_2)$.

2. **Trace preserving**
   If $\mathrm{Tr}(\rho) = 1$, then $\mathrm{Tr}(\rho') = 1$, where $\rho' = \Lambda(\rho)$.

3. **Hermiticity preserving**
   If $\rho = \rho^\dagger$, then $\rho' = \rho'^\dagger$, where $\rho' = \Lambda(\rho)$.

4. **Complete positivity preserving**
   First we note that a map Λ is positive if $\Lambda(\rho)$ is nonnegative, when ρ is nonnegative. In order to satisfy complete positivity, we first assume that ρ is acting on the Hilbert $\mathcal{H}_A$. Λ can be considered completely positive (CP), if for any extension of the Hilbert space of $\mathcal{H}_A$, such as $\mathcal{H}_A \otimes \mathcal{H}_B$, the extended map $\Lambda \otimes \mathbb{1}$ is positive.

The Kraus theorem[75] tells us that the effect of Λ on ρ can be expressed as

$$\Lambda(\rho) = \sum_{n=1}^{N} K_n \rho K_n^\dagger, \tag{5.43}$$

where each K_n is referred to as a Kraus operator. Furthermore, it is required that each K_n satisfies

$$\sum_{n=1}^{N} K_n^\dagger K_n = \mathbb{1}. \tag{5.44}$$

We stress that such a representation is not unique. In a Hilbert space of dimension d, one can show that $N \leq d$. An important assumption that one is required to make when describing Λ using Eq. 5.43, is that the input state ρ needs to be in a product state with the rest of the world, or in other words, the initial state of the system described by ρ should not be correlated with the degrees of freedom outside of its own Hilbert space. We will assume this to be the case in the following discussions.

One important Kraus map that we will use is the phase–flip map. It is defined as

$$\Lambda_{\mathrm{dz}}(\rho) = p\mathbb{1}\rho\mathbb{1} + (1-p)\sigma_z\rho\sigma_z, \tag{5.45}$$

with $0 \leq p \leq 1$. Its effect is to remove information about the relative phase between the $|0\rangle$ and $|1\rangle$ states. In particular, it contracts state vectors that are not aligned along the z–axis on the Bloch sphere. It can be easily seen that in the special case, when $p = \frac{1}{2}$ the result of applying Λ_{dz} is in fact equivalent to a measurement of the σ_z operator, with the result of the measurement kept unknown. This map is often also called the *phase damping* map[18], or alternatively a *dephasing map.* We will use the latter expression, and generalize it, by instead of using σ_z as the operator acting on ρ in the second term of Eq. 5.45, we will use an operator that defines an axis through a Bloch sphere specified by some arbitrary angles θ and ϕ. For a more complete outline of other common Kraus maps, we point the reader to [96] and [69].

A very convenient extension to Eq. 5.43, is to rewrite each K_n in terms of a set of linearly independent B_j, which form an operator basis on the state space. Mathematically this leads to

$$K_n = \sum_j^N b_{nj} B_j, \tag{5.47}$$

with each b_{nj} being a complex number. This lets us rewrite Eq. 5.43 as

$$\begin{aligned}\Lambda(\rho) &= \sum_{j,j',n} b_{nj} B_j \rho B_{j'}^{\dagger} b_{j'n}^{*} &(5.48)\\ &= \sum_{j,j'} B_j \rho B_{j'}^{\dagger} \sum_n b_{nj} b_{j'n}^{*} &(5.49)\\ &= \sum_{j,j'} B_j \rho B_{j'}^{\dagger} \chi_{j,j'} &(5.50)\end{aligned}$$

where we have defined

$$\chi_{j,j'} = \sum_n b_{nj} b_{j'n}^{*}. \tag{5.51}$$

χ is often called the *process matrix* or even simply the *χ–matrix* [96]. Assuming that B_j are fixed, the complex number matrix χ above, uniquely describes the map Λ. In general, it contains $d^4 - d^2$ independent real parameters.

Now that we have general description of a map Λ in terms of its χ–matrix, we can look at calculating it explicitly.

---

[18] An alternative, but very common way to express it, is with the following choice of Kraus operators

$$K_1 = \begin{bmatrix} 1 & 0 \\ 0 & \sqrt{1-\beta} \end{bmatrix}, \qquad K_2 = \begin{bmatrix} 0 & 0 \\ 0 & \sqrt{\beta} \end{bmatrix}, \tag{5.46}$$

with $\beta = 2p(p-1)$.

5.11.2 χ–Matrix for an Evolution of a Single Qubit

In the next few paragraphs, we will outline a procedure of characterizing a map Λ in terms of its χ–matrix representation, that satisfies the conditions 1–4 shown in the last section, for a case of a single qubit. We will follow the discussion presented in[19] [24] as well as [96]. The key assumption of the method shown, is that we can prepare the qubit in a few specific physical input states, apply the map, and later obtain the resulting density matrix through, for example, process tomography.

Given that we have already established that Λ can be described using Eq. 5.43, and therefore through the χ–matrix, our first step is to define the operator basis that span a 4–dimensional Hilbert space of a single qubit. Following [24] as well as [96] we chose

$$\begin{aligned} B_0 &= \mathbb{1} \\ B_1 &= \sigma_x \\ B_2 &= -i\sigma_y \\ B_3 &= \sigma_z. \end{aligned} \tag{5.52}$$

Next we need to understand how Λ acts on four different initial states ρ_i, with $i = 1..4$. Namely we need to find $\rho'_i = \Lambda(\rho_i)$. In general we have some freedom in choosing the initial states ρ_i, with arguably the most obvious choice being the standard matrix basis

$$\rho_1 = \begin{bmatrix} 1 & 0 \\ 0 & 0 \end{bmatrix}, \tag{5.53}$$

as well as $\rho_2 = \rho_1\sigma_x$, $\rho_3 = \sigma_x\rho_1$ and $\rho_4 = \sigma_x\rho_1\sigma_x$. We stress however, that ρ_2 and ρ_3 defined in such a way, are not physical. In order to remedy this, we can expand these operators in terms of physically accessible states, constructed out of $|+_x\rangle$ and $|+_y\rangle$, the eigenvectors of σ_x and σ_y respectively[20]. This lets us summarize all the transformations as

$$\begin{aligned} \rho'_1 &= \Lambda(\rho_1) \\ \rho'_4 &= \Lambda(\rho_4) \\ \rho'_2 &= \Lambda(|+_x\rangle\langle+_x|) + i\Lambda(|+_y\rangle\langle+_y|) - \frac{1}{2}(1+i)(\rho'_1 + \rho'_4) \\ \rho'_3 &= \Lambda(|+_x\rangle\langle+_x|) - i\Lambda(|+_y\rangle\langle+_y|) - \frac{1}{2}(1-i)(\rho'_1 + \rho'_4). \end{aligned} \tag{5.54}$$

---

[19] The reference [24] contains many typos and should not be used directly without double–checking the mathematical details. Reference [96] on the other hand, seems to have most of the typos fixed, although there is still a problem with Eqs 8.175 and 8.176 (in 10th edition). The corrected expressions equivalent to those equations are shown in this section as Eq. 5.54.

[20] We define $|+_x\rangle = \frac{1}{\sqrt{2}}(|0\rangle + |1\rangle)$ and $|+_y\rangle = \frac{1}{\sqrt{2}}(|0\rangle + i|1\rangle)$.

In an experimental setting, where Λ would correspond to a real physical process, each ρ'_i would have to be measured through process tomography. Having obtained all the ρ'_i, we are finally ready to write down the χ–matrix of the map. It our case of a single qubit, it can be shown to be

$$\chi = \Upsilon \begin{bmatrix} \rho'_1 & \rho'_2 \\ \rho'_3 & \rho'_4 \end{bmatrix} \Upsilon, \tag{5.55}$$

with

$$\Upsilon = \frac{1}{2} \begin{bmatrix} \mathbb{1} & \sigma_x \\ \sigma_x & -\mathbb{1} \end{bmatrix}. \tag{5.56}$$

Hence by applying Λ to four different states and measuring the outcomes, we have a means to completely characterize it mathematically. In the next section, we will use the method just outlined to compare maps obtained through different means.

5.11.3 Map Comparisons

In this section we will compare the evolution obtained through solving the master equation of our system, to that of two different maps — the first, that of dephasing about an arbitrary axis on the Bloch sphere, and the second, a combination of X–rotation and Z–dephsaing. Each of these maps will be described by their respective χ–matrix, which will be expressed in terms of three free parameters. By minimizing the distance between the χ–matrices of these maps and the ones obtained through solving the master equation over the free parameters, we will study how well these (overly simplistic) maps can approximate the "true" (i.e., as calculated by the master equation) evolution of our system.

The calculate the distance between the different χ–matrices, we will consider the *trace distance*[21], which mathematically can be defined as

$$D(\chi_{\mathrm{me}}, \chi_{\mathrm{map}}) = \frac{1}{2} |\chi_{\mathrm{me}} - \chi_{\mathrm{map}}|_1. \tag{5.57}$$

χ_{me} is meant to represent the χ–matrix obtained from the master equation evolution of the system, while χ_{map} one obtained from the definition of a map we are trying to compare to. Operationally, we calculate $D(\chi_{\mathrm{me}}, \chi_{\mathrm{map}})$ as

$$D(\chi_{\mathrm{me}}, \chi_{\mathrm{map}}) = \frac{1}{2} \sum_i \sqrt{\lambda_i} \tag{5.58}$$

---

[21] There are many other distance measures that we could use to compare two matrices. Our choice of the trace distance shown in Eq. 5.57 comes from the fact that it can be shown to be equivalent to process fidelity. Another widely used distance measure that can also be assigned a relevant physical meaning and would likely be effective here, is the diamond norm [70].

where λ_i is the ith eigenvalue of the matrix $(\chi_{\mathrm{me}} - \chi_{\mathrm{map}})(\chi_{\mathrm{me}} - \chi_{\mathrm{map}})^\dagger$.

We would naturally expect that the evolution of our system should closely depend on the total Hamiltonian (along with any relevant Lindblad operators that we have assumed model the effect of the environment) as well as time. In order to explore the interplay between the size of the qubit splitting energy at zero flux Δ, as well as the strength of the qubit–oscillator coupling γ, on the measurement process, we concentrate on a special case where $\epsilon = 0$ in the expression of the system Hamiltonian shown in Eq. 3.16. Furthermore, we fix $\Delta = \pi$, and the total evolution time to $t = 0.1\Delta$, while varying γ between values of 0 and 20Δ. The oscillator decay rate is taken as $\kappa = 0.01\Delta$. Just from looking at the Hamiltonian, we can predict existence of two regimes. When $\Delta \gg \gamma$, the evolution will be dominated by rotation of the qubit around the x–axis and when $\Delta \ll \gamma$, and the decay rate out of the oscillator κ large enough, the qubit will dephase. In the next few paragraph we will see if this simplistic description can be in fact made more concrete by the map comparisons.

Dephasing About Arbitrary Axis

We start with a case of a map that represents dephasing about an axis on the Bloch sphere, defined by three parameters θ, ϕ and p. The effect of such a map can be written as

$$\Lambda_{\mathrm{dr}}(\rho) = p\mathbb{1}\rho\mathbb{1} + (1-p)R(\theta,\phi)\rho R(\theta,\phi)^\dagger, \tag{5.59}$$

where we have taken $R(\theta,\phi) = \cos(\phi)\sin(\theta)\sigma_x + \sin(\phi)\sin(\theta)\sigma_y + \cos(\theta)\sigma_z$. The corresponding Kraus operators are easily calculated to be $K_1 = \sqrt{p}\mathbb{1}$ and $K_2 = \sqrt{1-p}R(\theta,\phi)$. If we assume natural ranges of the parameters such that $0 \le \theta \le \pi$, $0 \le \phi \le 2\pi$ and $0 \le p \le 1$, it is easy to check that Eq. 5.44 is satisfied. Following the procedure outlined in Sec. 5.11.2 we can calculate the χ–matrix for the map Λ_{dr}, which reads

$$\chi_{\mathrm{dr}}(\theta,\phi,p) = \frac{(p-1)}{2}\begin{bmatrix} \frac{2p}{p-1} & 0 & 0 & 0 \\ 0 & -2\cos^2(\phi)\sin^2(\theta) & i\sin^2(\theta)\cos(2\phi) & -\sin(2\theta)\cos(\phi) \\ 0 & -i\sin^2(\theta)\cos(2\phi) & -2\sin^2(\phi)\sin^2(\theta) & -i\sin(2\theta)\sin(\phi) \\ 0 & -\sin(2\theta)\cos(\phi) & i\sin(2\theta)\sin(\phi) & -2\cos^2(\theta). \end{bmatrix}. \tag{5.60}$$

One can verify that this matrix satisfies obvious boundary cases. For example when $\theta = 0 = \pi$ and $p = \frac{1}{2}$, we end up with

$$\chi_{\mathrm{dr}}(\theta, \phi, p) = \frac{1}{2}\begin{bmatrix} 1 & 0 & 0 & 0 \\ 0 & 0 & 0 & 0 \\ 0 & 0 & 0 & 0 \\ 0 & 0 & 0 & 1 \end{bmatrix}, \tag{5.61}$$

which corresponds to perfect dephasing about the z–axis.

Z–Dephasing and X–Rotation

Next, let us consider a map which consist of a combination of a rotation about the x–axis as well as dephasing about the z–axis. The effect of such a map can be written as

$$\Lambda_{\mathrm{dz+rx}}(\rho) = \phi\Lambda_{\mathrm{dz}}(\rho) + (1-\phi)\Lambda_{\mathrm{rx}}(\rho), \tag{5.62}$$

where

$$\Lambda_{\mathrm{dz}}(\rho) = p\mathbb{1}\rho\mathbb{1} + (1-p)\sigma_z\rho\sigma_z, \tag{5.63}$$

and

$$\Lambda_{\mathrm{rx}}(\rho) = U(\theta)\rho U(\theta)^\dagger, \tag{5.64}$$

with

$$U(\theta) = \exp\left(-i\frac{\theta}{2}\sigma_x\right), \tag{5.65}$$

a standard rotation about the x–axis by an angle θ. The Kraus operators corresponding to this map can be shown to be

$$K_1 = \sqrt{\phi p}\mathbb{1}, \qquad K_2 = \sqrt{\phi(1-p)}\sigma_z, \qquad K_3 = \sqrt{1-\phi}\begin{bmatrix} \cos\frac{\theta}{2} & i\sin\frac{\theta}{2} \\ -i\sin\frac{\theta}{2} & \cos\frac{\theta}{2} \end{bmatrix}. \tag{5.66}$$

We stress that the parameters θ, ϕ as well as p play a different role here than they did when we considered a purely dephasing map Λ_{dr}. Their domains are $0 \leq \theta \leq 2\pi$, $0 \leq \phi \leq 1$ and $0 \leq p \leq 1$. Once again, we calculate the χ–matrix for the map

$\Lambda_{\mathrm{dz+rx}}$, which reads

$$\chi_{\mathrm{dz+rx}} = \begin{bmatrix} (1-\phi)\cos^2\left(\frac{\theta}{2}\right)+\phi p & -\frac{1}{2}i(\phi-1)\sin(\theta) & 0 & 0 \\ \frac{1}{2}i(\phi-1)\sin(\theta) & (1-\phi)\sin^2\left(\frac{\theta}{2}\right) & 0 & 0 \\ 0 & 0 & 0 & 0 \\ 0 & 0 & 0 & \phi(1-p) \end{bmatrix}. \tag{5.67}$$

We are now ready to compare the behavior χ_{dr} and $\chi_{\mathrm{dz+rx}}$ to the evolution obtained through solving the master equation.

Map Comparison Results

The results are presented in Fig. 5.5. Figure 5.5(a) shows the distance between the map obtained from the full master equation evolution and Λ_{dr} (blue curve) as well as $\Lambda_{\mathrm{dz+rx}}$ (red curve), as a function of the ratio γ/Δ. Figures 5.5(b), 5.5(c) and 5.5(d) show the optimal values of θ, ϕ and p respectively, again as a function of γ/Δ. As we already discussed, these values are obtained through the process of minimization of the trace distance between the maps, that was defined in Eq. 5.57.

In the limit where $\gamma \ll \Delta$, the evolution of the system is dominated by the Δ term in the Hamiltonian from Eq. 3.16, which translates to a simple rotation around the x–axis. From Fig. 5.5(a) we see that $\Lambda_{\mathrm{dz+rx}}$ is in very good agreement as its trace distance to the true evolution in this limit is near zero. Furthermore, the optimization leads to the optimal value of $\theta \approx \pi/5$ as can be seen from Fig. 5.5(b). This is consistent with the fact that the total rotation angle that we would expect from the evolution for the parameters we have chosen, should be $2\Delta t = \pi/5$. Finally, having both $p \approx \phi \approx 0$ implies that only the Λ_{rx} portion of the map shown in Eq. 5.62 is playing a role. Next, looking at the data for the case of the Λ_{dr} map (blue curves), still in the regime where $\gamma \ll \Delta$, we see that its agreement with the master equation evolution is poor. This is mainly because there is no set of parameters that can be chosen where this simple rotation could be mimicked. We stress that the situation would be different if, for example, the total evolution time were such that $\Delta t = \pi/2$, as this case the effective transformation of the density matrix of our system could be written as simply $\rho \to \sigma_x \rho \sigma_x$, which could be emulated with $\Lambda_{\mathrm{dz+xr}}$ by choosing $\phi = p = 0$ and $\theta = \pi$.

In the opposite regime, where $\gamma \gg \Delta$, we find that both maps approach a good agreement with the evolution of our system. This is exactly what we would expect. Here, even though Δ is nonzero, the evolution is dominated by the $\sim \gamma\sigma_z$ term in the Hamiltonian that couples the qubit to the oscillator. The fact that the oscillator decays to the environment, causes the qubit to dephase (we can verify this by studying the density matrix obtained from the master equation evolution, which is not explicitly shown here). Both maps $\Lambda_{\mathrm{dz+rx}}$ as well as Λ_{dr} are dephasing maps by construction, and in both cases the optimization over θ, ϕ and p simply

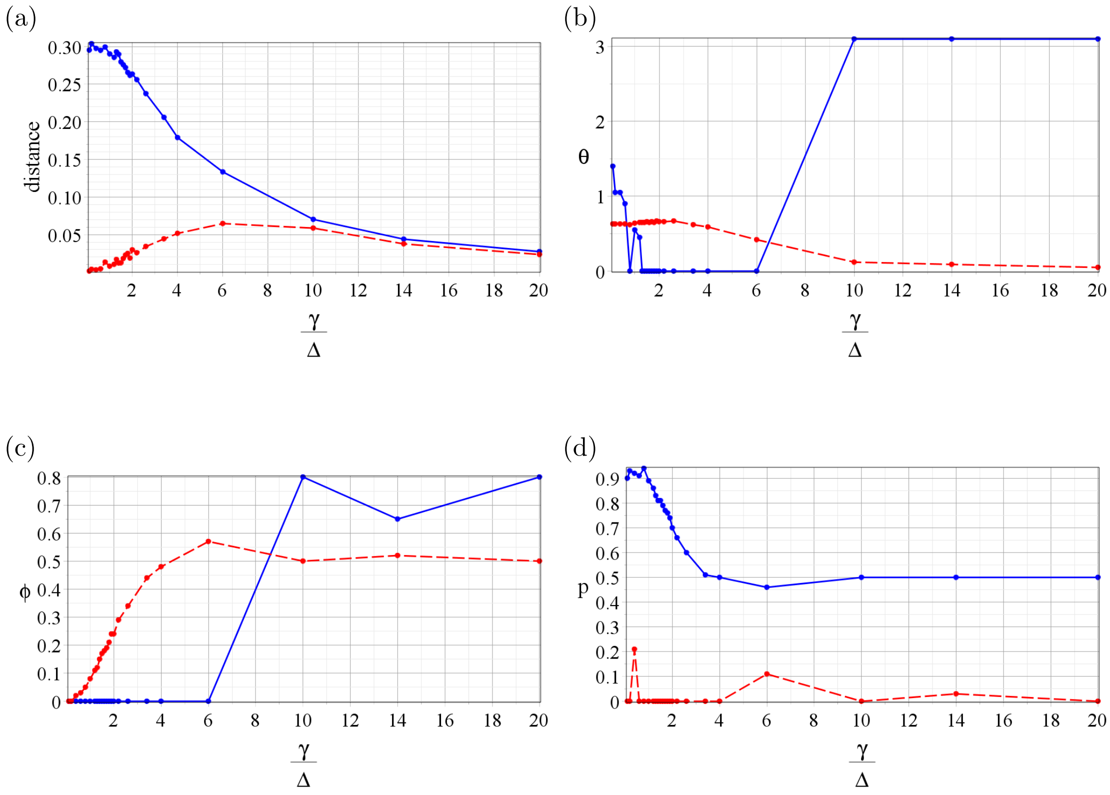

Figure 5.5: Map comparisons between the evolution calculated through solving the master equation for our qubit–oscillator system and simple maps consisting of dephasing about arbitrary axis around the Bloch sphere (blue curves) and a combination of x–axis rotation and dephasing about the z–axis (red curves). Plot (a) shows the trace distance between the corresponding χ–matrices as a function of the ratio $\frac{\gamma}{\Delta}$, while plots (b-d) show the optimal values of the parameters θ, ϕ and p. We observe good agreement (small trace distance) of both of the maps to the master equation evolution in the regime where $\gamma \gg \Delta$, as well as the combination of x–axis rotation and z–axis dephasing in the limit where $\gamma \ll \Delta$. See main text for discussion.

chooses the right parameters to mimic dephasing specifically around the z–axis. In the case $\Lambda_{\mathrm{zd+rx}}$ this leads to $\phi \approx 1/2$, $p \approx 0$ and $\theta \approx 0$. We stress that this is not the most obvious choice, but it works, because with $\theta \ll 1$, $U(\theta) \approx \mathbb{1}$. Clearly a more obvious solution (to a human!), might be to simply pick $\phi = 1$, in which case the rotation around θ would not play any role at all. In the case of Λ_{dr}, the angles are simply chosen so that the $R(\theta, \phi) \sim \sigma_z$, which means $\theta = \pi$ (although $\theta = 0$ would also clearly work) along with $p = 1/2$. The value of ϕ is irrelevant here, because having $\theta = \pi$ gets rid of all the off–diagonal entries in $R(\theta, \phi)$.

Finally, in the intermediate region where $\gamma \approx \Delta$, and where the evolution cannot be thought off as a simple rotation or dephasing, we see that our maps are not as good at approximating the outcome of the simulations. More elaborate examples could be chosen that we could optimize over. It is worth pointing out however, that while these kinds of "map guesses" might be instructive in quickly assessing the general behavior of a given system based on data obtained through process tomography, their real world applications, where the data may come from experiments, might be limited. Since in most situations one usually has at least some understanding of the system's Hamiltonian, often solving the master equation directly may be more desirable.

5.12 Summary and Conclusions

In this chapter we studied the dynamics of a qubit coupled to a harmonic oscillator, in the context of a quantum measurement. Using a polaron–type transformation, we calculated an effective qubit dephasing rate, valid in the QND measurement limit, where qubit–probe interaction commutes with the free evolution of the qubit itself. We also numerically explored regimes where this was not the case, and briefly discussed the related consequences. Finally, we concluded with a study of Kraus maps consisting of rotations and dephasing, and looked at how well they can model the evolution of the qubit in different parameter regimes.

Chapter 6

Conclusions and Outlook

In the last few years, superconducting circuits have shown to play an important role in many research areas, particularly in fields related to quantum computation and information, but also in subfields of physics that explore fundamental effects which have been hard or even impossible to study otherwise. This is largely due to the remarkable flexibility and experimental accessibility that they offer — from a small subset of simple circuit elements we can construct a variety of Hamiltonians, and therefore model many different behaviors, but more importantly perhaps, physicists are becoming better than ever at building circuits that are much less susceptible to outside noise, and provide means of precise control over their behavior.

The main theme of this thesis therefore, has been to study the dynamics as well as general quantum behaviour of a few superconducting circuit systems, that might at least slightly advance our understanding of this quickly evolving field. In the first part, we looked at Casimir and Casimir–Polder like effects that could be realized in a circuit consisting of a charge qubit coupled to a stripline cavity with a tunable boundary, which was constructed out of a DC–SQUID. These effects were mediated by the boundary DC–SQUID circulating currents, which, for a realistic set of physical parameters, have been calculated to be of the orders of $10^{-8}\,\mathrm{A}$ in the Casimir case, and $10^{-13}\,\mathrm{A}$ in the Casimir–Polder case. In the second part, we theoretically studied the classical dynamics of a highly nonlinear DC–SQUID oscillator and showed that our model closely agrees with experimentally produced results obtained by the Britton Plourde's group at Syracuse University. Finally, in the last part, we discussed, in the context of a measurement, the dynamics of a system consisting of a qubit coupled to a harmonic oscillator that could be implemented using a flux qubit inductively coupled to a DC–SQUID. While all of the three projects are fairly different in nature, each hopefully sheds some light on a small aspect of the applicability of a superconducting circuit systems in these various scenarios.

As is usually the case in science, there are many facets of of these projects that could be explored further. In the case of the Casimir and Casimir–Polder discussion, the central peace of the puzzle that still needs to be studied in detail, is how a measurement of these effects could be implemented. Related to this, it would be also instructive to explore some ideas that would let us make these currents large so that they are easier to observe. Both of these topics were briefly discussed in Secs. 3.11 and 3.8.5, but there is a lot of potential for future exploration. In the second project, we only scratched the surface of how a nonlinear oscillator operated in a transient regime could be used as a simple flux detector. Both experimental as well as theoretical work is needed to explore the optimal properties, such as input pulse shape, integration time, and even most reasonable flux biasing in order to maximize the contrast of a readout. Finally, in the last project that looked at at dynamics of qubit undergoing a measurement, we concentrated our discussion on the evolution of the qubit only. In order to complete the picture and discus the full measurement process, we would need to also study the corresponding dynamics of the probe, and more importantly, show over what kind of system parameters can an observer learn about the qubit, by only directly observing the probe. All of these issues are interesting, and may be explored further in the future.

APPENDICES

Appendix **A**

Normalization of Stripline Cavity Normal Modes

In this appendix we explicitly show the calculation involving the normalization of the normal modes of the cavity open at $x = x_l$, and with a DC–SQUID at $x = 0$, as described in Chapter 3.

In Sec. 3.4 we used an ansatz that the cavity normal modes have a form

$$u_n(x) = \eta_n \cos\left(\frac{\omega_n}{v}x + \theta_n\right), \tag{A.1}$$

with θ_n and ω_n satisfying

$$\theta_n = \tan^{-1}\left(C_{Js}Z_0\frac{\omega_n^2 - \omega_s(\Phi_s)^2}{\omega_n}\right) \tag{A.2}$$

$$\omega_n = \frac{v}{x_l}\left(n\pi - \theta_n\right), \tag{A.3}$$

and with η_n to be determined. We chose to normalize $u_n(x)$ subject to the weight function $w(x) = (\delta(x)C_{Js} + \Theta(x)c)$, with $\Theta(x)$ representing the Heaviside function, and the other parameters as defined in Chapter 3. Hence, in order to calculate η_n, we need to ensure that

$$\int_{-\infty}^{x_l} u_n(x)u_{n'}(x)w(x)dx = \delta_{n,n'}. \tag{A.4}$$

Let us begin by first considering

$$\int_{-\infty}^{x_l} u_n(x)u_{n'}(x)dx = \int_{-\infty}^{x_l} \eta_n\eta_{n'}\cos\left(\frac{\omega_n}{v}x + \theta_n\right)\cos\left(\frac{\omega_{n'}}{v}x + \theta_{n'}\right)dx. \tag{A.5}$$

In the case of $n = n'$, we have

$$\begin{aligned}\int_{-\infty}^{x_l} u_n(x)u_n(x)dx &= \int_{-\infty}^{x_l} \eta_n^2 \cos^2\left(\frac{\omega_n}{v}x + \theta_n\right) dx \\ &= \eta_n^2\left(\frac{x_l}{2} + \frac{v}{4\omega_n}\left(\sin\left(\frac{2\omega_n}{v}x + 2\theta_n\right) - \sin 2\theta_n\right)\right).\end{aligned} \tag{A.6}$$

Using Eq. A.3 we have $\sin\left(\frac{2\omega_n}{v}x + 2\theta_n\right) = \sin(2n\pi) = 0$, which leads to

$$\int_{-\infty}^{x_l} u_n(x)u_n(x)dx = \eta_n^2\left(\frac{x_l}{2} - \frac{v}{4\omega_n}\sin 2\theta_n\right). \tag{A.7}$$

When $n \neq n'$,

$$\int_{-\infty}^{x_l} u_{n'}(x)u_{n'}(x)dx = -\eta_n\eta_{n'}vC_{Js}Z_0\cos\theta_n\cos\theta_{n'}. \tag{A.8}$$

Using these results we can then write

$$\begin{aligned}\int_{-\infty}^{x_l} u_n(x)u_{n'}(x)w(x)dx &= \int_{-\infty}^{x_l} u_n(x)u_{n'}(x)\left(\delta(x)C_{Js} + \Theta(x)c\right)dx \\ &= C_{Js}\eta_n\eta_{n'}\cos\theta_n\cos\theta_{n'} + c\int_{-\infty}^{x_l}\Theta(x)u_n(x)u_{n'}(x)dx.\end{aligned} \tag{A.9}$$

When $n \neq n'$, as required, this expression simplifies to zero, since

$$\begin{aligned}&C_{Js}\eta_n\eta_{n'}\cos\theta_n\cos\theta_{n'} + c\int_{-\infty}^{x_l}\Theta(x)u_n(x)u_{n'}(x)dx \\ &\qquad = (1 - vcZ_0)C_{Js}\eta_n\eta_{n'}\cos\theta_n\cos\theta_{n'} \\ &\qquad = 0,\end{aligned} \tag{A.10}$$

as $1 - vcZ_0 = 1 - \frac{1}{\sqrt{cl}}c\sqrt{\frac{l}{c}} = 0$.

When $n = n'$ on the other hand, Eq. A.9 simplifies to

$$\begin{aligned}\int_{-\infty}^{x_l} u_n(x)u_{n'}(x)w(x)dx &= \int_{-\infty}^{x_l} u_n(x)u_{n'}(x)\left(\delta(x)C_{Js} + \Theta(x)c\right)dx \\ &= C_{Js}\eta_n^2\cos^2\theta_n + c\eta_n^2\left(\frac{x_l}{2} - \frac{v}{4\omega_n}\sin(2\theta_n)\right) \\ &= \eta_n^2\left(\frac{C_t}{2} + C_{Js}\cos^2\theta_n - \frac{v}{4\omega_n}\sin(2\theta_n)\right),\end{aligned} \tag{A.11}$$

where we have defined the total stripline cavity capacitance $C_t = cx_l$. Equating this

---

expression to 1, and solving for η_n, leads to the normalization shown in Eq. 3.29.

Appendix B

Details of the Perturbative Energy Shift Calculation

In this appendix we show the details of the perturbative energy shift calculations presented in Sec. 3.6. The material shown here is meant to complement that discussion, and we point the reader to that section for the definitions of parameters and the general problem setup. We explicitly show the calculation for the case of a cavity with two field modes, but this result is generalized to an arbitrary mode number in Sec. 3.6.

First, we show the expression for the diamagnetic contribution to the energy shift, $\delta E^{\text{diam}}_{q,n_1,n_2}$

$$\begin{aligned}
\delta E^{\text{diam}}_{q,n_1,n_2} &= \langle q,n_1,n_2|\frac{\hbar}{\gamma}\left(\sum_{k=1,2} g_k^{(\pm)} i^{\frac{1\mp1}{2}}\left(a_k^\dagger \pm a_k\right)\right)^2 |q,n_1,n_2\rangle \\
&= \pm\frac{\hbar}{\gamma}\langle q,n_1,n_2|\left(g_1^{(\pm)}\left(a_1^\dagger \pm a_1\right) + g_2^{(\pm)}\left(a_2^\dagger \pm a_2\right)\right)^2 |q,n_1,n_2\rangle \\
&= \pm\frac{\hbar}{\gamma}\langle q,n_1,n_2| \pm g_1^{(\pm)2}\left(a_1^\dagger a_1 + a_1 a_1^\dagger\right) \pm g_2^{(\pm)2}\left(a_2^\dagger a_2 + a_2 a_2^\dagger\right)|q,n_1,n_2\rangle \\
&= \pm\frac{\hbar}{\gamma}\langle q,n_1,n_2| \pm g_1^{(\pm)2}\left(2a_1^\dagger a_1 + 1\right) \pm g_2^{(\pm)2}\left(2a_2^\dagger a_2 + 1\right)|q,n_1,n_2\rangle \\
&= \frac{\hbar}{\gamma}\sum_{k=1,2} g_k^{(\pm)2}(2n_k+1).
\end{aligned} \tag{B.1}$$

Next, we look at the details of obtaining the paramagnetic contribution $\delta E^{\text{param}}_{q,n_1,n_2}$

$$\begin{aligned}
\delta E^{\text{param}}_{q,n_1,n_2} =& \sum_{\substack{p,j_1,j_2 \\ p,j_1,j_2 \neq q,n_1,n_2}} \frac{1}{E_{q,n_1,n_2} - E_{p,j_1,j_2}} \Bigg| \langle p, j_1, j_2| \hbar \sum_m x_{m,m+1} \sigma_x^m \sum_{k=1,2} g_k^{(\pm)} i^{\frac{1\mp 1}{2}} \left(a_k^\dagger \pm a_k \right) \\
&+ \hbar \sum_m z_m |m\rangle\langle m| \sum_{k=1,2} g_k^{(\pm)} i^{\frac{1\mp 1}{2}} \left(a_k^\dagger \pm a_k \right) |q, n_1, n_2\rangle \Bigg|^2 \\
=& \sum_{\substack{p,j_1,j_2 \\ p,j_1,j_2 \neq q,n_1,n_2}} \frac{\hbar^2}{E_{q,n_1,n_2} - E_{p,j_1,j_2}} \Bigg| \langle p, j_1, j_2| \sum_m \sum_{k=1,2} x_{m,m+1} \sigma_x^m g_k^{(\pm)} \left(a_k^\dagger \pm a_k \right) |q, n_1, n_2\rangle \\
&+ \langle p, j_1, j_2| \sum_m \sum_{k=1,2} z_m |m\rangle\langle m| g_k^{(\pm)} \left(a_k^\dagger \pm a_k \right) |q, n_1, n_2\rangle \Bigg|^2 .
\end{aligned} \tag{B.2}$$

Let us consider this expression term–by–term. First we have

$$\begin{aligned}
\langle p, j_1, j_2| &\sum_m \sum_{k=1,2} x_{m,m+1} \sigma_x^m g_k^{(\pm)} \left(a_k^\dagger \pm a_k \right) |q, n_1, n_2\rangle \\
&= \sum_m \sum_{k=1,2} x_{m,m+1} \delta_{p,m} \delta_{m+1,q} \langle j_1, j_2| g_k^{(\pm)} \left(a_k^\dagger \pm a_k \right) |n_1, n_2\rangle \\
&\quad + \sum_m \sum_{k=1,2} x_{m+1,m} \delta_{p,m+1} \delta_{m,q} \langle j_1, j_2| g_k^{(\pm)} \left(a_k^\dagger \pm a_k \right) |n_1, n_2\rangle \\
&= x_{p,q} \delta_{p+1,q} \sum_{k=1,2} \langle j_1, j_2| g_k^{(\pm)} \left(a_k^\dagger \pm a_k \right) |n_1, n_2\rangle \\
&\quad + x_{p,q} \delta_{p-1,q} \sum_{k=1,2} \langle j_1, j_2| g_k^{(\pm)} \left(a_k^\dagger \pm a_k \right) |n_1, n_2\rangle.
\end{aligned} \tag{B.3}$$

Next, we look at the last term from Eq. B.2

$$\begin{aligned}
\langle p, j_1, j_2| &\sum_m \sum_{k=1,2} z_m |m\rangle\langle m| g_k^{(\pm)} \left(a_k^\dagger \pm a_k \right) |q, n_1, n_2\rangle \\
&= z_p \delta_{p,q} \sum_{k=1,2} \langle j_1, j_2| g_k^{(\pm)} \left(a_k^\dagger \pm a_k \right) |n_1, n_2\rangle.
\end{aligned} \tag{B.4}$$

Finally, in order to simplify the last two expressions further, we note that

$$\begin{aligned}\sum_{k=1,2}\langle j_1,j_2|g_k^{(\pm)}\left(a_k^\dagger\pm a_k\right)|n_1,n_2\rangle=&\\ &=\langle j_1,j_2|(g_1^{(\pm)}\left(\sqrt{n_1+1}|n_1+1,n_2\rangle\pm\sqrt{n_1}|n_1-1,n_2\rangle\right)\\ &\quad+\langle j_1,j_2|g_2^{(\pm)}\left(\sqrt{n_2+1}|n_1,n_2+1\rangle\pm\sqrt{n_2}|n_1,n_2-1\rangle\right)\\ &=g_1^{(\pm)}(\sqrt{n_1+1}\delta_{j_1,n_1+1}\delta_{j_2,n_2}\pm\sqrt{n_1}\delta_{j_1,n_1-1}\delta_{j_2,n_2})\\ &\quad+g_2^{(\pm)}(\sqrt{n_2+1}\delta_{j_1,n_1}\delta_{j_2,n_2+1}\pm\sqrt{n_2}\delta_{j_1,n_1}\delta_{j_2,n_2-1}).\end{aligned}\tag{B.5}$$

Substituting Eqs. B.3, B.4 and B.5 into B.2 and simplifying leads to

$$\begin{aligned}\delta E_{q,n_1,n_2}^{\text{param}}=&\sum_{\substack{p,j_1,j_2\\ p,j_1,j_2\neq q,n_1,n_2}}\frac{\hbar^2}{E_{q,n_1,n_2}-E_{p,j_1,j_2}}\Big|\left(x_{p,q}\delta_{p+1,q}+x_{p,q}\delta_{p-1,q}+z_p\delta_{p,q}\right)\times\\ &\Big(g_1^{(\pm)}(\sqrt{n_1+1}\delta_{j_1,n_1+1}\delta_{j_2,n_2}\pm\sqrt{n_1}\delta_{j_1,n_1-1}\delta_{j_2,n_2})\\ &+g_2^{(\pm)}(\sqrt{n_2+1}\delta_{j_1,n_1}\delta_{j_2,n_2+1}\pm\sqrt{n_2}\delta_{j_1,n_1}\delta_{j_2,n_2-1})\Big)\Big|^2\\ =&\hbar^2|x_{q,q+1}|^2\left(\frac{|g_1^{(\pm)}|^2(n_1+1)}{E_{q,n_1,n_2}-E_{q+1,n_1+1,n_2}}+\frac{|g_1^{(\pm)}|^2n_1}{E_{q,n_1,n_2}-E_{q+1,n_1-1,n_2}}\right.\\ &\left.+\frac{|g_2^{(\pm)}|^2(n_2+1)}{E_{q,n_1,n_2}-E_{q+1,n_1,n_2+1}}+\frac{|g_2^{(\pm)}|^2n_2}{E_{q,n_1,n_2}-E_{q+1,n_1,n_2-1}}\right)\\ &+\hbar^2|x_{q,q-1}|^2\left(\frac{|g_1^{(\pm)}|^2(n_1+1)}{E_{q,n_1,n_2}-E_{q-1,n_1+1,n_2}}+\frac{|g_1^{(\pm)}|^2n_1}{E_{q,n_1,n_2}-E_{q-1,n_1-1,n_2}}\right.\\ &\left.+\frac{|g_2^{(\pm)}|^2(n_2+1)}{E_{q,n_1,n_2}-E_{q-1,n_1,n_2+1}}+\frac{|g_2^{(\pm)}|^2n_2}{E_{q,n_1,n_2}-E_{q-1,n_1,n_2-1}}\right)\\ &+\hbar^2|z_q|^2\left(\frac{|g_1^{(\pm)}|^2(n_1+1)}{E_{q,n_1,n_2}-E_{q,n_1+1,n_2}}+\frac{|g_1^{(\pm)}|^2n_1}{E_{q,n_1,n_2}-E_{q,n_1-1,n_2}}\right.\\ &\left.+\frac{|g_2^{(\pm)}|^2(n_2+1)}{E_{q,n_1,n_2}-E_{q,n_1,n_2+1}}+\frac{|g_2^{(\pm)}|^2n_2}{E_{q,n_1,n_2}-E_{q,n_1,n_2-1}}\right).\end{aligned}\tag{B.6}$$

We now need to evaluate the denominator terms containing the energy differences between various energy levels. Let us look at a couple of cases explicitly

$$E_{q,n_1,n_2}-E_{q+1,n_1+1,n_2}=\hbar\varepsilon_q+\left(n_1+\frac{1}{2}\right)\hbar\omega_1+\left(n_2+\frac{1}{2}\right)\hbar\omega_2\tag{B.7}$$

$$-\left(\hbar\varepsilon_{q+1}+\left(n_1+\frac{1}{2}+1\right)\hbar\omega_1+\left(n_2+\frac{1}{2}\right)\hbar\omega_2\right)\tag{B.8}$$

$$=\hbar\left((\varepsilon_q-\varepsilon_{q+1})-\omega_1\right),\tag{B.9}$$

and

$$E_{q,n_1,n_2} - E_{q+1,n_1-1,n_2} = \hbar\left((\varepsilon_q - \varepsilon_{q+1}) + \omega_1\right). \tag{B.10}$$

Performing similar calculations for the other terms leads to

$$\begin{aligned}
\delta E^{\text{param}}_{p,n_1,n_2} =&\hbar|x_{q,q+1}|^2 \sum_{k=1,2} |g_k^{(\pm)}|^2 \left(\frac{n_k+1}{(\varepsilon_q - \varepsilon_{q+1}) - \omega_k} + \frac{n_k}{(\varepsilon_q - \varepsilon_{q+1}) + \omega_k}\right) \\
&+ \hbar|x_{q,q-1}|^2 \sum_{k=1,2} |g_k^{(\pm)}|^2 \left(\frac{n_k+1}{(\varepsilon_q - \varepsilon_{q-1}) - \omega_k} + \frac{n_k}{(\varepsilon_q - \varepsilon_{q-1}) + \omega_k}\right) \\
&+ \hbar|z_q|^2 \sum_{k=1,2} |g_k^{(\pm)}|^2 \left(-\frac{n_k+1}{\omega_k} + \frac{n_k}{\omega_k}\right) \\
=&\hbar \sum_{j=+1,-1} \sum_{k=1,2} |x_{q,q+j}|^2 |g_k^{(\pm)}|^2 \left(\frac{n_k+1}{(\varepsilon_q - \varepsilon_{q+j}) - \omega_k} + \frac{n_k}{(\varepsilon_q - \varepsilon_{q+j}) + \omega_k}\right) \\
&- \hbar|z_q|^2 \sum_{k=1,2} \frac{|g_k^{(\pm)}|^2}{\omega_k}.
\end{aligned} \tag{B.11}$$

Combining the expressions obtained in this way, leads to the total shift as shown in Eq. 3.53.

Appendix C

Moments of the Stripline Cavity Field in the Ground State

In this appendix, we calculate the moments of the field inside the stripline cavity introduced in Chapter 3, when the system is assumed to be in its ground state — namely expressions of the form $\langle 0|\Phi^k(x,t)|0\rangle$. These results are particularly useful when analyzing the effective spread of the field's wavefunction, and in Sec. 3.12 let us describe the validity of approximating the DC–SQUID as a linear, flux–dependent LC oscillator. In order to simplify the calculations, we follow the technique presented in [130].

In Seq.3.4 we calculated the expression for the flux–field inside the cavity as

$$\Phi(x,t) = \sum_n \sqrt{\frac{\hbar}{2\omega_n}} u_n(x)(a_n e^{-i\omega_n t} + a_n^\dagger e^{i\omega_n t}). \tag{C.1}$$

For convenience, let us define operators $A = \sum_n \sqrt{\frac{\hbar}{2\omega_n}} u_n(x) a_n e^{-i\omega_n t}$ and $A^\dagger = \sum_n \sqrt{\frac{\hbar}{2\omega_n}} u_n(x) a_n^\dagger e^{i\omega_n t}$, which allow us to describe the field in a more concise form, as[1]

$$\Phi(x,t) = A + A^\dagger. \tag{C.2}$$

Taking $|0\rangle = |0,0,\dots\rangle$, it is easy to see that

$$A|0\rangle = 0, \tag{C.3}$$

and therefore $\langle 0|A^\dagger = 0$. Furthermore, we can now define helpful commutation

---

[1] Our naming convention differers from the one used in [130].

relations. We note that since $[a_n, a^\dagger_{n'}] = \delta_{n,n'}$, we can write

$$\begin{aligned}[A, A^\dagger] &= \sum_n \sum_{n'} \frac{\hbar}{2} \frac{1}{\sqrt{\omega_n}} \frac{1}{\sqrt{\omega_{n'}}} u_n(x) u_{n'}(x) [a_n, a^\dagger_{n'}] \\ &= \sum_n \frac{\hbar}{2\omega_n} u_n^2(x),\end{aligned} \tag{C.4}$$

and hence

$$\begin{aligned}[\Phi, A^\dagger] &= [A + A^\dagger, A^\dagger] \\ &= \sum_n \frac{\hbar}{2\omega_n} u_n^2(x),\end{aligned} \tag{C.5}$$

Next, using the notation $\langle \bullet \rangle \equiv \langle 0 | \bullet | 0 \rangle$, and dropping the explicit x and t dependence for notational convenience, from Eq. C.3 it follows that

$$\begin{aligned}\langle \Phi \rangle &= \langle A + A^\dagger \rangle \\ &= 0.\end{aligned} \tag{C.6}$$

Similarity, using that fact that for two operators B and C we can write $BC = CB + [B, C]$, for the second moment, we have

$$\begin{aligned}\langle \Phi^2 \rangle &= \langle \Phi (A + A^\dagger) \rangle \\ &= \langle \Phi A \rangle + \langle \Phi A^\dagger \rangle \\ &= \langle A^\dagger \Phi \rangle + \langle [\Phi, A^\dagger] \rangle \\ &= \sum_n \frac{\hbar}{2\omega_n} u_n^2(x).\end{aligned} \tag{C.7}$$

A higher kth moment can be calculated noting that for two operators B and C, that satisfy $[B, C] = d$, with $d \in \mathbb{C}$, we have $[B^k, C] = k d B^{k-1}$. Hence

$$\begin{aligned}\langle \Phi^k \rangle &= \langle \Phi^{k-1} \Phi \rangle \\ &= \langle \Phi^{k-1} (A + A^\dagger) \rangle \\ &= \langle \Phi^{k-1} A^\dagger \rangle \\ &= \langle A^\dagger \Phi^{k-1} \rangle + \langle [\Phi^{k-1}, A^\dagger] \rangle \\ &= (k-1) \sum_n \frac{\hbar}{2\omega_n} u_n^2(x) \langle \Phi^{k-2} \rangle.\end{aligned} \tag{C.8}$$

This shows how the expression for kth moment depends on the value of the $(k-2)$th moment. In the case of k being odd, inductively, we can trace this result back to $k = 1$ and using Eq. C.6, conclude that all the odd moments will be necessarily zero. Mathematically we can write this as

$$\langle \Phi^{2k+1} \rangle = 0, \tag{C.9}$$

for $k = 0, 1, 2 \ldots$. In the case of even powers on the other hand, using Eq. C.8, and inductively tracing back to the result for the second moment shown in Eq. C.7, we see that

$$\begin{aligned} \langle \Phi^{2k} \rangle &= (2k-1)!! \langle \Phi^2 \rangle^k \\ &= (2k-1)!! \left(\sum_n \frac{\hbar}{2\omega_n} u_n^2(x) \right)^{2k}, \end{aligned} \tag{C.10}$$

for $k = 1, 2, \ldots$. In this last expression, the "!!" symbol represents the double factorial, which is defined as

$$n!! = \begin{cases} \prod_{k=1}^{n/2} 2k = n(n-2)(n-4)\ldots 2 & \text{if } n \text{ is even} \\ \prod_{k=1}^{(n+1)/2} (2k-1) = n(n-2)(n-4)\ldots 1 & \text{if } n \text{ is odd.} \end{cases} \tag{C.11}$$

Hence Eqs. C.9 and C.10 let us calculate the kth moment of the flux operator in the ground state of the filed, described by the normal modes $u_n(x)$.

Appendix D

Derivations of an Effective DC–SQUID Inductance

In this appendix we will discuss various ways of approximating the inductance of a DC–SQUID. It is well known that due to the Josephson relations [67], in a case of just a single Josephson junction, the inductance can be thought of as $L_{J0}/\cos\varphi$, with $L_{J0} = \Phi_0/2\pi I_0$, and φ a superconducting phase across the junction. Such inductance is clearly time dependent, however it is often useful to approximate it by simply taking the steady state value of φ — let us call it $\varphi^{\min}$. The value of $\varphi^{\min}$ depends on the strength of the biasing DC current that is passed through the junction and it can be calculated by minimizing the junction's potential energy. Such an approximation is typically valid in the limit of small excitations of the DC–SQUID, namely when $|\varphi| \ll 1$. An analogous treatment can be performed for a DC–SQUID, and in Chapter 2, it was shown to be useful during characterization of the various circuit parameters.

For the sake of concreteness, let us consider a single DC–SQUID shown in Fig.D.1a. Everything follows from the discussion from Chapter 2, and in particular Sec. 4.3, except we neglect all the "other" circuit components, and furthermore, for the sake of generality, assume that the DC–SQUID is driven by some biasing current I_{in} (in Sec.4.3, the AC signal excited the circuit through the input capacitor C_{in}, but no other biasing current was present). We label the flux nodes as 2, 4, and 5, to stay consistent with the previous discussion. We can use this setup to discuss three slightly different, but analogous ways of calculating the effective inductance of a DC–SQUID. The first way (Method 1) will review the discussion already presented in Sec. 4.3, which consists of reducing the system to a single degree of freedom and minimizing a 1D potential energy. In the second way (Method 2) we will use the fact that in the limit of the junctions preforming linearly, and small $\beta_L = L_g/L_{J0}$, it will be possible to decouple two degrees of freedom in the DC–SQUID potential, and hence obtain an effective inductance by only looking at a single degree that couples

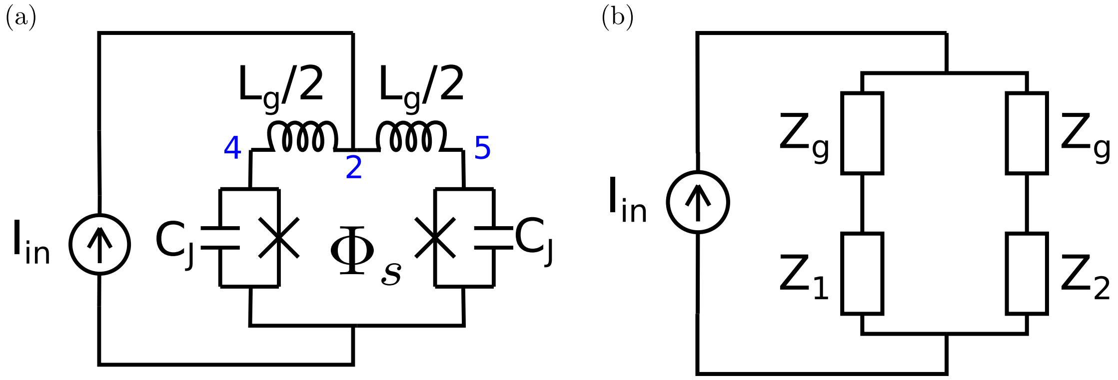

Figure D.1: (a) DC–SQUID driven by a current source. The flux nodes are labeled by numbers 2, 4 and 5 in order to stay consistent with Fig. 4.2 and the overall discussion in Sec. 4.3. (b) An equivalent circuit drawn in terms of impedances due to the Josephson and geometric inductances. See text for details.

to input current. Finally the last way (Method 3) will use standard circuit analysis techniques and combine all the involved impedances in Fourier space. We will conclude by providing a numerical comparison of the three methods just outlined.

D.1 Method 1

In this section we will review the results obtained in Sec. 4.3. There we started with the potential energy for the DC–SQUID in terms of three degrees of freedom, φ_2, φ_+, and φ_-, and given the fact that they evolve on different time scales, using a Born–Oppenheimer like treatment, we reduced the system and expressed the effective potential energy U_{eff} only in terms of φ_2, which in turn represents the total phase across the DC–SQUID. In Sec. 4.3 we assumed that there is no biasing DC current to be consistent with the experiment, but here, to preserve generality we can include the effects of having a nonzero I_{in} (see Fig. D.1a), which would result in an extra term $-\phi_0 I_{\text{in}}\varphi_2$ added to Eq. 4.5. While the resulting potential energy was shown to be still nonlinear in φ_2, at small excitations it could be expanded near φ_2 that minimized U_{eff}, namely φ_2^{min}, which we could calculate numerically (for a given applied flux ratio f_s). The last step was then just to conclude that this would let us write an effective inductance, which we called L_t, as

$$L_t = \phi_0^2 \left(\left. \frac{\partial^2 U_{\text{eff}}}{\partial \varphi_2^2} \right|_{\varphi_2 = \varphi_2^{\text{min}}} \right)^{-1}. \tag{D.1}$$

U_{eff} here is shown in detail in Eq. 4.5 and in what follows. Clearly by including higher orders corrections in β_L we could get a more accurate value.

D.2 Method 2

In this section we will provide an analogous treatment to what was shown in Sec. D.1, however we will start with a reduced potential energy of only two degrees of freedom – this kind of description is more common, particularly in circuits where the DC–SQUID is not shunted by other components. As was done in Chapter 4 for the full experimental circuit, we can write down the equations of motion of our simplified system consisting only of a DC–SQUID as

$$2C_J\phi_0\ddot{\varphi}_+ + 2I_0 \sin\varphi_+ \cos\varphi_- = I_{\text{in}} \tag{D.2}$$

$$2C_J\phi_0\ddot{\varphi}_- + 2I_0 \sin\varphi_- \cos\varphi_+ = \frac{4\phi_0}{L_g}\left(-\varphi_- + \pi f_s\right), \tag{D.3}$$

along with

$$I_{\text{in}} = \frac{4\phi_0}{L_g}\left(\varphi_2 - \varphi_+ + \pi f_s\right) \tag{D.4}$$

Once again we have taken the flux–phase relationship as $\Phi_i = \varphi_i\phi_0$, with $\phi_0 = \Phi_0/2\pi$ as well as $\varphi_\pm = (\varphi_4 \pm \varphi_5)/2$. f_s is the applied flux ratio Φ_s/Φ_0, with Φ_s representing the external flux through the DC–SQUID loop. It is worth stressing that while the equations of motion consist of three degrees of freedom, the dynamics of the DC–SQUID can be well understood by only considering φ_- and φ_+. This is because φ_2 is fully determined by I_b, φ_+ and φ_-, as can be easily observed from Eqs. D.2 and D.4. Let us then for now eliminate φ_2 and integrate Eqs. D.3 to obtain a potential energy. This leads to

$$\frac{U}{2E_J} = -I_b\varphi_+ - \cos\varphi_+ \cos\varphi_- + \frac{1}{\beta_L}\left(\pi f_s - \varphi_-\right)^2, \tag{D.5}$$

with $I_b = I_{\text{in}}/2I_0$. Temporarily, we will assume that I_{in} is a DC current, and therefore I_b is a constant.

Next, let us expand this expression around points associated with a minimum of U, namely φ_+^{min} and φ_-^{min}. Introducing translated variables $\bar{\varphi}_\pm = \varphi_\pm - \varphi_\pm^{\text{min}}$ and neglecting constant terms, lets us write an approximate potential energy U_{app}, as

$$\begin{aligned}\frac{U_{\text{app}}}{2E_J} = &\left(\frac{\beta_L}{2} + \cos\varphi_+^{\text{min}}\cos\varphi_-^{\text{min}}\right)\bar{\varphi}_-^2 + \frac{1}{2}\cos\varphi_+^{\text{min}}\cos\varphi_-^{\text{min}}\bar{\varphi}_+^2 \\ &+ \left(\frac{2}{\beta_L}(-\pi f_s + \varphi_-^{\text{min}}) + \cos\varphi_+^{\text{min}}\sin\varphi_-^{\text{min}} - \sin\varphi_+^{\text{min}}\sin\varphi_-^{\text{min}}\bar{\varphi}_+\right)\bar{\varphi}_- \\ &+ \left(\sin\varphi_+^{\text{min}}\cos\varphi_-^{\text{min}} - I_b\right)\bar{\varphi}_+.\end{aligned} \tag{D.6}$$

It is clear that in this form, the two degrees of freedom $\bar{\varphi}_+$ and $\bar{\varphi}_-$ are coupled.

We can however show that in the case of $|\varphi_-|, |\varphi_+| \ll 1$, which we have assumed to be true, when we expanded U in Eq. D.5, and only kept terms up to second order, and having $\beta_L \ll 1$, leads to these two degrees of freedom being approximately decoupled. Hence, we complete the square in $\bar{\varphi}_-$, which gives

$$\begin{aligned}\frac{U'_{\text{app}}}{2E_J} =&\frac{1}{2}\left(\cos\varphi_-^{\min}\cos\varphi_+^{\min} - \frac{\beta_L\sin^2\varphi_-^{\min}\sin^2\varphi_+^{\min}}{\beta_L\cos\varphi_-^{\min}\cos\varphi_+^{\min}+2}\right)\bar{\varphi}_+^2\\ &+\left(\cos\varphi_-^{\min}\sin\varphi_+^{\min} - I_b + \frac{\left(\beta_L\cos\varphi_+^{\min}\sin\varphi_-^{\min}+2\varphi_-^{\min}-2\pi f_s\right)}{\beta_L\cos\varphi_-^{\min}\cos\varphi_+^{\min}+2}\right)\bar{\varphi}_+\\ &+\left(\frac{\beta_L}{2}+\cos\varphi_+^{\min}\cos\varphi_-^{\min}\right)\bar{\varphi}_-'^2. \end{aligned} \tag{D.7}$$

Here we have introduced a new variable $\bar{\varphi}'_-$, which can be written as

$$\bar{\varphi}'_- =\bar{\varphi}_- - \frac{\beta_L\sin\varphi_-^{\min}(\bar{\varphi}_+\sin\varphi_+^{\min}-\cos\varphi_+^{\min})+2(\pi f_s-\varphi_-^{\min})}{\beta_L\cos\varphi_-^{\min}\cos\varphi_+^{\min}+2}. \tag{D.8}$$

While it clearly depends on $\bar{\varphi}_+$, it does so only weekly. Since $\beta_L \ll 1$, we can think of the variable $\bar{\varphi}_-$ as fast relative to $\bar{\varphi}_+$. Hence on the time scale of $\bar{\varphi}_-$ one can expect $\bar{\varphi}_+$ to be roughly constant. From Eqs. D.7 and D.8, it is clear that in this new uncoupled "frame", the $\bar{\varphi}_-$ gets a translation that depends on the "slow" $\bar{\varphi}_+$, while the degree of freedom $\bar{\varphi}_+$ sees a shift in its natural frequency. Hence after simplifying the potential further, we can now write down the effective inductance, associated with the $\bar{\varphi}_+$ (and hence φ_+) degree of freedom — let us call it L_+. It is simply the inverse of twice the coefficient of the $\bar{\varphi}_+^2$ multiplied by $2E_J$ in Eq. D.7. Therefore after simplifying we arrive at

$$L_+ =\frac{L_{J0}}{2}\frac{\beta_L\cos\varphi_-^{\min}\cos\varphi_+^{\min}+2}{\beta_L(\cos^2\varphi_-^{\min}+\cos^2\varphi_+^{\min}-1)+2\cos\varphi_-^{\min}\cos\varphi_+^{\min}} \tag{D.9}$$

Next, we need to account for the fact that the total voltage across the DC–SQUID is not $\phi_0\dot{\varphi}_+$, but instead $\phi_0\dot{\varphi}_2$. So far we have assumed that I_{in} is constant, but let us now treat it as consisting of a constant DC bias, as well as an AC component. Then differentiating Eq. D.4 with respect to time, and assuming that the applied flux is time–independent (which is consistent with the experiment), gives

$$\phi_0\dot{\varphi}_2 = \frac{L_g}{4}\dot{I}_{\text{in}} + \phi_0\dot{\varphi}_+. \tag{D.10}$$

We can now use the expression derived in Eq. D.9, to rewrite the above equation as

$$\begin{aligned}\phi_0 \dot{\varphi}_2 &= \frac{L_g}{4}\dot{I}_{\text{in}} + L_+ \dot{I}_{\text{in}} \\ &= \left(\frac{L_g}{4} + L_+\right)\dot{I}_{\text{in}} \\ &= L_{\text{eff}} \dot{I}_{\text{in}}.\end{aligned} \tag{D.11}$$

Hence we can define the effective inductance of a DC–SQUID to be

$$L_{\text{eff}} = \frac{L_g}{4} + \frac{L_{J0}}{2} \frac{\beta_L \cos\varphi_-^{\min} \cos\varphi_+^{\min} + 2}{\beta_L(\cos^2\varphi_-^{\min} + \cos^2\varphi_+^{\min} - 1) + 2\cos\varphi_-^{\min}\cos\varphi_+^{\min}}. \tag{D.12}$$

Lastly, since many DC–SQUID experiments are operated in the limit where $\beta_L \ll 1$, as was the case here, it is useful to expand the effective inductance in powers of β_L. So for example, neglecting terms of order $\mathcal{O}\left(\beta_L^2\right)$ or higher, leads to

$$L_{\text{eff}} = \frac{L_g}{4} + \frac{L_{J0}}{2\cos\varphi_-^{\min}\cos\varphi_+^{\min}} + \beta_L \frac{L_{J0}\tan^2\varphi_-^{\min}\tan^2\varphi_+^{\min}}{4}. \tag{D.13}$$

A variation of this form is used in different publications — often in fact only the second term is considered as one takes the limit of $\beta_L = L_g/L_{J0} \to 0$ [118, 119]. Furthermore while we have assumed that $\varphi_\pm^{\min}$ are "exact" (calculated by a numerical minimization), in some cases it may be useful to simply use an approximation, which can be obtained through informative guesses. For example in the case where the biasing DC current through the DC–SQUID is zero, and in the limit of $L_g = 0$, one can approximate $\varphi_-^{\min}$ as $f_s\pi$, and set $\varphi_+^{\min} = 0$, which lets us rewrite Eq.D.13 as $L_{J0}/2\cos(f_s\pi)$. Therefore in this limit, the DC–SQUID behaves like a single junction with an applied, flux–controlled critical current.

D.3 Method 3

In this section, let us briefly outline a calculation of the effective inductance using standard linear circuit analysis techniques, where we simply add impedances in Fourier space. In the limit of small junction capacitances C_J, we can neglect them, and using Josephson relations [67] treat the effective inductance of the ith junction as $L_i = L_{J0}/\cos\varphi_i^{\min}$, with φ_i representing the phase across the ith junction, as before (here the label i is 4 or 5). In general φ_i is time dependent but here we will assume we take a steady state value (or the minimum of the corresponding potential energy). In the limit of junctions behaving linearly, this lets us redraw our DC–SQUID circuit as four individual impedances arranged as shown in Fig. D.1b. The

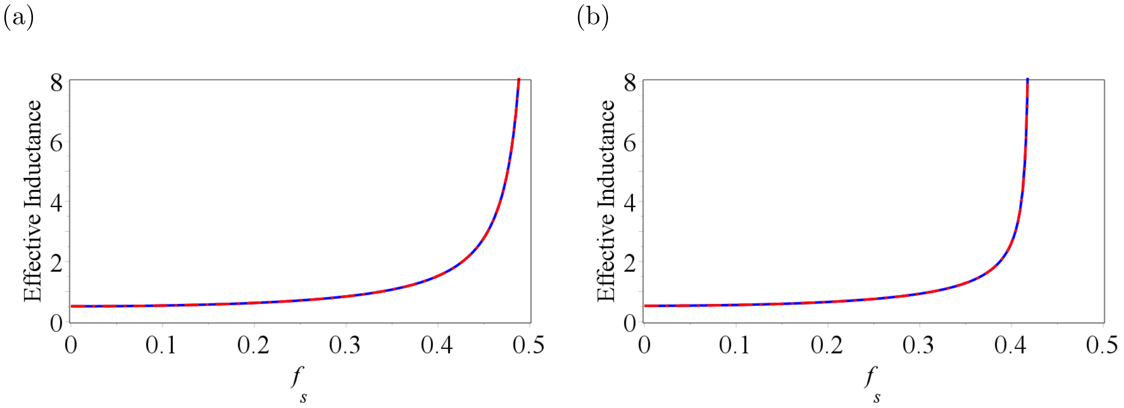

Figure D.2: Effective inductance of a DC–SQUID calculated via Method 1 (red curve) and Methods 2 and 3 (blue curve) in units of L_{J0} and as a function of the flux ratio f_s. The parameter β_L is taken as 0.05, which is consistent with the experiment discussed in Chapter 4. Furthermore, the plot in (a) uses the current ratio $I_b = 0.0$ as in the experiment, while (b) shows results for $I_b = 0.25$. We observe good agreement between the various methods.

total impedance of the whole circuit, can therefore be written as

$$Z_{\text{eff}} = (Z_1 + Z_g)||(Z_2 + Z_g), \tag{D.14}$$

where $||$ represents that the impedances are to be taken in parallel, $Z_g = i\omega L_g/2$, and finally $Z_i = i\omega L_i$. As before, applying a change of variables $\varphi_\pm = (\varphi_4 \pm \varphi_5)/2$ (and assuming that this holds for their minima as well) and simplifying, leads to

$$Z_{\text{eff}} = i\omega L_{\text{eff}}, \tag{D.15}$$

where L_{eff} is identical to the expression shown in Eq. D.12. As in Sec. D.2, in order to obtain a numerical value for this expression, one would have to either numerically minimize Eq. D.5 or use other means to arrive at some estimates for the steady steady state values of φ_+ and φ_-. Hence we conclude, as might be expected, these various approaches to deriving an approximate effective inductance, let us arrive at equivalent answers.

D.4 Comparison

As a last step, we can numerically compare the results from Sections D.1, as well as D.2 and D.3. Let us reiterate that while the expressions for the effective inductance from Sections D.2 and D.3 agree exactly with each other, the variation from Sec. D.1 is slightly different. This is because there, we have estimated the values of φ_+ and

φ_- that correspond to the minimum of potential energy via a Taylor expansion and not assumed them to be “exact” (i.e. obtained via a numerical minimization). Nevertheless, the resulting values of L_{eff} agree quite well for the parameters used in the experiment, as long as we keep terms at least up to first order in β_L. Fig. D.2 shows a couple of plots that compare the effective inductance calculated via Method 1 (red curve) and Methods 2 and 3 (blue curve) in units of L_{J0} and as a function of the flux ratio f_s. In both plots, the parameter β_L is taken as 0.05, as in the experiment outlined in Chapter 4. The plot in (a) uses the current ratio $I_b = 0.0$, while in (b) shows results for $I_b = 0.25$. We observe good general agreement between all the methods discussed.

Appendix E

Numerical Integration of the Langevin Equations

In chapter 4 we studied the transient response of a DC–SQUID oscillator circuit at finite temperature. We derived an effective set of stochastic differential equations (Langevin equations) [80, 102, 121] that govern the behavior of our system. In this appendix, we briefly outline how these equations were numerically integrated. We stress that the material shown here is meant to complement that discussion, and we point the reader to Sec. 4.3 for definitions of parameters and the general problem setup.

Through elimination of the fast degrees of freedom, in Sec. 4.3 we wrote down the equations of motion, in a vector form, as

$$\phi_0 \mathbf{C}\ddot{\vec{\varphi}} + \phi_0 \mathbf{R^{-1}}\dot{\vec{\varphi}} + \frac{1}{\phi_0}\vec{\nabla}_\varphi U_{\text{eff}} + \mathbf{N}\vec{n} + \vec{I}_{\text{dr}} = 0. \tag{E.1}$$

Here $\vec{\varphi} = (\varphi_1, \varphi_2, \varphi_3)^T$, $\vec{\nabla}_\varphi = (\partial/\partial\varphi_1, \partial/\partial\varphi_2, \partial/\partial\varphi_3)^T$, $\vec{I}_{\text{dr}} = (-V_{\text{in}}/R_z, 0, 0)^T$ and $\vec{n} = (n_1, n_2, n_3)^T$ is a vector of Gaussian random variables representing white noise as described in Sec. 4.3. The matrices corresponding to $\mathbf{C}$ and $\mathbf{R^{-1}}$ can be written as

$$\mathbf{C} = \begin{pmatrix} C_{\text{in}} & -C_{\text{in}} & 0 \\ -C_{\text{in}} & C_\Sigma & -C_{\text{out}} \\ 0 & -C_{\text{out}} & C_{\text{out}} \end{pmatrix}, \mathbf{R^{-1}} = \begin{pmatrix} \frac{1}{R_z} & 0 & 0 \\ 0 & \frac{1}{R_t} & 0 \\ 0 & 0 & \frac{1}{R_z} \end{pmatrix}, \tag{E.2}$$

and $\mathbf{N}$ as simply

$$\mathbf{N} = \sqrt{2k_B T \mathbf{R^{-1}}}. \tag{E.3}$$

In order to solve the system shown in Eq. E.1 numerically, we first transform it into a system of first order equations. This is done by introducing

$$\vec{X} = \begin{pmatrix} X_1 \\ X_2 \\ X_3 \\ X_4 \\ X_5 \\ X_6 \end{pmatrix} = \begin{pmatrix} \varphi_1 \\ \dot{\varphi}_1 \\ \varphi_2 \\ \dot{\varphi}_2 \\ \varphi_3 \\ \dot{\varphi}_3 \end{pmatrix}. \tag{E.4}$$

Next, we write it as a *standard form* of a multivariate Langevin equation [51, 52], which reads

$$\vec{X}(t+dt) = \vec{X}(t) + \vec{\mu}dt + \boldsymbol{\sigma}\vec{N}\sqrt{dt}, \tag{E.5}$$

with

$$\vec{\mu} = \frac{1}{C_t}\begin{pmatrix} X_2 \\ -\frac{(C_{\text{in}}+C_t)X_2}{C_{\text{in}}R_z} - \frac{2\cos(\pi f_s)\sin(\pi f_s+X_3)}{L_J} - \beta_L\frac{\sin(4\pi f_s+2X_3)+\sin(2X_3)}{2L_J} - \frac{X_4}{R_t} - \frac{X_6}{R_z} + \frac{(C_{\text{in}}+C_t)V_{\text{in}}}{\phi_0 C_{\text{in}}R_z} \\ X_4 \\ -\frac{X_2}{R_z} - \frac{2\cos(\pi f_s)\sin(\pi f_s+X_3)}{L_J} - \beta_L\frac{\sin(4\pi f_s+2X_3)+\sin(2X_3)}{2L_J} - \frac{X_4}{R_t} - \frac{X_6}{R_z} + \frac{V_{\text{in}}}{\phi_0 R_z} \\ X_6 \\ -\frac{X_2}{R_z} - \frac{2\cos(\pi f_s)\sin(\pi f_s+X_3)}{L_J} - \beta_L\frac{\sin(4\pi f_s+2X_3)+\sin(2X_3)}{2L_J} - \frac{X_4}{R_t} - \frac{(C_t+C_{\text{out}})X_6}{C_{\text{out}}R_z} + \frac{V_{\text{in}}}{\phi_0 R_z} \end{pmatrix}, \tag{E.6}$$

and

$$\boldsymbol{\sigma} = -\frac{\sqrt{2k_BT}}{\phi_0 C_t}\begin{pmatrix} 0 & 0 & 0 & 0 & 0 & 0 \\ 0 & \frac{(C_{\text{in}}+C_t)}{C_{\text{in}}\sqrt{R_z}} & 0 & \frac{1}{\sqrt{R_t}} & 0 & \frac{1}{\sqrt{R_z}} \\ 0 & 0 & 0 & 0 & 0 & 0 \\ 0 & \frac{1}{\sqrt{R_z}} & 0 & \frac{1}{\sqrt{R_t}} & 0 & \frac{1}{\sqrt{R_z}} \\ 0 & 0 & 0 & 0 & 0 & 0 \\ 0 & \frac{1}{\sqrt{R_z}} & 0 & \frac{1}{\sqrt{R_t}} & 0 & \frac{(C_{\text{out}}+C_t)}{C_{\text{out}}\sqrt{R_z}} \end{pmatrix}. \tag{E.7}$$

$\vec{N}$ represents a vector of temporally uncorrelated unit normal variables, with $N_i \in \mathcal{N}(0,1)$. The form of E.5 is particularly convenient, since it is presented as an update formula for the random variables described by $\vec{X}(t)$. In other words, it tells us how $\vec{X}(t)$ changes as we increase time by a small increment dt. Such an update formula can be easily programmed in a computer[1]. The results presented throughout chapter 4, are calculated with Maple, which uses the open source QuantLib library (version 0.3.11 as of this writing) implementation of the integration procedure[2].

---

[1] The method of directly using the update formula E.5 to generate single realizations of $\vec{X}(t)$ by splitting the time range of of interest into small time increments dt and generating a sample of random variables described by $\vec{N}$ at each time step, is often called the *Euler–Maruyama method.*

[2] At the initial stages of this project, some of the results were also obtained using a direct

In our simulations we chose the initial conditions to satisfy

$$\vec{X}(0) = \begin{pmatrix} 0 \\ 0 \\ -\pi f_s \\ 0 \\ 0 \\ 0 \end{pmatrix}. \tag{E.8}$$

This is a convenient choice as it sets the φ_2 (or X_3) near the potential energy minimum[3]. We then let the system thermalize by evolving Eq. E.5 without an external drive present, with only the thermal noise influencing the evolution. In the final step, one of the input pulses described by Eqs. 4.25 or 4.26 is applied, which in turn excites the system and prodcues rigndown oscillations.

The simulations are repeated many times to gather statistics about trajectories of individual realizations, which are later averaged. For example, the average of X_6 (multiplied by ϕ_0) corresponds to the circuit's output voltage and hence can be compared to the data that was measured in the Syracuse experiment.

---

implementation of Eq. E.5.

[3] It is not exactly at the minimum, due to the fact that β_L is small but not exactly zero.

Appendix F

Coherent State Evolution of a Decaying Harmonic Oscillator Coupled to a Qubit

In this appendix, we calculate the time dependent evolution of the coherent states of a harmonic oscillator decaying to its environment at a rate κ and coupled to a qubit. The results of this calculation are used in Sec. 5.5. We closely follow the procedure used in [47]. The key difference between our discussion and the one presented in [47] is the Hamiltonian — in the paper, it is dispersive and the qubit couples to the photon number operator $a^\dagger a$, whereas in our case, the qubit couples to oscillator displacement operator $a^\dagger + a$ instead.

We consider a special case of the Hamiltonian shown in Sec. 5.3, with $\Delta = 0$, namely

$$H = \hbar\Omega a^\dagger a + \frac{\hbar\epsilon}{2}\sigma_z + \hbar\gamma\sigma_z(a^\dagger + a) \tag{F.1}$$

where ϵ and Ω are the frequencies of the qubit and oscillator respectively, and γ the coupling between the two. We further assume that the evolution of our system is subject to a Lindblad master equation

$$\dot{\rho}(t) = -\frac{i}{\hbar}[H, \rho(t)] + \kappa\mathcal{D}[a]\rho(t), \tag{F.2}$$

with

$$\mathcal{D}[a]\rho(t) = a\rho a^\dagger + \frac{1}{2}\left(a^\dagger a\rho(t) + \rho(t)a^\dagger a\right), \tag{F.3}$$

and κ representing the decay rate out of the oscillator.

We begin by noting that we can rewrite the density matrix $\rho(t)$ as

$$\rho(t) = \sum_{\substack{i=e,g \\ j=e,g}} \rho_{ij}(t)|i\rangle\langle j|, \tag{F.4}$$

where e and g are the indices of excited and ground states of the qubit respectively. We stress that each $\rho_{ij}(t)$ is an operator in a Hilbert space of the oscillator only, not the qubit, and it is precisely the evolution that we wish to calculate. Substituting Eq. F.4 into the master equation F.2, leads to four differential equations for each of ρ_{ij} (neglecting explicit time dependence for the sake of brevity)

$$\dot{\rho}_{ee} = -i\Omega[a^\dagger a, \rho_{ee}] - ig[a^\dagger + a, \rho_{ee}] + \kappa\mathcal{D}[a]\rho_{ee} \tag{F.5}$$

$$\dot{\rho}_{gg} = -i\Omega[a^\dagger a, \rho_{gg}] + ig[a^\dagger + a, \rho_{gg}] + \kappa\mathcal{D}[a]\rho_{gg} \tag{F.6}$$

$$\dot{\rho}_{eg} = -i\Omega[a^\dagger a, \rho_{eg}] - i\epsilon\rho_{eg} - ig[a^\dagger + a, \rho_{eg}] + \kappa\mathcal{D}[a]\rho_{eg} \tag{F.7}$$

$$\dot{\rho}_{ge} = +i\Omega[a^\dagger a, \rho_{ge}] + i\epsilon\rho_{ge} + ig[a^\dagger + a, \rho_{ge}] + \kappa\mathcal{D}[a]\rho_{ge}. \tag{F.8}$$

Next, following [47], we introduce a positive–P representation [84] defined as

$$\rho_{ij} = \int d^2\alpha \int d^2\beta \Lambda P_{ij}(\alpha, \beta) \tag{F.9}$$

where

$$\Lambda = \frac{|\alpha\rangle\langle\beta^*|}{\langle\beta^*|\alpha\rangle}. \tag{F.10}$$

Each of α and β is a complex number, hence the integral in Eq. F.9 is four dimensional. The positive–P representation is particularly useful in this case (as opposed to say Winger representation [84]), as we will be able to write P_{ij} in terms of δ–functions — this is because we expect the degrees of freedom of the oscillator to evolve like a time dependent coherent states [49].

The next step involves substituting Eq. F.9 into Eqs. F.5 – F.8. Using the following identities

$$\begin{aligned} a|\alpha\rangle &= \alpha|\alpha\rangle, & a^\dagger|\alpha\rangle &= (\partial_\alpha + \alpha^*/2)|\alpha\rangle \\ \langle\beta^*|a^\dagger &= \beta\langle\beta^*|, & \langle\beta^*|a &= (\partial_\beta + \beta/2)\langle\beta^*|, \end{aligned} \tag{F.11}$$

one can show that

$$
\begin{aligned}
[a^\dagger, \rho_{ij}] &= -\partial_\alpha P_{ij} && \text{(F.12)}\\
[a, \rho_{ij}] &= \partial_\beta P_{ij} && \text{(F.13)}\\
[a^\dagger + a, \rho_{ij}] &= -\partial_\alpha P_{ij} + \partial_\beta P_{ij} && \text{(F.14)}\\
[a^\dagger a, \rho_{ij}] &= -\alpha \partial_\alpha P_{ij} + \beta \partial_\beta P_{ij}, && \text{(F.15)}
\end{aligned}
$$

which then lets us rewrite Eqs. F.5 – F.8 in terms of P_{ij} as

$$
\begin{aligned}
\dot{P}_{ee} &= \partial_\alpha \left(i\Omega\alpha + ig + \frac{k\alpha}{2} \right) P_{ee} + \partial_\beta \left(-i\Omega\beta - ig + \frac{\kappa\beta}{2} \right) P_{ee} && \text{(F.16)}\\
\dot{P}_{gg} &= \partial_\alpha \left(i\Omega\alpha - ig + \frac{k\alpha}{2} \right) P_{gg} + \partial_\beta \left(-i\Omega\beta + ig + \frac{\kappa\beta}{2} \right) P_{gg} && \text{(F.17)}\\
\dot{P}_{eg} &= \partial_\alpha \left(i\Omega\alpha + ig + \frac{k\alpha}{2} \right) P_{eg} + \partial_\beta \left(-i\Omega\beta - ig + \frac{\kappa\beta}{2} \right) P_{eg} - i\epsilon P_{eg} && \text{(F.18)}\\
\dot{P}_{eg} &= \partial_\alpha \left(-i\Omega\alpha - ig + \frac{k\alpha}{2} \right) P_{eg} + \partial_\beta \left(+i\Omega\beta + ig + \frac{\kappa\beta}{2} \right) P_{eg} + i\epsilon P_{eg}. && \text{(F.19)}
\end{aligned}
$$

These equations can be solved, by making a simple ansatz [47]

$$
P_{ii} = \delta^2[\alpha - \alpha_i(t)]\delta^2[\beta - \alpha_i^*(t)] \tag{F.20}
$$

and assuming $c_{ij}(t)$ are time–dependent functions,

$$
P_{ij} = c_{ij}(t)\delta^2[\alpha - \alpha_i(t)]\delta^2[\beta - \alpha_j^*(t)], \tag{F.21}
$$

with $i \neq j$. Each $\alpha_i(t)$, for $i, j \in \{e, g\}$, describes the very coherent states we want to calculate — they tell us how the degrees of freedom of the oscillator evolve in time.

We can substitute Eqs. F.20 and F.21 into Eqs. F.16 – F.19 and simplify, which finally leads to expressions

$$
\begin{aligned}
\dot{\alpha}_e(t) =& -i\gamma - \left(\Omega + \frac{\kappa}{2} \right) \alpha_e(t) && \text{(F.22)}\\
\dot{\alpha}_g(t) =& i\gamma - \left(\Omega + \frac{\kappa}{2} \right) \alpha_g(t), && \text{(F.23)}
\end{aligned}
$$

with easily obtainable solutions

$$
\alpha_j(t) = \alpha_j^s + \left(\alpha_j(0) - \alpha_j^s \right) \exp\left(-i\left(\Omega + \gamma \right) t - \frac{\kappa t}{2} \right) \tag{F.24}
$$

for $j \in \{e, g\}$, and with α_j^s representing steady state solutions where $\alpha_e^s = -\frac{2i\gamma}{2i\Omega + \kappa}$

and $\alpha_g^s = -\alpha_e^s$. Hence, using Eq. F.9 along with Eq. F.24 gives the qubit–state dependent evolution of the oscillator, subject to the master equation F.2.

References

[1] Alhambra, A. M., Kempf, A., and Martin-Martinez, E. Casimir forces on atoms in optical cavities. *arXiv preprint arXiv:1311.7619* (2013).

[2] Bardeen, J., Cooper, L. N., and Schrieffer, J. R. Theory of superconductivity. *Phys. Rev. 108*, 5 (1957), 1175–1204.

[3] Barends, R., Kelly, J., Megrant, A., Veitia, A., Sank, D., Jeffrey, E., White, T., Mutus, J., Fowler, A., Campbell, B., et al. Superconducting quantum circuits at the surface code threshold for fault tolerance. *Nature 508*, 7497 (2014), 500–503.

[4] Ben-Jacob, E., Bergman, D., Imry, Y., Matkowsky, B., and Schuss, Z. Thermal activation from the fluxoid and the voltage states of dc squids. *Journal of applied physics 54*, 11 (1983), 6533–6542.

[5] Bethe, H. A. The electromagnetic shift of energy levels. *Physical Review 72*, 4 (1947), 339–341.

[6] Bhupathi, P., Groszkowski, P., DeFeo, M., Ware, M., Wilhelm, F. K., and Plourde, B. Transient dynamics of a superconducting nonlinear oscillator. *arXiv preprint arXiv:1504.06883* (2015).

[7] Blais, A., Huang, R.-S., Wallraff, A., Girvin, S., and Schoelkopf, R. Cavity quantum electrodynamics for superconducting electrical circuits: An architecture for quantum computing. *Phys. Rev. A 69* (2004), 062320.

[8] Bloch, F. Generalized theory of relaxation. *Phys. Rev. 105* (1957), 1206.

[9] Boissonneault, M., Gambetta, J. M., and Blais, A. Dispersive regime of circuit qed: Photon-dependent qubit dephasing and relaxation rates. *Physical Review A 79*, 1 (2009), 013819.

[10] Bouchiat, V., et P. Joyez, D. V., Esteve, D., and Devoret, M. Quantum coherence with a single Cooper pair. *Physica Scripta T76* (1998), 165.

[11] Boulant, N., Ithier, G., Meeson, P., Nguyen, F., Vion, D., Esteve, D., Siddiqi, I., Vijay, R., Rigetti, C., Pierre, F., and Devoret, M. Quantum nondemolition readout using a Josephson bifurcation amplifier. *Phys. Rev. B 76*, 1 (2007), 014525.

[12] Braginsky, V., Khalili, F. Y., and Thorne, K. *Quantum Measurement.* Cambridge University Press, Cambridge, 1995.

[13] Bressi, G., Carugno, G., Onofrio, R., and Ruoso, G. Measurement of the casimir force between parallel metallic surfaces. *Physical review letters 88*, 4 (2002), 041804.

[14] Breuer, H., and Petruccione, F. *The theory of open quantum systems.* Oxford University Press, USA, 2002.

[15] Brune, M., Nussenzveig, P., Schmidt-Kaler, F., Bernardot, F., Maali, A., Raimond, J., and Haroche, S. From lamb shift to light shifts: vacuum and subphoton cavity fields measured by atomic phase sensitive detection. *Physical review letters 72*, 21 (1994), 3339.

[16] Burkard, G., Koch, R. H., and DiVincenzo, D. P. Multilevel quantum description of decoherence in superconducting qubits. *Physical Review B 69*, 6 (2004), 064503.

[17] Caldeira, A., and Leggett, A. Quantum tunneling in a dissipative system. *Ann. Phys. (NY) 149* (1983), 374.

[18] Carmichael, H. *An open systems approach to quantum optics.* Springer, Berlin, 1993.

[19] Casimir, H., and Polder, D. The influence of retardation on the london-van der waals forces. *Physical Review 73*, 4 (1948), 360.

[20] Casimir, H. B. On the attraction between two perfectly conducting plates. In *Proc. K. Ned. Akad. Wet* (1948), vol. 51, p. 150.

[21] Castellanos-Beltran, M., Irwin, K., Hilton, G., Vale, L., and Lehnert, K. Amplification and squeezing of quantum noise with a tunable josephson metamaterial. *Nat. Phys. 4* (2008), 929.

[22] Chiorescu, I., Bertet, P., Semba, K., Nakamura, Y., Harmans, C. J. P. M., and J. E. Mooij, J. E. Coherent dynamics of a flux qubit coupled to a harmonic oscillator. *Nature 431* (2004), 159.

[23] Chow, J. M., Gambetta, J. M., Magesan, E., Abraham, D. W., Cross, A. W., Johnson, B., Masluk, N. A., Ryan, C. A., Smolin, J. A., Srinivasan, S. J., et al. Implementing a strand of a scalable fault-tolerant quantum computing fabric. *Nature communications 5* (2014).

[24] Chuang, I. L., and Nielsen, M. A. Prescription for experimental determination of the dynamics of a quantum black box. *Journal of Modern Optics 44*, 11-12 (1997), 2455–2467.

[25] Clarke, J. Squids: Then and now. *International Journal of Modern Physics B 24*, 20n21 (2010), 3999–4038.

[26] Clarke, J., and Braginski, A. I. *The SQUID Handbook: Fundamentals and Technology of SQUIDs and SQUID Systems Vol. I.* Wiley, Weinheim, 2004.

[27] Claudon, J., Fay, A., Hoskinson, E., and Buisson, O. Nanosecond quantum state detection in a current-biased dc SQUID. *Phys. Rev. B 76* (2007), 024508.

[28] de Gennes, P. *Superconductivity of metals and alloys.* Benjamin, N.Y., 1966.

[29] Debye, P. Interference of röntgen rays and heat motions. *Ann. Phys 43* (1914), 49–95.

[30] DeFeo, M. P., Bhupathi, P., Yu, K., Heitmann, T. W., Song, C., McDermott, R., and Plourde, B. L. T. Microstrip superconducting quantum interference device amplifiers with submicron josephson junctions: Enhanced gain at gigahertz frequencies. *Appl. Phys. Lett. 97* (2010), 092507.

[31] DeFeo, M. P., and Plourde, B. L. T. Superconducting microstrip amplifiers with sub-kelvin noise temperature near 4ghz. *Applied Physics Letters 101*, 5 (2012), –.

[32] Devoret, M. Quantum fluctuations in electrical circuits. In *Quantum Fluctuations* (Amsterdam, 1995), no. LXIII in Les Houches Session, Elsevier, p. 351.

[33] Dolan, G. J. Offset masks for lift-off photoprocessing. *Appl. Phys. Lett. 31* (1977), 337–339.

[34] Dorf, R. C., and Svoboda, J. A. *Introduction to electric circuits.* John Wiley & Sons, 2010.

[35] Drung, D., Assmann, C., Beyer, J., Kirste, A., Peters, M., Ruede, F., and Schurig, T. Highly sensitive and easy-to-use squid sensors. *Applied Superconductivity, IEEE Transactions on 17*, 2 (2007), 699–704.

[36] Egger, D. J., and Wilhelm, F. K. Multimode circuit quantum electrodynamics with hybrid metamaterial transmission lines. *Physical review letters 111*, 16 (2013), 163601.

[37] Einstein, A., and Stern, O. Einige argumente für die annahme einer molekularen agitation beim absoluten nullpunkt. *Annalen der Physik 345*, 3 (1913), 551–560.

[38] Elizalde, E., and Romeo, A. Essentials of the casimir effect and its computation. *Am. J. Phys 59*, 8 (1991), 711–719.

[39] Feynman, R. Simulating physics with computers. *International Journal of Theoretical Physics 21* (1981), 467.

[40] Feynman, R. P. Forces in molecules. *Physical Review 56*, 4 (1939), 340.

[41] Feynman, R. P. Space-time approach to non-relativistic quantum mechanics. *Reviews of Modern Physics 20*, 2 (1948), 367.

[42] Fowler, A. G., Thompson, W. F., Yan, Z., Stephens, A. M., Plourde, B. L. T., and Wilhelm, F. K. Long-range coupling and scalable architecture for superconducting flux qubits. *Phys. Rev. B 76* (2007), 174507.

[43] Fragner, A., Göppl, M., Fink, J., Baur, M., Bianchetti, R., Leek, P., Blais, A., and Wallraff, A. Resolving vacuum fluctuations in an electrical circuit by measuring the lamb shift. *Science 322*, 5906 (2008), 1357–1360.

[44] Friedman, J. R., Patel, V., Chen, W., Tolpygo, S., and Lukens, J. E. Quantum superposition of distinct macroscopic states. *nature 406*, 6791 (2000), 43–46.

[45] Fulling, S., and Davies, P. Radiation from a moving mirror in two dimensional space-time: conformal anomaly. *Proceedings of the Royal Society of London. A. Mathematical and Physical Sciences 348*, 1654 (1976), 393–414.

[46] Gambetta, J., Blais, A., Boissonneault, M., Houck, A., Schuster, D., and Girvin, S. Quantum trajectory approach to circuit QED: Quantum jumps and the Zeno effect. *Phys. Rev. A 77*, 1 (2008), 12112.

[47] Gambetta, J., Blais, A., Schuster, D. I., Wallraff, A., Frunzio, L., Majer, J., Devoret, M. H., Girvin, S. M., and Schoelkopf, R. J. Qubit-photon interactions in a cavity: Measurement-induced dephasing and number splitting. *Physical Review A 74*, 4 (2006), 042318.

[48] García-Ripoll, J. J., Peropadre, B., and De Liberato, S. Light-matter decoupling and a^2 term detection in superconducting circuits. *arXiv preprint arXiv:1410.7785* (2014).

[49] Gardiner, C., and Zoller, P. *Quantum Noise. A Handbook of Markovian and Non-Markovian Quantum Stochastic Methods with Applications to Quantum Optics*. Springer series in synergetics. Springer, Berlin, 1999.

[50] Gay, F., Piquemal, F., and Geneves, G. Ultralow noise current amplifier based on a cryogenic current comparator. *Review of Scientific Instruments 71*, 12 (2000), 4592–4595.

[51] Gillespie, D. T. The mathematics of brownian motion and johnson noise. *American Journal of Physics 64*, 3 (1996), 225–239.

[52] Gillespie, D. T. The multivariate langevin and fokker–planck equations. *American Journal of Physics 64*, 10 (1996), 1246–1257.

[53] Grønbech-Jensen, N., Castellano, M., Chiarello, F., Cirillo, M., Cosmelli, C., Filippenko, L., Russo, R., and Torrioli, G. Microwave-induced thermal escape in josephson junctions. *Physical review letters 93*, 10 (2004), 107002.

[54] Groszkowski, P., Fowler, A. G., Motzoi, F., and Wilhelm, F. K. Tunable coupling between three qubits as a building block for a superconducting quantum computer, Feb. 2011.

[55] Grover, L. Quantum mechanics helps in searching for a needle in a haystack. *Proceedings of the 28'th Annual ACM Symposium on the Theory of Computing 79* (1997), 325.

[56] Han, S., Lapointe, J., and Lukens, J. Effect of a two-dimensional potential on the rate of thermally induced escape over the potential barrier. *Physical Review B 46*, 10 (1992), 6338.

[57] Hanggi, P., Talkner, P., and Borkovec, M. Reaction-rate theory: fifty years after kramers. *Rev. Mod. Phys. 62* (1990), 252.

[58] Hatridge, M., Vijay, R., Slichter, D., Clarke, J., and Siddiqi, I. Dispersive magnetometry with a quantum limited squid parametric amplifier. *Phys. Rev. B 83* (2011), 134501.

[59] Heinzen, D., Childs, J., Thomas, J., and Feld, M. Enhanced and inhibited visible spontaneous emission by atoms in a confocal resonator. *Physical review letters 58*, 13 (1987), 1320.

[60] Heisenberg, W. Über quantentheoretische Umdeutung kinematischer und mechanischer Beziehungen. *Zeitschrift fur Physik 33* (Dec. 1925), 879–893.

[61] Hellmann, H. Einfuhrung in die quantumchemie. *Franz Deutsche, Leipzig* (1937), 285.

[62] Hover, D., Chen, Y.-F., Ribelli, G., Zhu, S., Sendelbach, S., and McDermott, R. Superconducting low-inductance undulatory galvanometer microwave amplifier. *Appl. Phys. Lett. 10* (2012), 063503.

[63] Jacobs, K. *Quantum Measurement Theory and its Applications.* Cambridge University Press, 2014.

[64] Johansson, J., Johansson, G., and Nori, F. Optomechanical-like coupling between superconducting resonators. *Physical Review A 90*, 5 (2014), 053833.

[65] Johansson, J., Johansson, G., Wilson, C., and Nori, F. Dynamical casimir effect in superconducting microwave circuits. *Physical Review A 82*, 5 (2010), 052509.

[66] Johansson, J., Nation, P., and Nori, F. Qutip 2: A python framework for the dynamics of open quantum systems. *Computer Physics Communications 184*, 4 (2013), 1234–1240.

[67] Josephson, B. Possible new effects in superconductive tunneling. *Phys. Lett. 1*, 7 (1962), 251.

[68] Kamon, M., Tsuk, M. J., and White, J. Fasthenry: A multipole-accelerated 3-d inductance extraction program. In *Design Automation Conference* (1993), pp. 678–683.

[69] Kaye, P., Laflamme, R., and Mosca, M. An introduction to quantum computing, 2007.

[70] Kitaev, A. Quantum computations: algorithms and error correction. *Russian Mathematical Surveys 52*, 6 (1997), 1191–1249.

[71] Kittel, C., McEuen, P., and McEuen, P. *Introduction to solid state physics*, vol. 8. Wiley New York, 1976.

[72] Koch, J., Yu, T., Gambetta, J., Houck, A. A., Schuster, D. I., Majer, J., Blais, A., Devoret, M. H., Girvin, S. M., and Schoelkopf, R. J. Charge-insensitive qubit design derived from the cooper pair box. *Phys. Rev. A 76*, 4 (2007), 042319.

[73] Koch, R., DiVincenzo, D., and Clarke, J. Model for 1/f flux noise in squids and qubits. *Physical Review Letters 98*, 26 (2007), 267003.

[74] Kramers, H. A. Brownian motion in a field of force and the diffusion model of chemical reactions. *Physica 7*, 4 (1940), 284–304.

[75] Kraus, K. *States, effects and operations.* Springer, 1983.

[76] Lalumière, K., Sanders, B. C., van Loo, A. F., Fedorov, A., Wallraff, A., and Blais, A. Input-output theory for waveguide qed with an ensemble of inhomogeneous atoms. *Physical Review A 88*, 4 (2013), 043806.

[77] Lamb, W. E., and Retherford, R. C. Fine structure of the hydrogen atom by a microwave method. *Physical Review 72*, 3 (1947), 241–243.

[78] Lancaster, M. J. *Passive microwave device applications of high-temperature superconductors.* Cambridge University Press, 2006.

[79] Lanting, T., Cho, H.-M., Clarke, J., Holzapfel, W., Lee, A. T., Lueker, M., Richards, P., Dobbs, M. A., Spieler, H., and Smith, A. Frequency-domain multiplexed readout of transition-edge sensor arrays with a superconducting quantum interference device. *Applied Physics Letters 86*, 11 (2005), 112511.

[80] Lemons, D. S., and Langevin, P. *An introduction to stochastic processes in physics.* JHU Press, 2002.

[81] Lupascu, A., Saito, S., Picot, T., De Groot, P. C., Harmans, C. J. P. M., and Mooij, J. E. Quantum non-demolition measurement of a superconducting two-level system. *Nature Physics 3* (2007), 119.

[82] Marrocco, M., Weidinger, M., Sang, R., and Walther, H. Quantum electrodynamic shifts of rydberg energy levels between parallel metal plates. *Physical review letters 81*, 26 (1998), 5784.

[83] McDermott, R., Lee, S., Ten Haken, B., Trabesinger, A. H., Pines, A., and Clarke, J. Microtesla mri with a superconducting quantum interference device. *Proceedings of the National Academy of Sciences of the United States of America 101*, 21 (2004), 7857–7861.

[84] Milburn, G. J., and Walls, D. F. Quantum nondemolition measurements via quadratic coupling. *Phys. Rev. A 28*, 4 (1983), 2065–2070.

[85] Milonni, P. W., and Shih, M.-L. Casimir forces. *Contemporary Physics 33*, 5 (1992), 313–322.

[86] Moore, G. T. Quantum theory of the electromagnetic field in a variable-length one-dimensional cavity. *Journal of Mathematical Physics 11*, 9 (1970), 2679–2691.

[87] Mück, M., Kycia, J., and Clarke, J. Superconducting quantum interference device as a near-quantum-limited amplifier at 0.5 ghz. *Applied Physics Letters 78*, 7 (2001), 967–969.

[88] Mück, M., and McDermott, R. Radio-frequency amplifiers based on dc squids. *Supercon. Sci. Technol. 23*, 9 (2010), 093001.

[89] Muck, M., Welzel, C., and Clarke, J. Superconducting quantum interference device amplifiers at gigahertz frequencies. *Appl. Phys. Lett. 82*, 19 (2003), 3266–3268.

[90] Mulliken, R. S. The band spectrum of boron monoxide. *Nature 114*, 2862 (1924), 349–350.

[91] Nakamura, Y., Pashkin, Y., and Tsai, J. Coherent control of macroscopic quantum states in a single-Cooper-pair box. *Nature 398* (1999), 786.

[92] Nataf, P., and Ciuti, C. Is there a no-go theorem for superradiant quantum phase transitions in cavity and circuit qed? *arXiv preprint arXiv:1006.1801* (2010).

[93] Nataf, P., and Ciuti, C. Vacuum degeneracy of a circuit qed system in the ultrastrong coupling regime. *Physical review letters 104*, 2 (2010), 023601.

[94] Nation, P., Johansson, J., Blencowe, M., and Nori, F. Colloquium: Stimulating uncertainty: Amplifying the quantum vacuum with superconducting circuits. *Reviews of Modern Physics 84*, 1 (2012), 1.

[95] Nernst, W. *Verh. Deutsch. Phys. Ges. 18* (1916), 83.

[96] Nielsen, M. A., and Chuang, I. L. *Quantum Computation and Quantum Information.* Cambridge University Press, Cambridge, UK, 2000.

[97] Niskanen, A., Harrabi, K., Yoshihara, F., Nakamura, Y., Lloyd, S., and Tsai, J. Quantum coherent tunable coupling of superconducting qubits. *Science 316* (2007), 5825.

[98] Nyquist, H. Thermal agitation of electric charge in conductors. *Physical review 32*, 1 (1928), 110–113.

[99] Onnes, H. K. The superconductivity of mercury. *Leiden Comm. 122b* (1911), 124.

[100] Orlando, T., Mooij, J., Tian, L., van der Wal, C. H., Levitov, L., Lloyd, S., and Mazo, J. Superconducting persistent-current qubit. *Physical Review B 60*, 22 (1999), 15398.

[101] Osbourne, K., and Martinis, J. Superconducting qubits and the physics of josephson junctions. In *Les Houches conference proceedings* (2003).

[102] Paauw, F., Fedorov, A., Harmans, C., and Mooij, J. Tuning the gap of a superconducting flux qubit. *Phys. Rev. Lett. 102*, 9 (2009), 90501.

[103] Peropadre, B., Lindkvist, J., Hoi, I.-C., Wilson, C., Garcia-Ripoll, J. J., Delsing, P., and Johansson, G. Scattering of coherent states on a single artificial atom. *New Journal of Physics 15*, 3 (2013), 035009.

[104] Plourde, B., Zhang, J., Whaley, K., Wilhelm, F., Robertson, T., Hime, T., Linzen, S., Reichardt, P., Wu, C., and Clarke, J. Entangling flux qubits with a bipolar dynamic inductance. *Phys. Rev. B 70*, 14 (2004), 140501.

[105] Pozar, D. *Microwave Engineering*, 3 ed. WWiley, New York, 2005.

[106] Redfield, A. On the theory of relaxation processes. *IBM J Res. Develop. 1* (1957), 19.

[107] Reynaud, S., and Lambrecht, A. Casimir forces. *arXiv preprint arXiv:1410.2746* (2014).

[108] Ribeill, G. J., Hover, D., Chen, Y.-F., Zhu, S., and McDermott, R. Superconducting low-inductance undulatory galvanometer microwave amplifier: Theory. *Journal of Applied Physics 110* (2011), 103901.

[109] Schrödinger, E. An undulatory theory of the mechanics of atoms and molecules. *Physical Review 28*, 6 (1926), 1049.

[110] Serban, I., Plourde, B., and Wilhelm, F. Quantum nondemolition-like fast measurement scheme for a superconducting qubit. *Phys. Rev. B 78*, 5 (2008), 054507.

[111] Serban, I., Plourde, B. L. T., and Wilhelm, F. K. Quantum nondemolition-like fast measurement scheme for a superconducting qubit. *Phys. Rev. B 78* (2008), 054507.

[112] Sete, E. A., Gambetta, J. M., and Korotkov, A. N. Purcell effect with microwave drive: Suppression of qubit relaxation rate. *Physical Review B 89*, 10 (2014), 104516.

[113] Shor, P. Algorithms for quantum computation: Discrete logarithms and factoring. *Proceedings 35th Annual Symposium on Foundations of Computer Science* (1994), 124.

[114] Siddiqi, I., Vijay, R., Pierre, F., Wilson, C. M., Frunzio, L., Metcalfe, M., Rigetti, C., Schoelkopf, R. J., Devoret, M. H., Vion, D., and Esteve, D. Direct Observation of Dynamical Bifurcation between Two Driven Oscillation States of a Josephson Junction. *Phys. Rev. Lett. 94* (2005), 027005.

[115] Somaroo, S., Tseng, C. H., Havel, T. F., Laflamme, R., and Cory, D. G. Quantum simulations on a quantum computer. *Phys. Rev. Lett. 82*, 26 (Jun 1999), 5381–5384.

[116] Tian, L., Lloyd, S., and Orlando, T. Decoherence and relaxation of a superconducting quantum bit during measurement. *Phys. Rev. B 65* (2002), 144516.

[117] Tinkham, M. *Introduction to Superconductivity.* McGraw-Hill, New York, 1996.

[118] van der Wal, C. *Quantum Superpositions of Persistent Josephson Currents.* PhD thesis, Technische Universiteit Delft, 2001.

[119] van der Wal, C., Wilhelm, F., Harmans, C., and Mooij, J. Engieering decoherence in Josephson persistent-current qubits. *Eur. Phys. J. B 31* (2003), 111.

[120] van der Wal, C. H., Wilhelm, F., Harmans, C., and Mooij, J. Engineering decoherence in josephson persistent-current qubits. *The European Physical Journal B-Condensed Matter and Complex Systems 31*, 1 (2003), 111–124.

[121] van Kampen, N. *Stochastic processes in physics and chemistry.* Elsevier, Amsterdam, 1997.

[122] Vijay, R., Devoret, M. H., and Siddiqi, I. Invited Review Article: The Josephson bifurcation amplifier. *Rev. Sci. Instrum. 80* (2009), 111101.

[123] Vion, D., Aassime, A., Cottet, A., Joyez, P., Pothier, H., Urbina, C., Esteve, D., and Devoret, M. H. Manipulating the Quantum State of an Electrical Circuit. *Science 296* (2002), 886.

[124] Wallquist, M., Shumeiko, V., and Wendin, G. Selective coupling of superconducting charge qubits mediated by a tunable stripline cavity. *Physical Review B 74*, 22 (2006), 224506.

[125] Wendin, G., and Shumeiko, V. *Handbook of Theoretical and Computational Nanotechnology.* American Scientific Publishers, 2006, ch. Superconducting Quantum Circuits, Qubits and Computing.

[126] Wikipedia. Large hadron collider — wikipedia, the free encyclopedia, 2015. [Online; accessed 23-April-2015].

[127] Wikipedia. Maglev — wikipedia, the free encyclopedia, 2015. [Online; accessed 23-April-2015].

[128] Wilson, C., Johansson, G., Pourkabirian, A., Simoen, M., Johansson, J., Duty, T., Nori, F., and Delsing, P. Observation of the dynamical casimir effect in a superconducting circuit. *Nature 479*, 7373 (2011), 376–379.

[129] Wiseman, H., Milburn, G., and Corporation, E. *Quantum Measurement and Control.* Cambridge University Press, 2009.

[130] Yurke, B. Quantizing the damped harmonic oscillator. *American Journal of Physics 54*, 12 (1986), 1133–1139.

[131] Yurke, B., Corruccini, L., Kaminsky, P., Rupp, L., Smith, A., Silver, A., Simon, R., and Whittacker, E. Observation of parametric amplification and deamplification in a josephson parametric amplifier. *Phys. Rev. A 39* (1989), 2519.

[132] Yurke, B., and Denker, J. Quantum network theory. *Phys. Rev. A 29*, 3 (1984), 1419–1437.